

CHARACTERIZATION OF GEOHAZARDS VIA SEISMIC AND ACOUSTIC WAVES

By

Liam Toney

A Dissertation Submitted in Partial Fulfillment of the Requirements

for the Degree of

Doctor of Philosophy

in

Geophysics

University of Alaska Fairbanks

August 2023

APPROVED:

David Fee, Committee Chair

Carl Tape, Committee Member

Matthew Haney, Committee Member

Ronni Grapenthin, Committee Member

Paul McCarthy, Chair

Department of Geosciences

Karsten Hueffer, Dean

College of Natural Science & Mathematics

Richard Collins, Director

Graduate School

Abstract

Earth processes, such as large landslides and volcanic eruptions, occur globally and can be hazardous to life and property. Geophysics — the quantitative study of Earth processes and properties — is used to monitor and rapidly respond to these geohazards. In particular, seismoacoustics, which is the joint study of seismic waves in the solid Earth and acoustic waves in Earth’s atmosphere, has been proven effective for a variety of geophysical monitoring tasks. Typically, the acoustic waves studied are infrasonic: They have frequencies less than 20 hertz, which is below the threshold of human hearing. In this dissertation, we use seismic and acoustic waves and techniques to characterize geohazards, and we examine the propagation of the waves themselves to better understand how seismoacoustic energy is transformed on its path from a given source to the measurement location. Chapter 1 provides a broad overview of seismoacoustics tailored to this dissertation. In Chapter 2, we use seismic and acoustic waves to reconstruct the dynamics of two very large, and highly similar, ice and rock avalanches occurring in 2016 and 2019 on Iliamna Volcano (Alaska). We determine their trajectories using seismic data from distant stations, demonstrating the feasibility of remote seismic landslide characterization. Chapter 3 details the application of machine learning to a rich volcano infrasound dataset consisting of thousands of explosions recorded at Yasur Volcano (Vanuatu) over six days in 2016. We automatically generate a labeled catalog of infrasound waveforms associated to two different locations in Yasur’s summit crater, and use this catalog to test different strategies for transforming the waveforms prior to classification model input. In Chapter 4, we use the coupling of atmospheric waves into the Earth to leverage a dense network of about 900 seismometers around Mount Saint Helens volcano (Washington state) as a quasi-infrasound network. We use buried explosions from a 2014 experiment as sources of infrasound. The dense spatial wavefield measurements permit detailed examination of the effects of wind and topography on infrasound propagation. Finally, in Chapter 5 we conclude with some discussion of future work and additional seismoacoustic topics.

Table of Contents

	Page
Abstract.....	iii
Table of Contents	v
List of Figures.....	ix
List of Tables.....	xi
Acknowledgments	xiii
Chapter 1: General Introduction	1
1.1 Seismoacoustics.....	1
1.1.1 Propagation and Coupling.....	2
1.1.2 Deployment Styles	7
1.1.3 Approaches to Source Characterization.....	8
1.2 Earth Processes and their Seismoacoustic Signatures.....	12
1.2.1 Mass Movements	12
1.2.2 Volcanoes.....	13
1.2.3 Buried Anthropogenic Explosions	14
1.3 Machine Learning in Seismoacoustics	15
1.4 Overview of Manuscript Chapters.....	16
1.4.1 Chapter 2: Reconstructing the Dynamics of the Highly Similar May 2016 and June 2019 Iliamna Volcano (Alaska) Ice–Rock Avalanches from Seismoacoustic Data	16
1.4.2 Chapter 3: Waveform Features Strongly Control Subcrater Classification Performance for a Large, Labeled Volcano Infrasound Dataset	17
1.4.3 Chapter 4: Examining Infrasound Propagation at High Spatial Resolution Using a Nodal Seismic Array.....	17
1.5 Additional Output and Activities	18
1.6 References	18
Chapter 2: Reconstructing the Dynamics of the Highly Similar May 2016 and June 2019 Iliamna Volcano (Alaska) Ice–Rock Avalanches from Seismoacoustic Data	27
2.1 Abstract	27
2.2 Introduction	28
2.3 Background	30
2.3.1 Analysis of Long-Period Seismic Waves from Mass Movements.....	30
2.3.2 Acoustic Studies of Mass Movements	32
2.3.3 Ice–Rock Avalanches	33
2.3.4 Iliamna Volcano, Alaska	34
2.4 Data.....	36

2.4.1	Seismic Signals	37
2.4.2	Acoustic Signals.....	38
2.4.3	Aerial Photos, Satellite Imagery, and Elevation Data	39
2.5	Methods	41
2.5.1	Mass Estimation.....	41
2.5.2	Infrasound Analyses	42
2.5.3	Force Inversions	44
2.5.4	Trajectory Calculations	46
2.6	Results	48
2.6.1	Infrasound	48
2.6.2	Seismic Inversion and Derivative Results	49
2.7	Discussion	54
2.7.1	Acoustic Source Directionality	54
2.7.2	Multi-Stage Failure and Flow	55
2.7.3	Mass Estimation.....	56
2.7.4	Flow Dynamics.....	57
2.7.5	Inversion Stability and Trajectory Uncertainties.....	59
2.7.6	Comparing Events	60
2.7.7	Feasibility for Rapid Hazard Response.....	61
2.8	Conclusions	62
2.9	Code and Data Availability	63
2.10	Appendix A: Inversion Formulation and Constraints.....	64
2.11	Acknowledgements	66
2.12	References	66

Chapter 3: Waveform Features Strongly Control Subcrater Classification Performance for a Large, Labeled Volcano Infrasound Dataset.....	75
3.1 Abstract	75
3.2 Introduction	75
3.3 Data	77
3.4 Methods	78
3.4.1 Creation of Labeled Dataset.....	78
3.4.2 Feature Extraction.....	80
3.4.3 Support Vector Classification	82
3.5 Results	82
3.5.1 Trends in Labeled Catalog	82
3.5.2 Classification Accuracy.....	83
3.6 Discussion	85
3.7 Conclusions	88
3.8 Data and Resources	89
3.9 Acknowledgments.....	89
3.10 References	90

Chapter 4: Examining Infrasound Propagation at High Spatial Resolution Using a Nodal Seismic Array	95
4.1 Abstract	95
4.2 Introduction	96
4.3 Data & Methods	98
4.3.1 Seismic data processing	98
4.3.2 Topographic ray path analysis.....	100
4.3.3 Atmospheric data and models	101
4.3.4 Numerical modeling of the infrasound wavefield	103
4.4 Results	104
4.4.1 Presence of acoustic–seismic coupled arrivals on nodes.....	104
4.4.2 Atmospheric state during the shots.....	105
4.4.3 Spatial variability of acoustic–seismic coupled arrival amplitudes.....	107
4.4.4 Travel time variations and azimuth dependence.....	109
4.4.5 Infrasound wavefield simulations	111
4.5 Discussion	113
4.5.1 Factors controlling the presence of coupled signals on nodes	113
4.5.2 Spatial coherence of STA/LTA amplitude and path length differences...	116
4.5.3 Factors influencing infrasound travel times	117
4.5.4 Propagation at intermediate source–receiver distances	119
4.5.5 Applications.....	121
4.6 Conclusions	123
4.7 Data Availability Statement	124
4.8 Acknowledgments.....	124
4.9 References	125
4.10 Supplemental Material	133
Chapter 5: General Conclusions	135
5.1 Additional Work	137
5.1.1 Summer 2023 return to Yasur Volcano.....	137
5.1.2 Atmospheric acoustic waves in Alaska from the Hunga volcano eruption	138
5.2 References	139

List of Figures

	Page
Figure 1.1 Visualization of infrasound propagation in a realistic atmosphere	4
Figure 1.2 Simulation of infrasound propagation over topography	5
Figure 1.3 Schematic of three different types of seismic–acoustic coupling	7
Figure 1.4 Schematic of network versus array deployment	8
Figure 1.5 Schematic of reverse time migration source location method	10
Figure 1.6 Seismoacoustic waveforms from different types of mass movements.....	13
Figure 1.7 Infrasound waveforms from several different volcanic explosions.....	14
Figure 2.1 Station map of Cook Inlet, Alaska region.....	30
Figure 2.2 Satellite images of the 2016 and 2019 Red Glacier avalanche deposits....	31
Figure 2.3 Photographs of the 2016 and 2019 Red Glacier avalanche deposits	37
Figure 2.4 Seismic waveforms and spectrograms from the 2016 and 2019 events.....	39
Figure 2.5 Seismic spectra at station HOM from the 2016 and 2019 events	40
Figure 2.6 Modeled infrasound transmission loss for the 2016 and 2019 events	41
Figure 2.7 Infrasound signals from the 2016 and 2019 events.....	42
Figure 2.8 Force inversion results for the 2016 and 2019 events	50
Figure 2.9 Waveform fits for the 2016 and 2019 events	51
Figure 2.10 Inversion-derived trajectories for the 2016 and 2019 events	53
Figure 3.1 Map of study region and located events	77
Figure 3.2 Temporal evolution of labeled dataset.....	80
Figure 3.3 Classification accuracy scores for “generalization case”	83
Figure 3.4 Classification accuracy scores for “same-station case”	84
Figure 4.1 Station map and iMUSH explosion timeline.....	99
Figure 4.2 Short-term average to long-term average ratio shot gathers.....	102
Figure 4.3 Scatter plot of shot–node distances versus pre-shot noise	105

Figure 4.4	Wind speed and direction during shots X5 and Y5.....	108
Figure 4.5	Comparison between coupled observations and path length differences ..	110
Figure 4.6	Comparison between measured celerities and winds for shot Y5.....	111
Figure 4.7	Finite-difference time-domain simulation for shot Y5	114
Figure 4.8	Finite-difference time-domain simulation for shot X5	115
Figure 4.9	Waveforms and spectrograms for coupled shot X4 arrivals on 12 nodes .	118
Figure 4.10	Regional infrasound station recordings of iMUSH shots.....	133
Figure 4.11	ERA5 atmospheric profiles used in the numerical modeling.....	134
Figure 5.1	Amplitudes of the Hunga eruption Lamb wave across Alaska.....	138

List of Tables

	Page
4.1 Summary of acoustic–seismic coupled arrival observations for each shot . . .	106

Acknowledgments

The graduate school journey has been a roller coaster. I give a heartfelt thanks to my advisor, David Fee, for knowing when to nudge me, and when to give me space. I was lucky to find that your seismoacoustic interests are as broad as mine — as reflected in this dissertation! It has been special to share moments of research discovery, or simply comedy, and I look forward to many more collaborations in the next chapter. To my committee: Carl Tape, Matthew Haney, and Ronni Grapenthin — thanks for rooting for me.

Several professors at Pomona College were formative in my early research and academic life. Dwight Whitaker facilitated my first research experience. Thomas Moore was patient and kind to me when I [temporarily] dropped out of his particle physics class in a fit of academic uncertainty! Likewise, when I swung in the geology direction and found myself struggling, Bob Gaines helped me succeed. Eric Grosfils was my mentor at Pomona for all things geophysics. Finally, the late Alfred Kwok — to whom my undergraduate thesis is dedicated — demonstrated that work isn't everything.

I was halfway through my undergraduate degree in physics when I met with Jackie Caplan-Auerbach to ask her about this thing called “geophysics.” That conversation opened my eyes to a research future that I could imagine myself in. Soon after, I found myself in my first geophysics research experience, where I learned much from my supervisors Rob Abbott and Hunter Knox, and mentor Rob Anthony. I'm grateful to Michael Hubenthal for organizing that Incorporated Research Institutions for Seismology internship experience — simply put, it's the reason I'm where I am today.

Between undergraduate and graduate school, Yannik Behr helped me make the most out of a spontaneous internship at GNS Science in New Zealand, and got me started in Python. That whole opportunity wouldn't have happened if Nico Fournier hadn't been willing to meet a random backpacker for coffee in Taupō — cheers for that! Kate Allstadt has been an

approachable and formative mentor these most recent few years of graduate school. I thank Suzan van der Lee for her kindness and wisdom.

I'd like to thank the staff of the Alaska Volcano Observatory, the Alaska Earthquake Center, and the Wilson Alaska Technical Center for their support and career, field, and scientific advice over my time at UAF. The people at these organizations are pros, and I had no idea how important these groups would be to my success and growth at UAF.

At UAF, I've been so lucky that my peers and lab-mates have also been my good friends. To "Team Infrasond" — Alex Iezzi, Julia Gestrich, Jordan Bishop, Darren Tan, Alex Witsil — thanks for your support, laughs, and honest feedback. Outside of the "lab," I've been fortunate to form some of the strongest friendships of my life in graduate school. I know I'll forget someone if I attempt to list people, so to these folks: You know who you are, and I'm so glad I met you. Thanks to my "family friends," in particular Liz Schermer, for their decade+ of support and advice. And Hannah: The magnitude of the love and support I feel from you is larger than you know. Finally, to mom, dad, and Katie — thanks for encouraging me. I love you all!

The three papers which form the body of this dissertation were written by me, and based upon research that I conducted. I received guidance and edits from the following co-authors: David Fee, Kate Allstadt, Matthew Haney, Robin Matoza, Alex Witsil, Brandon Schmandt, and Jordan Bishop. When "we" appears in this dissertation, it refers to me along with the above individuals.

Much of the work detailed in this dissertation was carried out on Troth Yeddha', on the lands of the Lower Tanana River Dene.

Chapter 1: General Introduction

Geohazards, such as earthquakes, landslides, and volcanic events, pose significant risks to life and property in the U.S. and worldwide. There is an obvious motivation to prevent human loss of life and other impacts from these hazards by reducing risk — for example, evacuating people from affected areas, re-directing air traffic, or re-routing roads. Additionally, after sudden activity — such as an eruption or sudden ground failure — occurs, rapid response efforts can reduce the negative fallout from these events.

Geophysical monitoring has long played a key role in reducing risk from geohazards. The breadth of geophysical monitoring applications is far too large to list in full here, but some examples include: measuring volcano inflation using ground-based GPS to infer magma recharge which might signal an impending eruption (e.g., Ji & Herring, 2011); using seismic stations to provide early warning for large earthquakes (Allen et al., 2009); and monitoring slope deformation using satellite-based radar to understand possible pre-failure signals (e.g., J. Kim et al., 2022).

This dissertation focuses on a subset of geophysical monitoring techniques: seismology and inaudible acoustics. This introductory chapter aims to provide a broad background on how seismic and acoustic waves are produced by sources of interest, how they propagate through the Earth and atmosphere, and how we can harness the information they contain about both their source and the medium through which they traveled.

1.1 Seismoacoustics

Broadly speaking, seismoacoustics is the field concerned with mechanical waves in the solid Earth — seismic waves — and in the atmosphere — acoustic waves — and how wave energy interacts across the Earth and atmospheric domains (Arrowsmith et al., 2010). While aerial sources directly generate only acoustic waves, and buried sources only seismic waves, energy propagates from these sources and is partially converted when it encounters the

Earth’s surface. Processes occurring directly on Earth’s surface, such as landslides, produce seismic and acoustic energy simultaneously, making them especially rich seismoacoustic sources. For such processes, joint analyses of the seismic and acoustic signals produced can be complementary, since the two wave types do not necessarily reflect the same source phenomena (Toney et al., 2021).

Seismic waves are elastic waves which propagate through, and on the surface of, the Earth (Stein & Wysession, 2003). These waves can cover frequency ranges of millihertz (e.g., Earth’s normal modes; Montagner & Roult, 2008) up to tens of hertz. The seismic waves most relevant to this dissertation are P (compressional) and S (shear) waves — which are collectively referred to as body waves — and surface waves, which are typically slower than body waves. Atmospheric acoustic waves are compressional waves which propagate in Earth’s atmosphere. Infrasound is a subset of atmospheric acoustics, typically defined to be waves with frequencies less than 20 Hz — approximately the threshold of human hearing. The lower frequency limit for infrasound is the Brunt–Väisälä frequency of a few millihertz. Near this frequency, the effect of gravity as a restoring force cannot be ignored, giving rise to so-called acoustic-gravity waves (Hines, 1960; Yeh & Liu, 1974).

1.1.1 Propagation and Coupling

Seismic and acoustic waves recorded at sensors reflect source processes but also the medium through which they travel (and the response of the recording instrument). Therefore, understanding seismoacoustic propagation is essential to accurately characterizing seismoacoustic sources.

Seismic wave propagation is controlled by Earth structure. Under simplifying approximations, seismic waves bend in the Earth due to refraction (Snell’s law). Since seismic wavespeeds generally increase with depth in the Earth, seismic waves tend to be refracted back towards Earth’s surface (Stein & Wysession, 2003). The wavelength of seismic waves determines the spatial scale of Earth structure and topography to which they are sensitive.

Long-period (> 10 s) seismic waves have longer wavelengths which are less sensitive to fine-scale Earth structure and terrain. This allows studies focusing solely on this frequency band to use simplified Earth models, such as 1D models without topography. Seismic wave propagation can be modeled in the infinite-frequency approximation (geometric rays), or with full-wave approaches which fully numerically solve the wave equation (Nissen-Meyer et al., 2014) or use in-between methods such as frequency-wavenumber integration and normal-mode summation. Full-wave numerical modeling is computationally expensive, and the creation of meshes which sufficiently capture subsurface medium properties can be challenging. However, simplified 1D Earth models permit the use of the aforementioned in-between semi-analytical methods which are more efficient (Yang et al., 2010). A whole field of seismology, not discussed in this dissertation, is dedicated to using known seismic sources to understand wave propagation and image the subsurface of the Earth.

Infrasound propagation is controlled mainly by atmospheric state and by wave interactions with topography. Generally, atmospheric effects are ignored at local (< 15 km from source; Fee & Matoza, 2013) distances, while at regional to global distances, typically only atmospheric state is considered and influences of topography are ignored.

The speed of sound in air, c , is controlled largely by temperature:

$$c = \sqrt{\frac{\gamma RT}{M}}, \quad (1.1)$$

where γ is the adiabatic index (about 1.4 for dry air), M is the molar mass (0.02896 kg/mol for dry air), T is air temperature in kelvin, and R is the molar gas constant (Pierce, 2019). The atmospheric influence on infrasound propagation is often approximated using the effective sound speed, c_{eff} , which is defined as

$$c_{\text{eff}} = c + \hat{\mathbf{p}} \cdot \mathbf{w}, \quad (1.2)$$

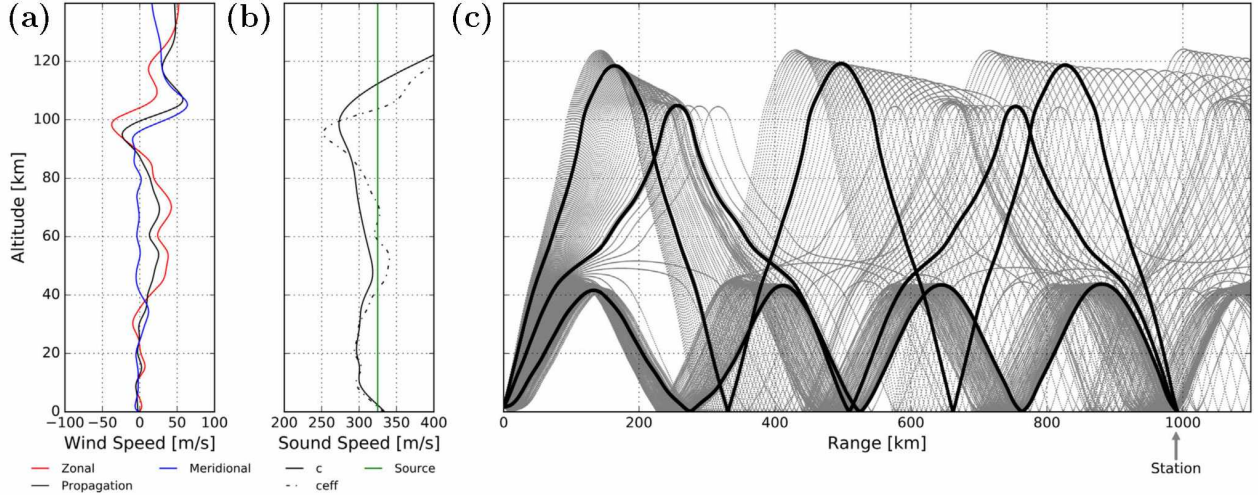


Figure 1.1 Example of infrasound propagation in a realistic atmosphere with ducts. **(a)** Winds as a function of height. “Zonal” and “meridional” refer to eastward and northward winds, respectively. The black line shows the quantity $\hat{\mathbf{p}} \cdot \mathbf{w}$ — the wind component in the propagation direction (see Equation 1.2). **(b)** Sound speeds as a function of height. **(c)** Predicted ray paths in this atmosphere. Adapted from Figure 4 in Iezzi, Schwaiger, et al. (2019).

where c is the static sound speed from Equation 1.1, $\hat{\mathbf{p}}$ is a unit vector pointing from the source to the receiver (i.e., the propagation direction) and \mathbf{w} is the wind vector (Godin, 2002). When source and receiver locations are known, we can combine Equations 1.1 and 1.2 to obtain the effective sound speed if we know the temperature and wind fields as a function of height.

When the effective sound at some elevation up in the atmosphere, $c_{\text{eff}}(z)$, is greater than the effective sound speed at the elevation of the source $c_{\text{eff}}(z_{\text{src}})$, then infrasound will refract back down towards the Earth’s surface. Conversely, if $c_{\text{eff}}(z)$ is everywhere lower in the atmosphere than at the surface, infrasound is expected to refract upwards. Vertical regions of the atmosphere where $c_{\text{eff}}(z) > c_{\text{eff}}(z_{\text{src}})$ are referred to as ducts or waveguides. Figure 1.1 shows a visualization of infrasound propagation through a realistic atmosphere. Areas where $c_{\text{eff}}(z)$ (dashed line) exceeds its value at the source (green line) form a duct which encourages efficient propagation of infrasound.

Infrasound waves interact with topography via reflection, scattering, focusing, and diffraction. Reflection is the “bouncing” of waves off of a surface, while scattering is a smaller scale

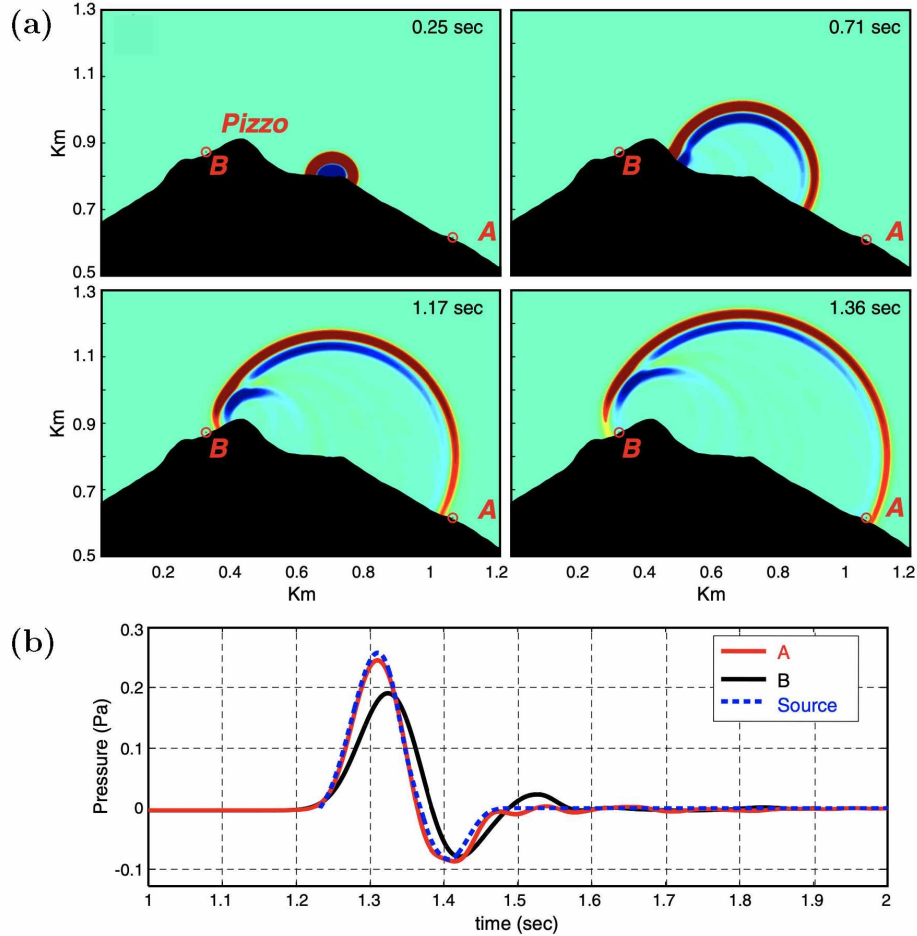


Figure 1.2 Simulation of infrasound propagation over topography at Stromboli volcano, Italy. **(a)** Snapshots of the acoustic wavefield at different times from a simulation. Red indicates compression and blue rarefaction. “A” and “B” labels denote two synthetic sensors. **(b)** Simulated pressure waveforms at the two sensors shown in **(a)**, compared to the source waveform (blue dashed line). Adapted from Figure 7 in Lacanna and Ripepe (2013).

process associated with rough surfaces that is not predicted by geometric acoustics (Blom, 2020). Focusing occurs at concave surfaces where energy is concentrated, analogous to a concave lens in optics. Diffraction is the “bending” of acoustic waves around obstructions, which can result in sound reaching the ground surface even when the source and receiver are not within line-of-sight from one another. Diffraction results in a loss of energy, as shown in Figure 1.2. It is also associated with an increase in travel time from source to receiver due to the longer path the wave must take over terrain (see, e.g., Fee et al., 2021).

Like in seismology, infrasound can be modeled in the geometric limit using ray tracing methods (see, e.g., Figure 1.1c), and full synthetic waveforms can be obtained via numerical simulations (e.g., Bishop et al., 2022). These approaches can incorporate wave interactions with terrain as well as range-dependent atmospheric state. While topography can be measured quite accurately, especially with the increasing popularity of uncrewed aircraft systems (UAS) for digital elevation model acquisition (Ruiz et al., 2013), the same is not true for atmospheric variables. Furthermore, the atmosphere can vary substantially in space and time. This poses challenges for accurately predicting infrasound propagation. As with seismology, infrasound propagation itself can be investigated using infrasound sources such as explosions or ocean-produced pressure variations (e.g., Haney, 2009).

Seismic–acoustic and acoustic–seismic coupling — that is, the conversion of seismic waves to acoustic waves, and vice versa — are important phenomena which have been increasingly studied in the seismoacoustics community (Bishop et al., 2022; Fee et al., 2023; Ichihara et al., 2012; Macpherson et al., 2023; Matoza & Fee, 2014; McKee et al., 2018; Wills et al., 2022). Seismic–acoustic coupling can take several forms (Figure 1.3). “Epicentral” infrasound refers to acoustic waves generated near the epicenter of a buried source, such as an earthquake or explosion. This type of infrasound travels the entirety of the path from source (epicenter) to receiver as an infrasound wave. “Secondary” infrasound is produced by topographic features, such as mountain ranges, being shaken by seismic surface waves. These arrivals will have faster apparent speeds, because they travel as faster seismic waves for a portion of the source–receiver path. Finally, in the immediate vicinity of the receiver, seismic shaking can produce “local” infrasound, which is coherent with the seismic ground motion.

Acoustic–seismic coupling has been observed for aerial sources such as spacecraft re-entries (Edwards et al., 2007) and bolides (Walker et al., 2010) as well as surface sources like volcanoes (Fee et al., 2021; Matoza & Fee, 2014). The coupling is typically frequency dependent (Matoza & Fee, 2014), and linked to near-surface material properties (Novoselov et al., 2020) as well as incidence angle (Bishop et al., 2022). More complete characterization

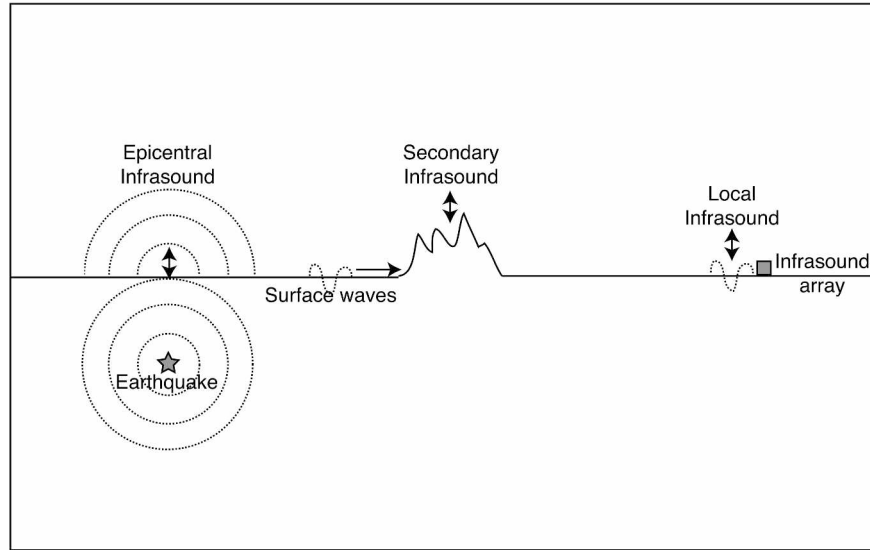


Figure 1.3 Schematic of three different types of seismic–acoustic coupling, showing “epicentral,” “secondary,” and “local” infrasound. Reproduced from Figure 2 in Arrowsmith et al. (2010).

of acoustic–seismic coupling is desirable as it opens the door for the utilization of seismic sensors as quasi-infrasound sensors.

1.1.2 Deployment Styles

Both seismic and infrasound sensors can be deployed in several distinct styles depending upon the desired application. Networks consist of a number of sensors spaced throughout the study area (e.g., around a volcanic edifice, or throughout the state of Alaska). Sources of interest should generally be located within the network. Arrays are strategically arranged collections of sensors designed to locate sources distal to the array by leveraging travel time differences between waves arriving on the array. Schematics of these two sensor arrangements are shown in Figure 1.4.

A typical “single station” seismic or infrasound installation consists of the sensor itself, a digitizer and data storage device, a telemetry link for transmitting data from the site, and a power system. In “campaign-style” temporary deployments, telemetry may be omitted and data recovered directly from the digitizer at the conclusion of the experiment. Often, a single

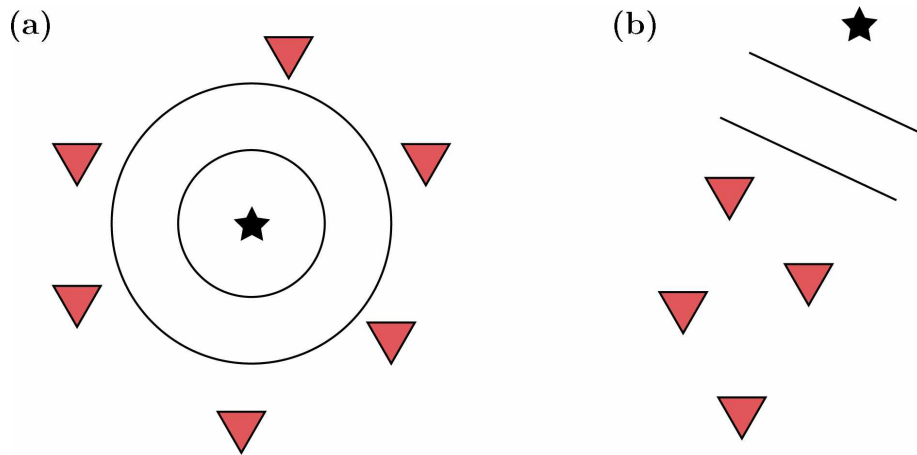


Figure 1.4 Schematic of network versus array deployment. **(a)** A network configuration, where the source (black star) is within the collection of sensors (red triangles). Wavefronts are shown as black lines. **(b)** Array configuration. The source is outside of the array, and wavefronts arrive at different sensors at different times. Note that the source–array distance is not to scale (typically, the desired source should be much farther from the array).

site has multiple instruments connected to a digitizer — for example, a seismometer and an infrasound sensor together. A more recent instrumentation design for seismometers places the power, digitizer, and sensor in one self-contained package. These instruments, referred to as “nodes,” are very quick to deploy in large quantities when dense spatial measurements of the wavefield are desired. To date, they have only been realized for seismic sensors, but recent infrasound instrumentation efforts have focused on developing an analog to seismic nodes for rapid large-N infrasound deployments (Anderson et al., 2018).

1.1.3 Approaches to Source Characterization

Seismoacoustic source characterization can broadly be divided into three steps which are, in most cases, sequentially performed and require progressively more robust data. These are detection, location, and quantification. Detection is the simplest source characterization product — a binary “yes/no” (or a probability) that an event occurred, with an estimated origin time. This may or may not involve a classification of source type. Generally, waveform data are transformed into a time series product that is triggered using some threshold. This

approach almost always relies on contributions from multiple stations which must “agree” that an event occurred. Seismoacoustic detection is a large topic which has obvious implications in the nuclear monitoring community (Le Pichon et al., 2009), but is not a large focus of the work in this dissertation.

Source location is the next layer of detail after detection. Very broadly, source location techniques can be divided into network- and array-based methods (see §1.1.2). Network-based methods typically involve grid searches over candidate locations within the network. Two common approaches are reverse time migration (RTM; e.g., Fee et al., 2021; Walker et al., 2010) and amplitude source location (e.g., Watson et al., 2023). In reverse time migration, also termed backprojection, travel times are computed for each candidate location in the grid to each receiver. The waveform at each receiver is then time-shifted using the computed travel time, and the waveforms are combined, or “stacked,” to produce a stack function ($Q(t)$; see Figure 1.5). The trial grid point and time with the highest stack value is chosen as the location and time of the source. RTM can be applied to seismic or acoustic data, however, location accuracy and precision are dependent on many factors. One principal concern is the fidelity of the travel time calculations, which can be complex, especially for high-frequency seismic waves and for infrasound propagation in severe topography (see §1.1.1). Amplitude source location for seismic waves follows a similar grid search pattern, however instead of computing travel times, predicted amplitudes at each station are calculated. The optimal source location is the one which produces the best-fitting amplitude attenuation relationship with distance for all stations (Battaglia & Aki, 2003).

Array-based methods exploit differential arrival times of seismic or acoustic waves on an intentionally-formed geometry of sensors (Figure 1.4b). Individual sensors in an array are typically referred to as “elements.” Assuming that an acoustic or seismic wave traveling across an array is planar — a valid assumption for distal sources (Szuberla et al., 2006) — then measured travel time differences across the array can be used to solve for the slowness vector, $\boldsymbol{\beta}$. The backazimuth from the source to the array is given by $\phi = \tan^{-1}(\beta_y/\beta_x)$, and

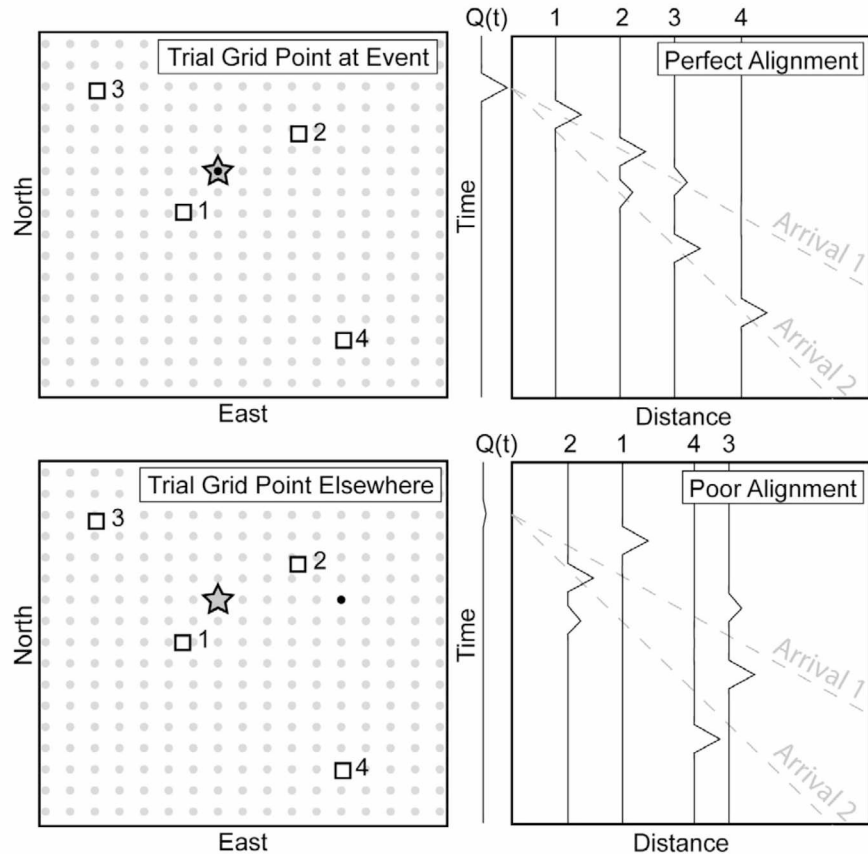


Figure 1.5 Schematic of the reverse time migration source location method. The left-hand boxes show the source search grid. Each gray dot is a candidate source location, and the black dot is the chosen source location. Receivers are shown as white squares, and the true source as a gray star. The right-hand boxes show the corresponding waveforms. Theoretically perfect alignment is achieved when the true source is chosen (top row). Reproduced from Figure 5 in Walker et al. (2010).

the trace velocity is $v = 1/\|\beta\|$ (Bishop et al., 2020). The trace velocity is the apparent speed of the wave traversing the array; it is related to the local sound speed c by

$$v = \frac{c}{\cos \theta}, \quad (1.3)$$

where θ is the incidence angle of the wave measured from the horizontal. For a horizontally propagating wave, $\theta = 0^\circ$ and Equation 1.3 gives $v = c$ — that is, the trace velocity is equal to the local sound speed. As θ approaches 90° , or vertical incidence, v approaches infinity. This is because a vertically incident plane wave arrives at each array element at the

same time. Note that if c is well-constrained, the incidence angle of a wave can be determined from v using Equation 1.3. A single array can only provide a direction of arrival, but multiple arrays can be used to locate sources via cross-beam analysis (e.g., Matoza et al., 2017).

A new class of location methods uses a single, co-located or nearly co-located seismoacoustic sensor pair to estimate signal backazimuths. These methods leverage acoustic–seismic coupled arrivals measured on the seismometer and uses the polarization (the particle motion of the seismic wave) to determine a direction of arrival. For an example implementation of this method, see McKee et al. (2018).

Once a seismoacoustic source is located, or if the location is already independently constrained, the next and most advanced step in the characterization process is the quantification of the source. Typically, this takes the form of some kind of inversion for source parameters. Geophysical inversion is a large topic which is far beyond the scope of this dissertation; Tarantola (2005) provides a thorough background on this topic. A geophysical inverse problem can be constructed as a “forward model,” where some data \mathbf{d} are produced by a model \mathbf{m} like:

$$\mathbf{d} = G(\mathbf{m}). \tag{1.4}$$

In Equation 1.4, \mathbf{d} is a vector of data. For example, \mathbf{d} can be a three-component seismogram flattened into a 1D array of ground velocity values. \mathbf{m} is a vector containing the source parameters for the model which produces the data \mathbf{d} . For the seismogram example, \mathbf{m} could be a 1D array of earthquake source parameters. $G(\mathbf{m})$ is the function mapping a given model to the data it produces — the Green’s function. For the example introduced previously, the function G encompasses the earthquake source physics as well as the propagation physics. For a linear inverse problem, $G(\mathbf{m}) = \mathbf{Gm}$ — that is, the Green’s function can be described as a matrix.

In seismology, source inversions are commonly performed to obtain earthquake source parameters (i.e., moment tensors; Engdahl & Kanamori, 1980; Sipkin, 1982) and for point force sources such as volcanic eruptions (Kanamori & Given, 1982) and landslides (e.g.,

K. E. Allstadt, 2013). Infrasound source inversions have focused on constraining the volume flux from explosive eruptions, with point source (monopole or multipole) models (e.g., Iezzi, Fee, et al., 2019; K. Kim et al., 2015).

1.2 Earth Processes and their Seismoacoustic Signatures

The variety of processes producing seismic and acoustic waves is far too broad to list in full here. The following sections outline the seismoacoustic characteristics of surficial mass movements, volcanic explosions, and buried anthropogenic explosions, as these are the processes which form the focus of this dissertation.

1.2.1 *Mass Movements*

Mass movements, such as debris flows, avalanches, lahars, and rock falls, generate seismic and acoustic waves across a broad range of frequencies. In the time domain, signals are typically characterized by an emergent onset (i.e., lacking distinct P or S phases) and a tapered “tail.” Some examples of seismic and acoustic waveforms from mass movements are shown in Figure 1.6. The frequency content of the signals is controlled by the size and composition of the flow, but is in general broadband (< 1 Hz to > 20 Hz) due to the multiple, multi-scale processes occurring during an event (K. E. Allstadt et al., 2018).

The largest mass movements generate strong long-period seismic waves which are caused by the total bulk loading and unloading of the landslide mass on Earth’s surface (Ekström & Stark, 2013). Seismoacoustic source modeling for mass movements is made difficult by (1) the extended spatial nature of the source and (2) the movement of the source. Source movement may contribute to seismoacoustic source directionality (e.g., Watson, Carpenter, et al., 2022) — that is, higher signal amplitudes for stations located in the vicinity of the flow direction.

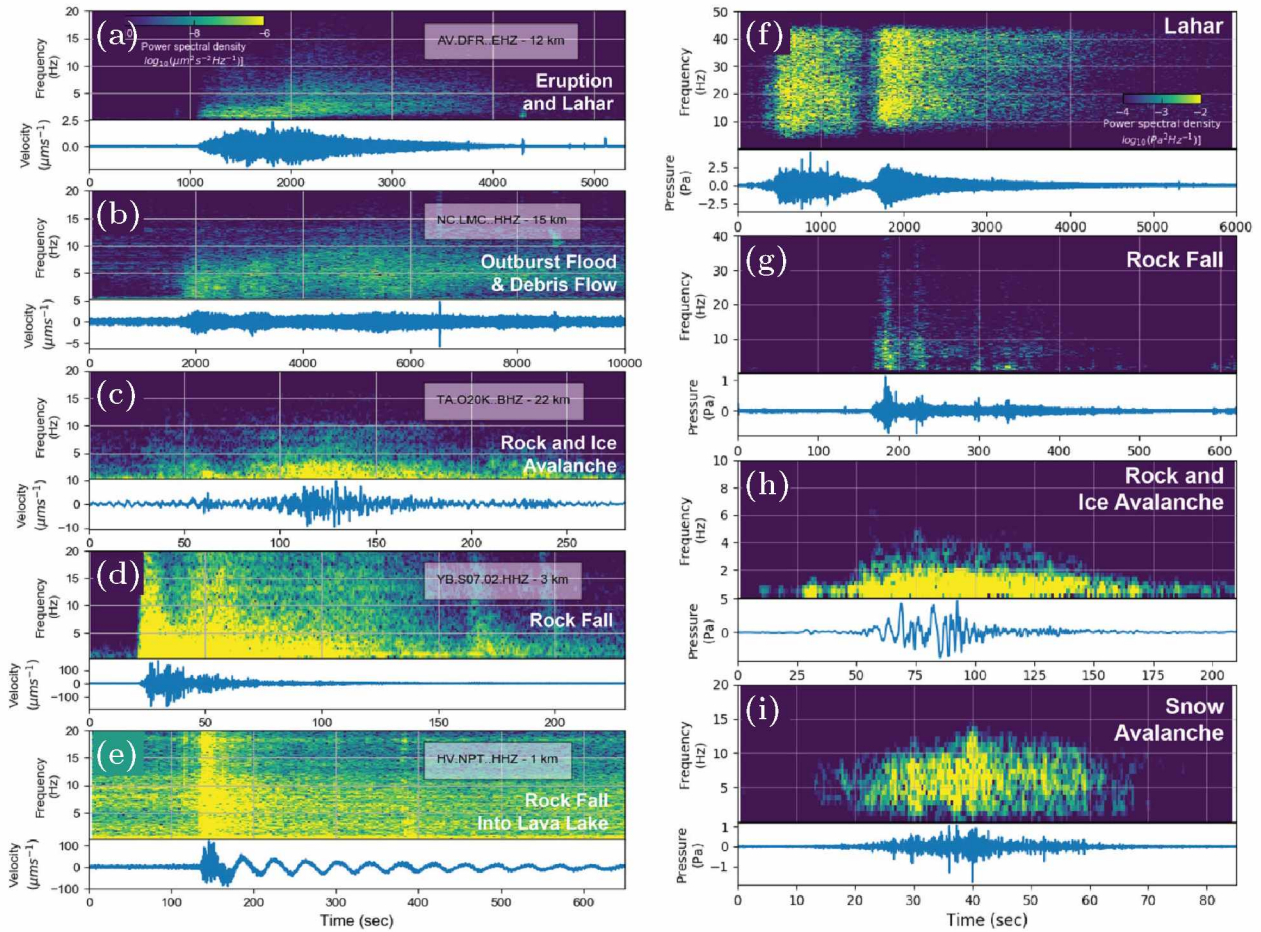


Figure 1.6 Seismic (a)–(e) (left-hand column) and acoustic (f)–(i) (right-hand column) waveforms produced by different types of mass movements, with spectrograms above each waveform showing the variable frequency content of each signal. Adapted from Figures 2 and 3 in K. E. Allstadt et al. (2018).

1.2.2 Volcanoes

Volcanoes are rich sources of seismoacoustic waves. Magma migration at volcanoes can give rise to volcano-tectonic earthquakes, where stresses created by migrating fluids fracture brittle rock; long-period (LP) events, associated with resonance in fluid-filled voids under the volcano; and volcanic tremor, a sustained signal with a source process thought to be similar to LP events (Chouet & Matoza, 2013). Infrasonic is associated with some of these seismic sources but is most prominently observed for explosive volcanic activity. The most commonly observed explosive infrasonic signals originate from strombolian and vulcanian eruptive

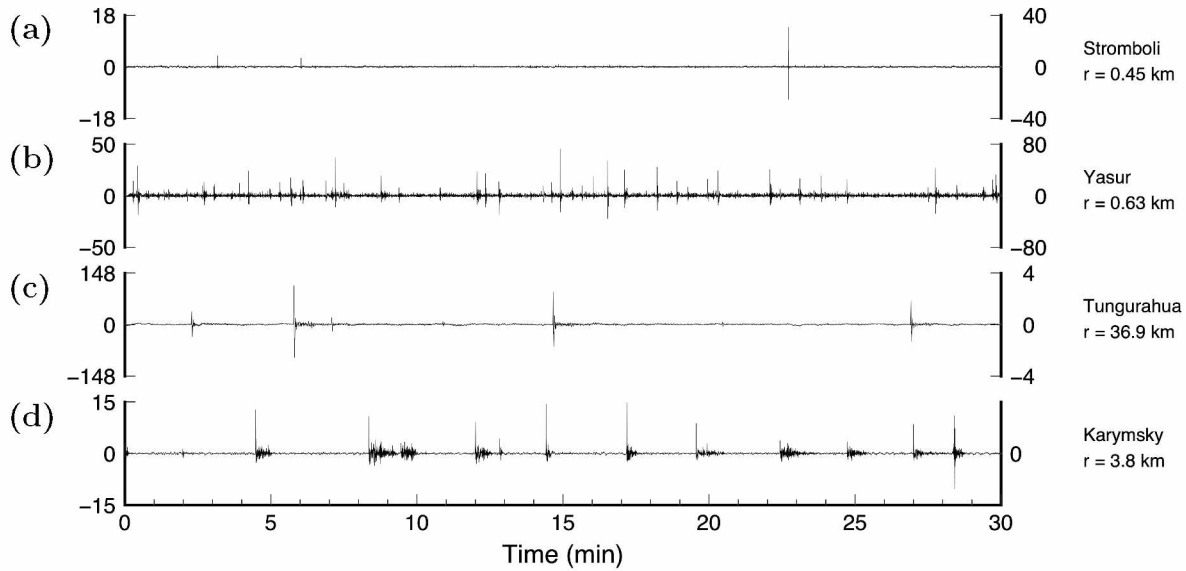


Figure 1.7 Infrasound waveforms from volcanic explosions. The left-hand y -axes show absolute pressure in Pa. The right-hand y -axes give the pressure corrected to a reference distance of 1 km. The volcano and the distance r from the sensor to the volcano are listed to the right of each waveform. (a)–(c) show strombolian explosions; (d) shows complex waveforms including explosions and subsequent jetting. Adapted from Figure 14 in Matoza and Roman (2022).

styles, where transient pressure waves are created by bursting gas bubbles which have risen through a magma-filled conduit, or by failure of a lava cap or dome after pressurization from magma intruding below (Fee et al., 2013). Some examples of these types of infrasound waveforms are shown in Figure 1.7. These types of events are commonly modeled as acoustic monopoles — that is, as simple sources radiating sound equally in all directions (Matoza et al., 2013).

1.2.3 Buried Anthropogenic Explosions

The generation of seismic and acoustic waves by buried and surface explosions is of key importance for verifying compliance with the Comprehensive Nuclear-Test-Ban Treaty (Bowers & Selby, 2009). A relevant task is discriminating between the seismoacoustic signatures of earthquakes versus explosions. Since buried explosions are, in an idealized case, isotropic sources of seismic radiation, in a homogeneous whole-space only P waves are expected to

be observed. However, in realistic environments, S waves and surface waves are observed due to wave interactions with the free surface and geologic structure (Massé, 1981; Stein & Wysession, 2003). Still, the relatively lower S wave and surface-wave energy produced by explosions versus earthquakes has long been used as a discriminant (Bowers & Selby, 2009). Buried explosions are known to generate epicentral infrasound via seismic–acoustic coupling (see §1.1.1) in addition to pure seismic waves (Che et al., 2014; Poppeliers et al., 2019). The relative partitioning of seismic and acoustic energy depends primarily upon geologic conditions and explosion burial depth (Ford et al., 2014).

1.3 Machine Learning in Seismoacoustics

The Earth sciences is a data-rich field, making it ripe for data-driven approaches such as machine learning (ML; Bergen et al., 2019), and ML is increasingly being applied to seismic and acoustic datasets. ML methods can be grouped broadly into supervised and unsupervised methods (Kong et al., 2019). Supervised methods involve the training of some model with labeled data, and subsequent application of the model to unseen data. A major application for supervised ML in seismology is earthquake phase picking (e.g., Mousavi et al., 2020), with the goal of detecting more and smaller earthquakes and reducing seismic analysis workload. Source classification has been performed using both seismic and acoustic data, such as for classifying rockfall events (Provost et al., 2017) or separating volcanic and earthquake activity (Albert & Linville, 2020). While large benchmark datasets do exist for some applications such as phase picking (Mousavi et al., 2019), a limitation of supervised methods is a dearth of training data for some event types. This is especially true for infrasound data (Toney et al., 2022). Unsupervised methods, which do not require training data, are therefore also relevant and can be used to cluster signals and discover trends in data (e.g., Watson, 2020; Witsil & Johnson, 2020). ML methods can additionally be divided into “shallow” and “deep” learning approaches. In shallow learning, statistical “features” (e.g., peak frequency) are extracted from data examples and input into a model. In deep learning, features are not explicitly

defined by the user but instead determined implicitly by a neural network. Deep learning is showing promise for a variety of waveform geophysics tasks (Mousavi & Beroza, 2022).

1.4 Overview of Manuscript Chapters

The body of this dissertation consists of three chapters corresponding to three projects undertaken during my PhD. Chapters 2 and 3 are published in open access peer-reviewed journals (Toney et al., 2021, 2022). Chapter 4 has been submitted to a peer-reviewed journal and is currently in review (as of 10 July 2023). Full citations for each published paper are provided as footnotes on the first page of the corresponding chapter.*

1.4.1 Chapter 2: Reconstructing the Dynamics of the Highly Similar May 2016 and June 2019 Iliamna Volcano (Alaska) Ice–Rock Avalanches from Seismoacoustic Data

Two massive ice and rock avalanches occurred on Iliamna Volcano (Alaska) in May 2016 and June 2019. Each avalanche transported material approximately 8 km downslope, and the deposits of the two avalanches were very similar in size and shape. We take advantage of a relatively dense state-wide network of seismometers and infrasound sensors to characterize these two events. Seismoacoustic signals from these events are generally quite similar, in line with the similarity in field observations, and the signals are energetic: infrasound signals from the events were recorded to distances exceeding 600 km. For each avalanche, we model the source as a time-varying point force and perform an inversion of long-period seismic signals to recover the best-fitting model. We further process the force-time function to obtain the trajectory of each avalanche. The avalanche speeds and flow paths we obtain are consistent with field observations and observed local infrasound signals. The repeatability of avalanches at Iliamna makes the volcano a prime candidate for focused studies on the seismoacoustic characteristics of large surficial mass wasting events.

*Small differences, such as those related to formatting, may exist between the published papers and the text in this dissertation. In such cases, the published paper should be taken as the version of record.

1.4.2 Chapter 3: Waveform Features Strongly Control Subcrater Classification Performance for a Large, Labeled Volcano Infrasonic Dataset

As mentioned in §1.3, the application of supervised ML to infrasonic data has been limited by a lack of training data. In this work, we use data from a six-day-long deployment at the highly active Yasur Volcano (Vanuatu) to train and test a simple classifier which determines the subcrater of origin for explosion waveforms. We use the five-station infrasonic network to locate more than 7,500 explosions and associate these with one of the two subcraters at Yasur. We extract features for the waveforms associated with each event, using both a manually-selected approach and an automated tool. When we train and test our algorithm on data from the same station, we achieve accuracies greater than 95%. When we generalize to training and testing on data from different stations, our accuracy is about 75%. We find that the automatically-chosen features do the best job of generalizing to unseen data. We demonstrate the the choice of summarizing features is the most important decision when tuning a shallow classifier for geophysical waveform data.

1.4.3 Chapter 4: Examining Infrasonic Propagation at High Spatial Resolution Using a Nodal Seismic Array

Source characterization is a key goal for infrasonic scientists and seismologists, but as §1.1.1 shows, accounting for propagation — which is essential for accurately locating and quantifying sources — is difficult. Here, we use acoustic–seismic coupled arrivals from buried explosions recorded on a dense network of nodal seismometers to assess fine-scale propagation effects related to atmospheric state and topography. The data come from the active-source portion of the Imaging Magma Under St. Helens (iMUSH) seismic imaging experiment, which took place in the summer of 2014 at Mount Saint Helens volcano in Washington state. The presence of coupled arrivals on the nodes for a given explosion is influenced by local wind noise as well as explosion–array distance. For explosions with extensive coupling on the nodes, we observe spatially variable amplitudes which can be explained by topographic obstructions

contributing to energy loss by diffraction. We also observe travel time variations consistent with winds from a high resolution (mesoscale) weather model. We perform full-wave numerical modeling of the infrasound wavefield from select explosions and find poor agreement with observed data which we largely attribute to complex and highly spatially variable acoustic–seismic coupling across the nodal array. The methods we apply to the iMUSH dataset can be applied to past and future dense seismic (and infrasound) deployments.

1.5 Additional Output and Activities

In addition to the publications associated with the chapters in this dissertation, I am the lead author on Toney and Allstadt (2021), and I am a co-author on Dannemann Dugick et al. (2021); Fee et al. (2021); Matoza et al. (2022); Watson, Iezzi, et al. (2022). I am also a developer on three published software projects (K. Allstadt & Toney, 2020; Toney, 2022; Uieda et al., 2022).

As a teaching assistant during the fall semester of 2020, I co-developed instructional materials for two UAF Department of Geosciences courses: GEOS F431/F631 Foundations of Geophysics (github.com/uafgeoteach/GEOS631_FoG), and GEOS F436/F636 Programming and Automation for Geoscientists (github.com/uafgeoteach/GEOS636_PAG).

I co-founded the UAF Geophysical Institute Diversity, Equity, and Inclusion Committee (gi.alaska.edu/diversity-equity-and-inclusion) with fellow student Jordan Bishop in 2020.

1.6 References

- Albert, S., & Linville, L. (2020). Benchmarking Current and Emerging Approaches to Infrasound Signal Classification. *Seismological Research Letters*, *91*(2A), 921–929. <https://doi.org/10.1785/0220190116>
- Allen, R. M., Gasparini, P., Kamigaichi, O., & Bose, M. (2009). The Status of Earthquake Early Warning around the World: An Introductory Overview. *Seismological Research Letters*, *80*(5), 682–693. <https://doi.org/10.1785/gssrl.80.5.682>

- Allstadt, K., & Toney, L. (2020). *lsforce*. U.S. Geological Survey. <https://doi.org/10.5066/P9CR20KW>
- Allstadt, K. E. (2013). Extracting source characteristics and dynamics of the August 2010 Mount Meager landslide from broadband seismograms. *Journal of Geophysical Research: Earth Surface*, *118*(3), 1472–1490. <https://doi.org/10.1002/jgrf.20110>
- Allstadt, K. E., Matoza, R. S., Lockhart, A. B., Moran, S. C., Caplan-Auerbach, J., Haney, M. M., Thelen, W. A., & Malone, S. D. (2018). Seismic and acoustic signatures of surficial mass movements at volcanoes. *Journal of Volcanology and Geothermal Research*, *364*, 76–106. <https://doi.org/10.1016/j.jvolgeores.2018.09.007>
- Anderson, J. F., Johnson, J. B., Bowman, D. C., & Ronan, T. J. (2018). The Gem Infrasound Logger and Custom-Built Instrumentation. *Seismological Research Letters*, *89*(1), 153–164. <https://doi.org/10.1785/0220170067>
- Arrowsmith, S. J., Johnson, J. B., Drob, D. P., & Hedlin, M. A. H. (2010). The seismoacoustic wavefield: A new paradigm in studying geophysical phenomena. *Reviews of Geophysics*, *48*(4), RG4003. <https://doi.org/10.1029/2010RG000335>
- Battaglia, J., & Aki, K. (2003). Location of seismic events and eruptive fissures on the Piton de la Fournaise volcano using seismic amplitudes. *Journal of Geophysical Research*, *108*(B8), 2364. <https://doi.org/10.1029/2002JB002193>
- Bergen, K. J., Johnson, P. A., de Hoop, M. V., & Beroza, G. C. (2019). Machine learning for data-driven discovery in solid Earth geoscience. *Science*, *363*(6433), eaau0323. <https://doi.org/10.1126/science.aau0323>
- Bishop, J. W., Fee, D., Modrak, R., Tape, C., & Kim, K. (2022). Spectral Element Modeling of Acoustic to Seismic Coupling Over Topography. *Journal of Geophysical Research: Solid Earth*, *127*(1). <https://doi.org/10.1029/2021JB023142>
- Bishop, J. W., Fee, D., & Szuberla, C. A. L. (2020). Improved infrasound array processing with robust estimators. *Geophysical Journal International*, *221*(3), 2058–2074. <https://doi.org/10.1093/gji/ggaa110>
- Blom, P. (2020). The influence of irregular terrain on infrasonic propagation in the troposphere. *The Journal of the Acoustical Society of America*, *148*(4), 1984–1997. <https://doi.org/10.1121/10.0002128>
- Bowers, D., & Selby, N. D. (2009). Forensic Seismology and the Comprehensive Nuclear-Test-Ban Treaty. *Annual Review of Earth and Planetary Sciences*, *37*(1), 209–236. <https://doi.org/10.1146/annurev.earth.36.031207.124143>

- Che, I.-Y., Park, J., Kim, I., Kim, T. S., & Lee, H.-I. (2014). Infrasound signals from the underground nuclear explosions of North Korea. *Geophysical Journal International*, *198*(1), 495–503. <https://doi.org/10.1093/gji/ggu150>
- Chouet, B. A., & Matoza, R. S. (2013). A multi-decadal view of seismic methods for detecting precursors of magma movement and eruption. *Journal of Volcanology and Geothermal Research*, *252*, 108–175. <https://doi.org/10.1016/j.jvolgeores.2012.11.013>
- Dannemann Dugick, F. K., van der Lee, S., Prieto, G. A., Dybing, S. N., Toney, L., & Cole, H. M. (2021). ROSES: Remote Online Sessions for Emerging Seismologists. *Seismological Research Letters*, *92*(4), 2657–2667. <https://doi.org/10.1785/0220200421>
- Edwards, W. N., Eaton, D. W., McCausland, P. J., ReVelle, D. O., & Brown, P. G. (2007). Calibrating infrasonic to seismic coupling using the Stardust sample return capsule shockwave: Implications for seismic observations of meteors. *Journal of Geophysical Research*, *112*(B10), B10306. <https://doi.org/10.1029/2006JB004621>
- Ekström, G., & Stark, C. P. (2013). Simple scaling of catastrophic landslide dynamics. *Science*, *339*(6126), 1416–1419. <https://doi.org/10.1126/science.1232887>
- Engdahl, E. R., & Kanamori, H. (1980). Determination of earthquake parameters. *Eos, Transactions American Geophysical Union*, *61*(6), 62. <https://doi.org/10.1029/EO061i006p00062>
- Fee, D., Macpherson, K., & Gabrielson, T. (2023). Characterizing Infrasound Station Frequency Response Using Large Earthquakes and Colocated Seismometers. *Bulletin of the Seismological Society of America*, 1–15. <https://doi.org/10.1785/0120220226>
- Fee, D., & Matoza, R. S. (2013). An overview of volcano infrasound: From hawaiian to plinian, local to global. *Journal of Volcanology and Geothermal Research*, *249*(3), 123–139. <https://doi.org/10.1016/j.jvolgeores.2012.09.002>
- Fee, D., Toney, L., Kim, K., Sanderson, R. W., Iezzi, A. M., Matoza, R. S., De Angelis, S., Jolly, A. D., Lyons, J. J., & Haney, M. M. (2021). Local Explosion Detection and Infrasound Localization by Reverse Time Migration Using 3-D Finite-Difference Wave Propagation. *Frontiers in Earth Science*, *9*, Article 620813. <https://doi.org/10.3389/feart.2021.620813>
- Fee, D., Waxler, R., Assink, J., Gitterman, Y., Given, J., Coyne, J., Mialle, P., Garces, M., Drob, D., Kleinert, D., Hofstetter, R., & Grenard, P. (2013). Overview of the 2009 and 2011 Sayarim infrasound calibration experiments. *Journal of Geophysical Research: Atmospheres*, *118*(12), 6122–6143. <https://doi.org/10.1002/jgrd.50398>

- Ford, S. R., Rodgers, A. J., Xu, H., Templeton, D. C., Harben, P., Foxall, W., & Reinke, R. E. (2014). Partitioning of Seismoacoustic Energy and Estimation of Yield and Height-of-Burst/Depth-of-Burial for Near-Surface Explosions. *Bulletin of the Seismological Society of America*, *104*(2), 608–623. <https://doi.org/10.1785/0120130130>
- Godin, O. A. (2002). An effective quiescent medium for sound propagating through an inhomogeneous, moving fluid. *The Journal of the Acoustical Society of America*, *112*(4), 1269–1275. <https://doi.org/10.1121/1.1504853>
- Haney, M. M. (2009). Infrasonic ambient noise interferometry from correlations of microbaroms. *Geophysical Research Letters*, *36*(19), L19808. <https://doi.org/10.1029/2009GL040179>
- Hines, C. O. (1960). Internal atmospheric gravity waves at ionospheric heights. *Canadian Journal of Physics*, *38*(11), 1441–1481. <https://doi.org/10.1139/p60-150>
- Ichihara, M., Takeo, M., Yokoo, A., Oikawa, J., & Ohminato, T. (2012). Monitoring volcanic activity using correlation patterns between infrasound and ground motion. *Geophysical Research Letters*, *39*(4), n/a-n/a. <https://doi.org/10.1029/2011GL050542>
- Iezzi, A. M., Fee, D., Kim, K., Jolly, A. D., & Matoza, R. S. (2019). Three-dimensional acoustic multipole waveform inversion at Yasur Volcano, Vanuatu. *Journal of Geophysical Research: Solid Earth*, *124*(8), 8679–8703. <https://doi.org/10.1029/2018JB017073>
- Iezzi, A. M., Schwaiger, H. F., Fee, D., & Haney, M. M. (2019). Application of an updated atmospheric model to explore volcano infrasound propagation and detection in Alaska. *Journal of Volcanology and Geothermal Research*, *371*, 192–205. <https://doi.org/10.1016/j.jvolgeores.2018.03.009>
- Ji, K. H., & Herring, T. A. (2011). Transient signal detection using GPS measurements: Transient inflation at Akutan volcano, Alaska, during early 2008. *Geophysical Research Letters*, *38*, Article L06307. <https://doi.org/10.1029/2011GL046904>
- Kanamori, H., & Given, J. W. (1982). Analysis of long-period seismic waves excited by the May 18, 1980, eruption of Mount St. Helens—A terrestrial monopole? *Journal of Geophysical Research: Solid Earth*, *87*(B7), 5422–5432. <https://doi.org/10.1029/JB087iB07p05422>
- Kim, J., Coe, J. A., Lu, Z., Avdievitch, N. N., & Hults, C. P. (2022). Spaceborne InSAR mapping of landslides and subsidence in rapidly deglaciating terrain, Glacier Bay National Park and Preserve and vicinity, Alaska and British Columbia. *Remote Sensing of Environment*, *281*(July), 113231. <https://doi.org/10.1016/j.rse.2022.113231>

- Kim, K., Fee, D., Yokoo, A., & Lees, J. M. (2015). Acoustic source inversion to estimate volume flux from volcanic explosions. *Geophysical Research Letters*, *42*(13), 5243–5249. <https://doi.org/10.1002/2015GL064466>
- Kong, Q., Trugman, D. T., Ross, Z. E., Bianco, M. J., Meade, B. J., & Gerstoft, P. (2019). Machine Learning in Seismology: Turning Data into Insights. *Seismological Research Letters*, *90*(1), 3–14. <https://doi.org/10.1785/0220180259>
- Lacanna, G., & Ripepe, M. (2013). Influence of near-source volcano topography on the acoustic wavefield and implication for source modeling. *Journal of Volcanology and Geothermal Research*, *250*, 9–18. <https://doi.org/10.1016/j.jvolgeores.2012.10.005>
- Le Pichon, A., Vergoz, J., Blanc, E., Guilbert, J., Ceranna, L., Evers, L., & Brachet, N. (2009). Assessing the performance of the International Monitoring System’s infrasound network: Geographical coverage and temporal variabilities. *Journal of Geophysical Research*, *114*(D8), D08112. <https://doi.org/10.1029/2008JD010907>
- Macpherson, K. A., Fee, D., Coffey, J. R., & Witsil, A. J. (2023). Using Local Infrasound to Estimate Seismic Velocity and Earthquake Magnitudes. *Bulletin of the Seismological Society of America*, 1–23. <https://doi.org/10.1785/0120220237>
- Massé, R. P. (1981). Review of seismic source models for underground nuclear explosions. *Bulletin of the Seismological Society of America*, *71*(4), 1249–1268. <https://doi.org/10.1785/BSSA0710041249>
- Matoza, R. S., & Fee, D. (2014). Infrasonic component of volcano-seismic eruption tremor. *Geophysical Research Letters*, *41*(6), 1964–1970. <https://doi.org/10.1002/2014GL059301>
- Matoza, R. S., Fee, D., Assink, J. D., Iezzi, A. M., Green, D. N., Kim, K., Toney, L., Lecocq, T., Krishnamoorthy, S., Lalande, J.-m., Nishida, K., Gee, K. L., Haney, M. M., Ortiz, H. D., Brissaud, Q., Martire, L., Rolland, L., Vergados, P., Nippres, A., ... Wilson, D. C. (2022). Atmospheric waves and global seismoacoustic observations of the January 2022 Hunga eruption, Tonga. *Science*, *377*(6601), 95–100. <https://doi.org/10.1126/science.abo7063>
- Matoza, R. S., Fee, D., Neilsen, T. B., Gee, K. L., & Ogden, D. E. (2013). Aeroacoustics of volcanic jets: Acoustic power estimation and jet velocity dependence. *Journal of Geophysical Research: Solid Earth*, *118*(12), 6269–6284. <https://doi.org/10.1002/2013JB010303>
- Matoza, R. S., Green, D. N., Le Pichon, A., Shearer, P. M., Fee, D., Mialle, P., & Ceranna, L. (2017). Automated detection and cataloging of global explosive volcanism using the International Monitoring System infrasound network. *Journal of Geophysical Research: Solid Earth*, *122*(4), 2946–2971. <https://doi.org/10.1002/2016JB013356>

- Matoza, R. S., & Roman, D. C. (2022). One hundred years of advances in volcano seismology and acoustics. *Bulletin of Volcanology*, *84*, Article 86. <https://doi.org/10.1007/s00445-022-01586-0>
- McKee, K., Fee, D., Haney, M., Matoza, R. S., & Lyons, J. (2018). Infrasound Signal Detection and Back Azimuth Estimation Using Ground-Coupled Airwaves on a Seismo-Acoustic Sensor Pair. *Journal of Geophysical Research: Solid Earth*, *123*(8), 6826–6844. <https://doi.org/10.1029/2017JB015132>
- Montagner, J.-P., & Roult, G. (2008). Normal modes of the Earth. *Journal of Physics: Conference Series*, *118*(1), 012004. <https://doi.org/10.1088/1742-6596/118/1/012004>
- Mousavi, S. M., & Beroza, G. C. (2022). Deep-learning seismology. *Science*, *377*(6607). <https://doi.org/10.1126/science.abm4470>
- Mousavi, S. M., Ellsworth, W. L., Zhu, W., Chuang, L. Y., & Beroza, G. C. (2020). Earthquake transformer—an attentive deep-learning model for simultaneous earthquake detection and phase picking. *Nature Communications*, *11*(1), 3952. <https://doi.org/10.1038/s41467-020-17591-w>
- Mousavi, S. M., Sheng, Y., Zhu, W., & Beroza, G. C. (2019). STanford EArthquake Dataset (STEAD): A Global Data Set of Seismic Signals for AI. *IEEE Access*, *7*, 179464–179476. <https://doi.org/10.1109/ACCESS.2019.2947848>
- Nissen-Meyer, T., van Driel, M., Stähler, S. C., Hosseini, K., Hempel, S., Auer, L., Colombi, A., & Fournier, A. (2014). AxiSEM: broadband 3-D seismic wavefields in axisymmetric media. *Solid Earth*, *5*(1), 425–445. <https://doi.org/10.5194/se-5-425-2014>
- Novoselov, A., Fuchs, F., & Bokelmann, G. (2020). Acoustic-to-seismic ground coupling: coupling efficiency and inferring near-surface properties. *Geophysical Journal International*, *223*(1), 144–160. <https://doi.org/10.1093/gji/ggaa304>
- Pierce, A. D. (2019). *Acoustics*. Cham: Springer International Publishing. <https://doi.org/10.1007/978-3-030-11214-1>
- Poppeliers, C., Anderson Aur, K., & Preston, L. (2019). The Relative Importance of Assumed Infrasound Source Terms and Effects of Atmospheric Models on the Linear Inversion of Infrasound Time Series at the Source Physics Experiment. *Bulletin of the Seismological Society of America*, *109*(1), 463–475. <https://doi.org/10.1785/0120180249>
- Provost, F., Hibert, C., & Malet, J.-P. (2017). Automatic classification of endogenous landslide seismicity using the Random Forest supervised classifier. *Geophysical Research Letters*, *44*(1), 113–120. <https://doi.org/10.1002/2016GL070709>

- Ruiz, J. J., Diaz-Mas, L., Perez, F., & Viguria, A. (2013). Evaluating the accuracy of DEM generation algorithms from UAV imagery. *The International Archives of the Photogrammetry, Remote Sensing and Spatial Information Sciences*, *XL-1/W2*(September), 333–337. <https://doi.org/10.5194/isprsarchives-XL-1-W2-333-2013>
- Sipkin, S. A. (1982). Estimation of earthquake source parameters by the inversion of waveform data: synthetic waveforms. *Physics of the Earth and Planetary Interiors*, *30*(2-3), 242–259. [https://doi.org/10.1016/0031-9201\(82\)90111-X](https://doi.org/10.1016/0031-9201(82)90111-X)
- Stein, S., & Wysession, M. (2003). *An Introduction to Seismology, Earthquakes, and Earth Structure*. Blackwell.
- Szuberla, C. A. L., Arnoult, K. M., Olson, J. V., & Wilson, D. K. (2006). Discrimination of near-field infrasound sources based on time-difference of arrival information. *The Journal of the Acoustical Society of America*, *120*(3), EL23-EL28. <https://doi.org/10.1121/1.2234517>
- Tarantola, A. (2005). *Inverse Problem Theory and Methods for Model Parameter Estimation*. Society for Industrial and Applied Mathematics. <https://doi.org/10.1137/1.9780898717921>
- Toney, L. (2022). *infresnel*. Zenodo. <https://doi.org/10.5281/zenodo.7388646>
- Toney, L., & Allstadt, K. E. (2021). lsforce: A Python-Based Single-Force Seismic Inversion Framework for Massive Landslides. *Seismological Research Letters*, *92*(4), 2610–2626. <https://doi.org/10.1785/0220210004>
- Toney, L., Fee, D., Allstadt, K. E., Haney, M. M., & Matoza, R. S. (2021). Reconstructing the dynamics of the highly similar May 2016 and June 2019 Iliamna Volcano (Alaska) ice–rock avalanches from seismoacoustic data. *Earth Surface Dynamics*, *9*(2), 271–293. <https://doi.org/10.5194/esurf-9-271-2021>
- Toney, L., Fee, D., Witsil, A., & Matoza, R. S. (2022). Waveform features strongly control subcrater classification performance for a large, labeled volcano infrasound dataset. *The Seismic Record*, *2*(3), 167–175. <https://doi.org/10.1785/0320220019>
- Uieda, L., Tian, D., Leong, W. J., Jones, M., Schlitzer, W., Grund, M., Toney, L., Yao, J., Magen, Y., Materna, K., Frölich, Y., Belem, A., Newton, T., Anant, A., Ziebarth, M., Quinn, J., & Wessel, P. (2022). *PyGMT: A Python interface for the Generic Mapping Tools*. Zenodo. <https://doi.org/10.5281/zenodo.6702566>

- Walker, K. T., Hedlin, M. A. H., de Groot-Hedlin, C., Vergoz, J., Le Pichon, A., & Drob, D. P. (2010). Source location of the 19 February 2008 Oregon bolide using seismic networks and infrasound arrays. *Journal of Geophysical Research*, *115*(B12), B12329. <https://doi.org/10.1029/2010JB007863>
- Watson, L. M. (2020). Using unsupervised machine learning to identify changes in eruptive behavior at Mount Etna, Italy. *Journal of Volcanology and Geothermal Research*, *405*, 107042. <https://doi.org/10.1016/j.jvolgeores.2020.107042>
- Watson, L. M., Cannata, A., & Andronico, D. (2023). Tracking a pyroclastic density current with seismic signals at Mt. Etna (Italy). *Journal of Geophysical Research: Solid Earth*, *128*, Article e2022JB026114. <https://doi.org/10.1029/2022JB026114>
- Watson, L. M., Carpenter, B., Thompson, K., & Johnson, J. B. (2022). Using local infrasound arrays to detect plunging snow avalanches along the Milford Road, New Zealand (Aotearoa). *Natural Hazards*, *111*(1), 949–972. <https://doi.org/10.1007/s11069-021-05086-w>
- Watson, L. M., Iezzi, A. M., Toney, L., Maher, S. P., Fee, D., McKee, K., Ortiz, H. D., Matoza, R. S., Gestrich, J. E., Bishop, J. W., Witsil, A. J. C., Anderson, J. F., & Johnson, J. B. (2022). Volcano infrasound: progress and future directions. *Bulletin of Volcanology*, *84*, Article 44. <https://doi.org/10.1007/s00445-022-01544-w>
- Wills, G., Nippres, A., Green, D. N., & Spence, P. J. (2022). Site-specific variations in air-to-ground coupled seismic arrivals from the 2012 October 16 explosion at Camp Minden, Louisiana, United States. *Geophysical Journal International*, *231*(1), 243–255. <https://doi.org/10.1093/gji/ggac184>
- Witsil, A. J., & Johnson, J. B. (2020). Analyzing continuous infrasound from Stromboli volcano, Italy using unsupervised machine learning. *Computers & Geosciences*, *140*(January), 104494. <https://doi.org/10.1016/j.cageo.2020.104494>
- Yang, H.-Y., Zhao, L., & Hung, S.-H. (2010). Synthetic seismograms by normal-mode summation: a new derivation and numerical examples. *Geophysical Journal International*, *183*(3), 1613–1632. <https://doi.org/10.1111/j.1365-246X.2010.04820.x>
- Yeh, K. C., & Liu, C. H. (1974). Acoustic-gravity waves in the upper atmosphere. *Reviews of Geophysics*, *12*(2), 193. <https://doi.org/10.1029/RG012i002p00193>

Chapter 2: Reconstructing the Dynamics of the Highly Similar May 2016 and June 2019 Iliamna Volcano (Alaska) Ice–Rock Avalanches from Seismoacoustic Data[†]

2.1 Abstract

Surficial mass wasting events are a hazard worldwide. Seismic and acoustic signals from these often remote processes, combined with other geophysical observations, can provide key information for monitoring and rapid response efforts and enhance our understanding of event dynamics. Here, we present seismoacoustic data and analyses for two very large ice–rock avalanches occurring on Iliamna Volcano, Alaska (USA), on 22 May 2016 and 21 June 2019. Iliamna is a glacier-mantled stratovolcano located in the Cook Inlet, ~ 200 km from Anchorage, Alaska. The volcano experiences massive, quasi-annual slope failures due to glacial instabilities and hydrothermal alteration of volcanic rocks near its summit. The May 2016 and June 2019 avalanches were particularly large and generated energetic seismic and infrasound signals which were recorded at numerous stations at ranges from ~ 9 to over 600 km. Both avalanches initiated in the same location near the head of Iliamna’s east-facing Red Glacier, and their ~ 8 km long runout shapes are nearly identical. This repeatability — which is rare for large and rapid mass movements — provides an excellent opportunity for comparison and validation of seismoacoustic source characteristics. For both events, we invert long-period (15–80 s) seismic signals to obtain a force-time representation of the source. We model the avalanche as a sliding block which exerts a spatially static point force on the Earth. We use this force-time function to derive constraints on avalanche acceleration, velocity, and directionality, which are compatible with satellite imagery and observed terrain features. Our inversion results suggest that the avalanches reached speeds exceeding 70 m s^{-1} , consistent with numerical modeling from previous Iliamna studies. We lack sufficient local infrasound data to test an acoustic source model for these processes. However, the acoustic

[†]Toney, L., Fee, D., Allstadt, K. E., Haney, M. M., & Matoza, R. S. (2021). Reconstructing the dynamics of the highly similar May 2016 and June 2019 Iliamna Volcano (Alaska) ice–rock avalanches from seismoacoustic data. *Earth Surface Dynamics*, 9(2), 271–293. <https://doi.org/10.5194/esurf-9-271-2021>

data suggest that infrasound from these avalanches is produced after the mass movement regime transitions from cohesive block-type failure to granular and turbulent flow — little to no infrasound is generated by the initial failure. At Iliamna, synthesis of advanced numerical flow models and more detailed ground observations combined with increased geophysical station coverage could yield significant gains in our understanding of these events.

2.2 Introduction

Surficial gravitational mass movements, such as debris flows, rockfalls, lahars, and avalanches, constitute a broad collection of Earth processes which are a significant hazard around the world (Voight, 1978). These events can cause devastating damage to life and property when they occur in at-risk, populated areas in mountainous regions or on the flanks of volcanoes. Avalanches involving mixtures of ice and rock are a subset of these processes usually occurring in topographically extreme, glaciated terrain. Some of the most deadly surficial gravitational mass movements (hereafter, just “mass movements”) in history were ice-rock avalanches. For example, the Huascarán avalanches occurring in 1962 and 1970 in the Peruvian Andes together claimed an estimated 22,000 lives (Plafker & Ericksen, 1978). However, due to their high mobility and frequently remote location, eyewitness observations of these dramatic processes are rare (Caplan-Auerbach & Huggel, 2007; Coe et al., 2016), and other assessment methods such as geologic mapping or satellite imagery analysis may not be timely or even possible due to the rugged terrain and volatile mountain weather typically found in such settings.

Seismoacoustics is an emerging tool which can help us understand these powerful yet elusive processes (K. E. Allstadt et al., 2018, and references therein). Mass movements transfer energy into the solid Earth as seismic waves and into the atmosphere as acoustic waves. The atmospheric waves are primarily in the infrasonic range at frequencies below the range of human hearing (< 20 Hz). These signals contain valuable and complementary information about the character and size of the event and also provide a high-resolution record of event

timing. Most mass movements large enough to be destructive can be recorded seismoacoustically from sufficiently safe distances. By analyzing the seismic and acoustic waves generated by these processes, we can better understand their dynamics and work towards improved hazard mitigation and response. Seismology and infrasound are, therefore, some of the most promising tools for near-real-time detection and characterization of remote mass movements (K. E. Allstadt et al., 2018). However, development of detailed seismoacoustic source models is still an area of active research, as relatively few well-recorded events — particularly those with both seismic and infrasound data — exist.

Here, we focus on two ice-rock avalanches that occurred in May 2016 and June 2019 on Iliamna Volcano, Alaska, USA. These avalanches were very large, each measuring ~ 8 km from crown to toe. Both events produced energetic seismic and acoustic signals broadly recorded at local (< 100 km) and regional (> 100 km) distances. Relatively dense regional seismic and acoustic networks were in place during these events (Figure 2.1), providing a unique opportunity for source quantification and comparison. Additionally, the location and nature of failure and the material, shape, and size of the resulting deposits are very similar between the two events (Figure 2.2), providing excellent datasets for comparison. Iliamna Volcano is known for frequent, large mass movements of this nature (e.g., Caplan-Auerbach & Huggel, 2007; Caplan-Auerbach et al., 2004; Huggel et al., 2007; Schneider et al., 2010).

In this study, we describe the acoustic and seismic signals generated by the 2016 and 2019 Iliamna Volcano avalanches, along with auxiliary information including aerial, ground-based, and satellite imagery. We explore the timing and strength of the avalanche acoustic signal and assess the possibility of acoustic source directionality. We invert the strong long-period seismic signals produced by the events to obtain the time series of forces that the center of mass (COM) of each avalanche exerted on the Earth — the “force-time function”. From there, we calculate the acceleration, velocity, and displacement of the COMs and compare these to auxiliary data such as digital elevation models and satellite imagery. Our modeled forces

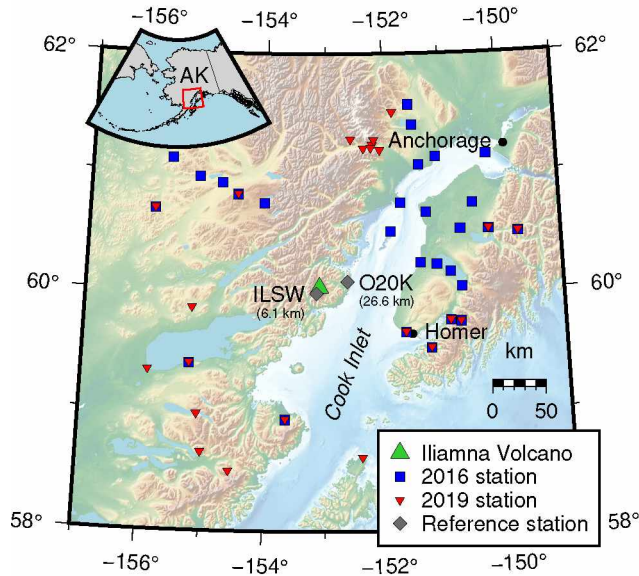


Figure 2.1 Map of the Cook Inlet region, Alaska. Iliamna Volcano is indicated by a green triangle. Broadband seismic stations used in the 2016 (28 stations) and 2019 (23 stations) force inversions are shown as blue squares and red inverted triangles, respectively. Overlapping markers denote stations used in both inversions. The station distribution varies greatly between the two events due to the presence of a temporary seismic array in 2016 and increased Transportable Array station coverage in 2019. Reference stations ILSW and O20K (the closest seismometer and infrasound sensor to the events, respectively) are shown as gray diamonds with distances to Iliamna Volcano given in parentheses. The city of Anchorage and town of Homer are marked as black dots. The red box in the inset shows the main map extent.

and trajectories generally agree well with the satellite imagery and observed terrain features and offer insight into the seismoacoustic source properties of these massive avalanches.

2.3 Background

2.3.1 Analysis of Long-Period Seismic Waves from Mass Movements

The amplitude and frequency content of the seismic wavefield radiated by a surficial mass movement are strongly controlled by the spatial and temporal scales involved as well as the structural coherence of the moving material. Processes such as powdery snow avalanches and lahars, which primarily involve incoherent collections of fine-grained particles, produce relatively high frequency seismicity (K. E. Allstadt et al., 2018). However, larger events which

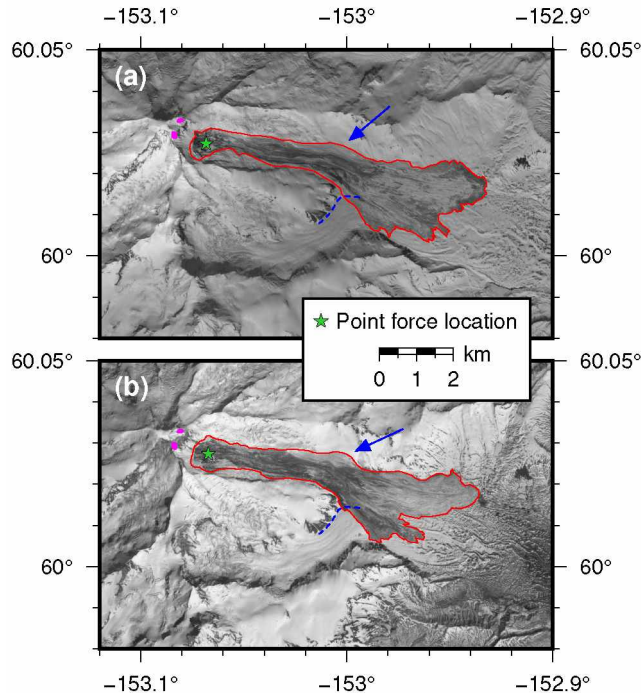


Figure 2.2 Satellite images of the 2016 and 2019 Red Glacier avalanche deposits acquired on (a) 23 May 2016 and (b) 22 June 2019, both less than 48 h post-event. Red outlines delineate approximate avalanche extents (source, track, and deposit areas). Green stars mark the location of the inversion point force. Blue arrows indicate the location of super-elevation-like flow lobes. Blue dashed lines delineate the northern margin of an unnamed tributary glacier which joins Red Glacier from the southwest. Magenta patches show the approximate locations of two fumarole zones located to the east of the summit. Imagery © 2016 and 2019 Planet Labs, Inc.

move coherently — such as rockfalls and ice-rock avalanches — can additionally produce significant long-period (> 10 s) seismic energy that can be recorded globally (K. E. Allstadt et al., 2018; Hibert et al., 2017). These long-period seismic waves originate from the bulk acceleration and deceleration of the mass as it moves downslope (Ekström & Stark, 2013).

Long-period seismic waves can be used to invert for quantitative mass movement source properties. The wave propagation (i.e., Green’s function) at these periods is often straightforward to model due to the relatively small influence of topography and Earth structure on such long-wavelength signals. Once the propagation is accounted for, one can invert for the time-varying force vector that the moving mass exerted on the Earth (e.g., K. E. Allstadt, 2013; Coe et al., 2016; Ekström & Stark, 2013; Gualtieri & Ekström, 2018; Kawakatsu, 1989).

The trajectory can then be obtained if the mass, generally assumed to be constant, is known or can be estimated (e.g., Ekström & Stark, 2013; Gualtieri & Ekström, 2018; Moore et al., 2017; Schöpa et al., 2018). However, complexities such as entrainment and deposition along the flow path clearly violate the constant mass approximation, so this method has generally only been successful for simple runout paths. The infrequent nature of mass movements capable of generating sufficiently long-period seismic radiation means that opportunities to apply this model are limited (Hibert et al., 2017).

2.3.2 Acoustic Studies of Mass Movements

More recently, studies have incorporated observations and analysis of infrasound generated by mass movements. Because infrasound stations are often deployed in volcano-monitoring settings (Fee & Matoza, 2013; Matoza et al., 2019), many acoustic observations of mass movements have documented volcanic phenomena such as pyroclastic flows (e.g., Delle Donne et al., 2014; Ripepe et al., 2009, 2010; Yamasato, 1997), lahars (e.g., Johnson & Palma, 2015), rockfalls (e.g., Johnson & Ronan, 2015; Moran et al., 2008), and flank collapse events (e.g., Perttu et al., 2020). Outside of the volcanic context, debris flows (e.g., Kogelnig et al., 2014; Marchetti et al., 2019; Schimmel & Hübl, 2016), powder snow avalanches, (e.g., Havens et al., 2014; Marchetti et al., 2015, 2020; Ulivieri et al., 2011), non-volcanic rockfalls (e.g., Zimmer et al., 2012; Zimmer & Sitar, 2015), and rock avalanches (e.g., Moore et al., 2017) have been observed acoustically. Infrasound recordings of surficial mass flows at regional distances are rare.

Infrasonic source directionality has previously been assessed for dense recordings of volcanic explosions. For example, Iezzi et al. (2019) performed a multipole acoustic source inversion on explosions from Yasur volcano, Vanuatu, describing the source as a combination of monopole (uniform radiation) and dipole (directional radiation) components. Mass movement acoustic radiation has been suggested to be highly directional and potentially described by an acoustic dipole (K. E. Allstadt et al., 2018; Haney et al., 2018). However, assessment

of acoustic source directionality for mass movements requires dense station coverage, which is not usually available (Iezzi et al., 2019); therefore, the actual source directionality has not been validated with data. Additionally, beyond local distances, path effects from the usually highly spatiotemporally variable atmosphere become important. These effects can mask source directionality or produce spurious source directionality and must be considered in analyses (e.g., Perttu et al., 2020).

Arrays of infrasound sensors can be used to determine the backazimuth of incident acoustic waves and can track flow fronts in certain circumstances (e.g., Johnson & Palma, 2015; Marchetti et al., 2020). Though infrasonic records of mass movements are becoming more common, the relevant acoustic source theory is currently underdeveloped (K. E. Allstadt et al., 2018). Very simple mass movements such as rockfalls have been treated as monopoles (e.g., Moran et al., 2008), but often the source of infrasound is moving and distributed, complicating modeling. Marchetti et al. (2019) modeled a debris flow as a linear series of monopole sources in motion, but found that infrasound array processing results always pointed back to fixed locations corresponding to check dams in the debris flow drainage, the most acoustically energetic sources. Using infrasound arrays, Johnson and Palma (2015) tracked a lahar which registered as a moving source until it encountered a topographic notch, at which point the source location became fixed on this acoustically “loud” flow feature. The dynamic, spatiotemporal variability of the atmosphere also complicates infrasound source modeling (Poppeliers et al., 2020). These studies highlight the challenge in determining the source of mass-movement-generated infrasound.

2.3.3 Ice–Rock Avalanches

Ice–rock avalanches are a subset of mass movements which consist of rapid flows of pulverized ice and rock. Though the initial failure of an ice–rock avalanche can free larger blocks of material, such blocks quickly disintegrate into small fragments of rock and ice as they impact asperities in the flow path at speed. This debris travels on a saturated, low-

strength layer of material, increasing avalanche mobility (Hungre et al., 2014). Additionally, since these processes often take place in steep, heavily glaciated terrain (Schneider et al., 2011), the avalanches commonly flow over glaciers. This further enhances mobility due to the low friction of glacier ice (Schneider et al., 2010). Debris avalanches involving volcanic rocks can be especially mobile due to the weakened edifice rock of which they are composed, which more readily transforms to low-internal-friction granular flow (Davies et al., 2010). Owing to their high mobility and often large volumes (Hungre et al., 2014; Schneider et al., 2011), debris avalanches such as ice–rock avalanches are among the most seismogenic types of mass movements (K. E. Allstadt et al., 2018).

2.3.4 Iliamna Volcano, Alaska

Iliamna Volcano (hereafter, “Iliamna”) is a 3,053-meter-tall stratovolcano located in the Cook Inlet region of south-central Alaska, USA (Figure 2.1). The volcano lies about 215 km from the city of Anchorage, and roughly 100 km across the Cook Inlet from the town of Homer. The geology of Iliamna consists primarily of stratified andesitic lava flows with smaller contributions from mass wasting deposits of various types. The volcano’s summit is perennially mantled with snow and ice, and its edifice hosts several large valley glaciers (C. F. Waythomas & Miller, 1999). Two zones of sulfurous fumaroles located on the eastern side of Iliamna’s summit (see magenta patches in Figure 2.2) emit steam and volcanic gas quasi-continuously (Werner et al., 2011).

Though Iliamna has not erupted in historical time, it experienced two periods of seismic unrest occurring in 1996 and 2012, which were interpreted as magmatic intrusions and failed eruptions (Herrick et al., 2014; Roman et al., 2004). Additionally, the deeply dissected and hydrothermally altered edifice of Iliamna hosts frequent mass wasting events. Geologic evidence of late Holocene lahars and debris avalanches is abundant (C. Waythomas et al., 2000), and Iliamna has experienced at least 12 very large (horizontal runout length $L > 5$ km) ice–rock avalanches since 1960 (K. Allstadt et al., 2017; Huggel et al., 2007). Ten of

these 12 events occurred on Iliamna’s east-facing Red Glacier. These avalanches typically fail in ice or at the ice–bedrock interface near the base of the hydrothermally altered fumarole zones near the summit. The avalanches are relatively frequent, with a recurrence interval of 2–4 years. This interval may be linked to the “recharging” time required for ice thickness to grow until shear stress exceeds shear strength (Huggel et al., 2007).

Iliamna’s ice–rock avalanches have been extensively studied via geologic mapping, multi-spectral satellite image analysis, numerical modeling, and seismic analysis. Geologic investigations by C. Waythomas et al. (2000) revealed that late Holocene debris avalanche deposits composed of hydrothermally altered rock are present in most of Iliamna’s glacier-filled valleys. From the thin, blanket-like appearance of these deposits, C. Waythomas et al. (2000) inferred that the original avalanches likely contained a significant amount of snow or ice in addition to rock. Caplan-Auerbach et al. (2004) documented the seismic signals associated with four very large Iliamna ice–rock avalanches. They found the signals to be remarkably similar, each exhibiting a precursory pattern of 20–60 min of repeating discrete events which become closer together in time, culminating with a high-amplitude emergent-onset waveform corresponding with the actual failure. This precursory phenomenon was explored further by Caplan-Auerbach and Huggel (2007), who defined four phases of precursory activity:

1. Crevasse opening, with minimal seismic energy release.
2. Acceleration of glacier movement.
3. Discrete slipping, manifested as repeating seismogenic stick-slip events.
4. Continuous slipping, which begins about 0.5–1 h prior to failure.

Caplan-Auerbach and Huggel (2007) also suggested that Iliamna’s glaciers are affected by volcanogenic heating, enabling them to fail on slopes shallower than the 45° threshold broadly assumed to be the minimum slope for cold-ice failure (Huggel et al., 2004). Huggel et al. (2007) found that satellite-derived thermal anomalies in Iliamna’s summit region were

spatially correlated with zones of fumarolic activity and hydrothermally altered rocks. Huggel et al. (2007) and Schneider et al. (2010) used successively more sophisticated numerical flow models to reconstruct a very large 2003 Red Glacier avalanche. Both studies were able to recreate flow features persistently observed for Red Glacier events since 1960, such as multiple distal flow lobes (toes) and prominent superelevation-like flow lobes on the orographically downslope left side of the flow.

2.4 Data

On 22 May 2016 at 07:58 UTC (about midnight local time; hereafter, all times in UTC unless otherwise noted), the Alaska Volcano Observatory (AVO) recorded emergent-onset seismic signals across Iliamna’s local monitoring network, and a subsequent pilot report confirmed that a large mass movement had occurred. A Landsat 8 image acquired the following day revealed a large dark-colored deposit on Red Glacier; this deposit was also visible from Homer (Figure 2.3a). A horizontal crown-to-toe runout length L of 8.5 km and a vertical drop height H of 1.7 km were estimated from follow-up imagery analysis, resulting in an H/L ratio of 0.2.

On 21 June 2019 at 00:03, AVO recorded signals on Iliamna’s seismic network indicative of another large avalanche. Photos from citizen overflights taken in the following several days (Figure 2.3b and c) showed a large deposit on Red Glacier. Satellite imagery analysis produced values of $L = 8.1$ km and $H = 1.7$ km (H/L ratio of 0.2). The combined source, track, and deposit areas for these two avalanches are delineated in Figure 2.2.

The 2016 and 2019 Iliamna ice–rock avalanches are well documented due to the relatively accessible nature of the volcano — by Alaska standards — as well as the exceptional instrument coverage afforded by several permanent and temporary seismoacoustic networks. Our seismoacoustic observations and interpretations were assisted by high-resolution (meter-scale, daily revisit) satellite imagery, aerial and ground-based imagery acquired fortuitously

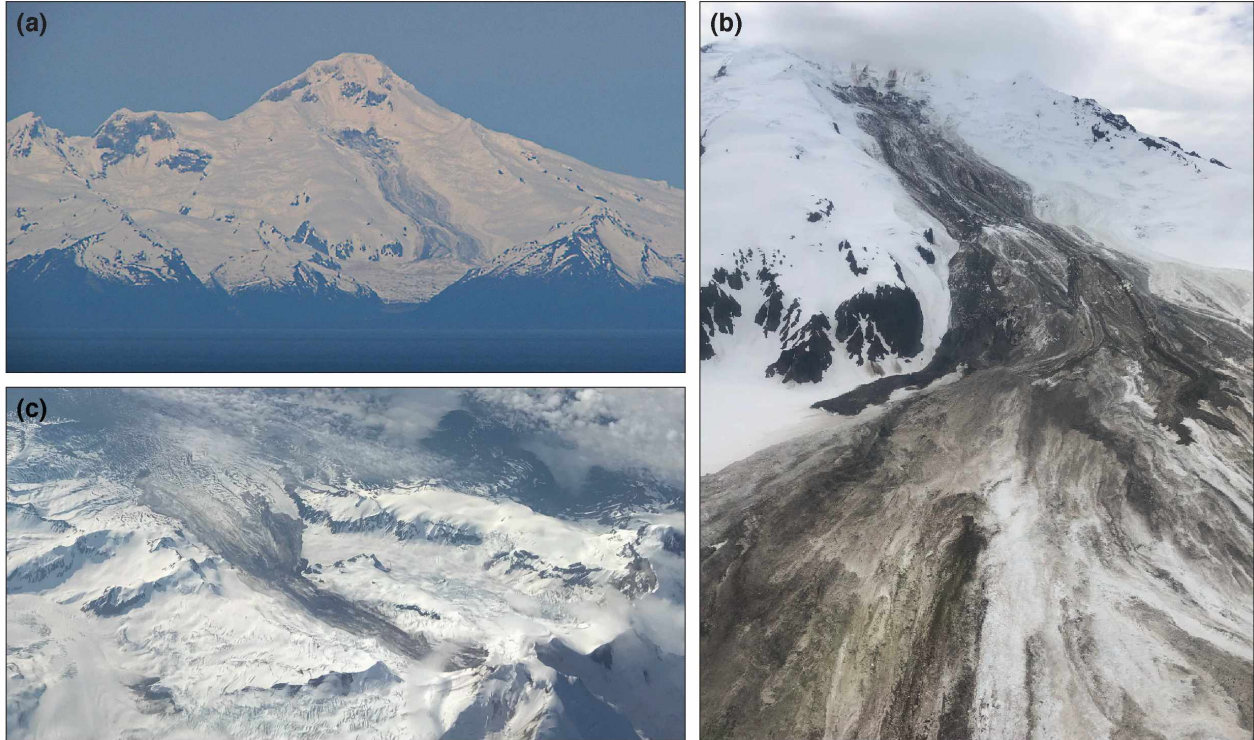


Figure 2.3 Photographs of the 2016 and 2019 Red Glacier avalanche deposits. **(a)** West-northwest-looking photograph of the 2016 deposit taken from near Homer on 23 May 2016. Photo courtesy Dennis Anderson, Night Trax Photography; Alaska Volcano Observatory (AVO) image database ID 95521. **(b)** West-northwest-looking aerial photograph of the 2019 deposit, taken 22 June 2019. Photo courtesy Loren Prosser; AVO image database ID 140871. **(c)** Southeast-looking aerial photograph of the 2019 deposit, taken 25 June 2019. Photo courtesy Greg Johnson; AVO image database ID 141431.

or opportunistically in the days following the events, and high-resolution (sub-meter-scale) elevation data.

2.4.1 Seismic Signals

Seismic signals from the events were broadly recorded on local and regional networks. Stations in the EarthScope USArray Transportable Array (network code TA), AVO (network code AV; Power et al., 2020), and Alaska Earthquake Center (AEC; network code AK) networks recorded signals from both events. The temporary Southern Alaska Lithosphere and Mantle Observation Network (SALMON; network code ZE; Tape et al., 2017), which was

deployed from 2015–2017, captured the 2016 event. Additionally, stations in the National Tsunami Warning Center (network code AT), temporary Alaska Amphibious Community Seismic Experiment (network code XO), and Global Seismograph Network (GSN; network code II) networks recorded one or both of the events. Most stations which recorded the signal were broadband (120 s corner period) three-component sensors.

AVO station ILSW, at ~ 6 km from the avalanche crowns (Figure 2.1), was the closest seismometer with usable data in both 2016 and 2019. We note here that due to the size and mobility of these avalanches, source-to-station distances change drastically over the course of the event; ILSW is ~ 12 km from the toes of the deposits. Vertical-component spectrograms and waveforms of avalanche seismic signals recorded at this station are shown in Figure 2.4. Multiple high-frequency transients are visible in the spectrograms prior to the main event, indicative of precursory stick-slip activity which has been observed for previous Red Glacier avalanches and is thoroughly explored in Caplan-Auerbach and Huggel (2007). The main event waveforms have an emergent onset characteristic of mass movement seismic signals (K. E. Allstadt et al., 2018). This same shape, albeit with a lower signal-to-noise ratio (SNR), is found on all stations which recorded the event. The events also produced prodigious long-period energy with a dominant period of 35 s (Figure 2.5). In this manuscript we do not analyze the precursory stick-slip activity observed for the 2016 and 2019 avalanches.

2.4.2 Acoustic Signals

The 2016 and 2019 events produced strong infrasound signals which were recorded out to distances exceeding 600 km (Figure 2.6). Signals were observed on select infrasound “single station” sensors of the TA, GSN, and AEC networks, as well as regional arrays operated by AVO and one International Monitoring System (network code IM) array. The nearest infrasound sensor at the time was TA station O20K (Figure 2.1) at ~ 19 and ~ 26 km from the avalanche toes and crowns, respectively.

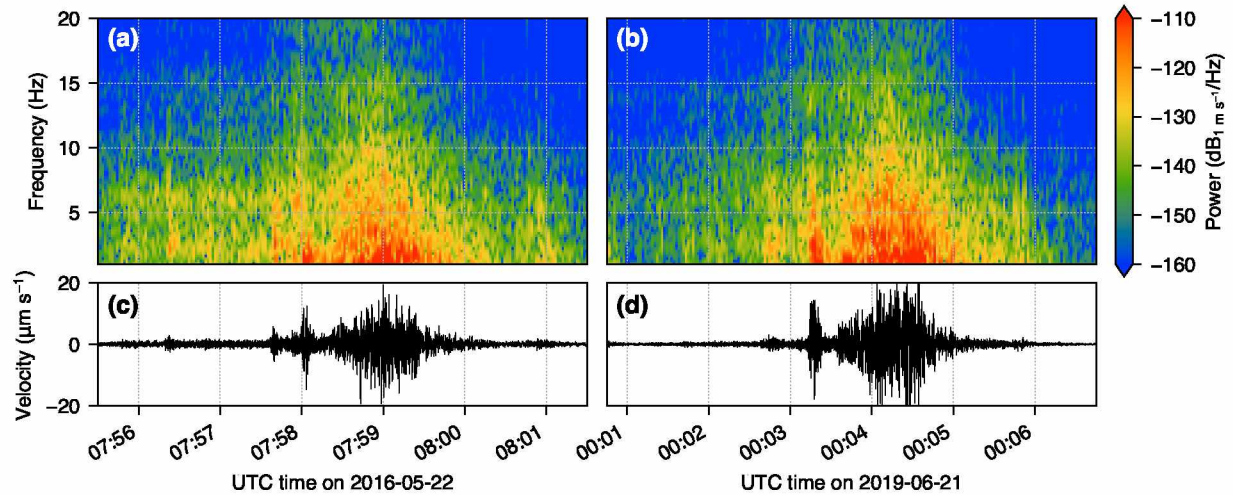


Figure 2.4 Vertical-component spectrograms (a, b) and seismic waveforms (c, d) from Alaska Volcano Observatory station ILSW for the 2016 (left column) and 2019 (right column) avalanches. Waveforms are highpass filtered at 100 s.

“Waterfall” plots of the infrasound signal at station O20K in different frequency bands for the 2016 and 2019 events are shown in Figure 2.7 and illustrate the signal’s broadband nature. The dominant frequency of the signal is about 0.5 Hz, but energy exists from 100 s up to 10 Hz (the Nyquist frequency for this station). In 2016, the ~ 120 s duration of the high-frequency signal (2–10 Hz, red line) is nearly twice that of the longer-period signal (0.01–0.1 Hz, blue line). The 2016 and 2019 signals are of similar amplitudes, but in 2019 the noise level is higher in the 0.01–0.1 and 2–10 Hz bands (Figure 2.7b).

2.4.3 Aerial Photos, Satellite Imagery, and Elevation Data

We interpret image data from three sources to augment our waveform-based analyses. Our satellite image sources are the Planet Labs PlanetScope (3-meter resolution) and RapidEye (5-meter resolution) satellite constellations and the DigitalGlobe WorldView-3 (WV-3, sub-meter resolution) satellite. We use the near-infrared band (NIR) from Planet Labs images acquired less than 48 h following each event (23 May 2016 and 22 June 2019) to constrain the dimensions of the source and deposit areas for each avalanche (Figure 2.2). Fortunately, cloud cover was minimal during this time window. A panchromatic WV-3 image from 22 June

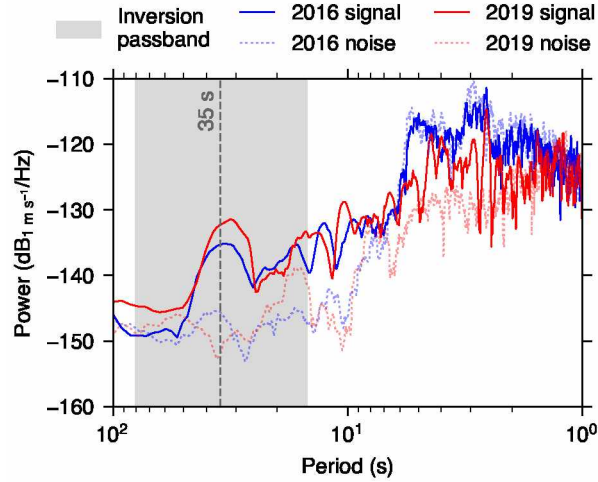


Figure 2.5 Power spectral densities (PSDs) of vertical-component seismic signals from the 2016 (blue lines) and 2019 (red lines) avalanches. The signals were recorded on Alaska Earthquake Center station HOM, the closest station to Iliamna Volcano used in both force inversions. Dotted lines are the PSDs for a 1000 s post-avalanche time window and indicate the approximate contemporaneous noise level. Gray box indicates the force inversion passband (15–80 s).

2016 captured the finer details of the source and deposit, though we note that melting of the icy portion of the deposit as well as additional smaller mass movements during the month between the 2016 avalanche and acquisition of the WV-3 image complicate our analysis of the image.

The 2016 and 2019 deposits were readily visible from Homer (Figure 2.3a). Members of the community captured oblique aerial photos of the 2019 event during flyovers on 22 and 25 June 2019 (Figure 2.3b and c). Additionally, in late July 2019, National Park Service and AVO staff flew a structure from motion (SfM) mission in the area around Iliamna, capturing about 4,400 photos of the edifice and Red Glacier areas that were used to produce a 70 cm resolution digital elevation model (DEM). The DEM extent completely covers the total areas of both events. We use this DEM in our analysis with the caveat that the bed surface of Red Glacier is highly dynamic due to erosion from mass movements as well as glacial activity; the DEM is therefore more applicable to the 2019 event than the 2016 event.

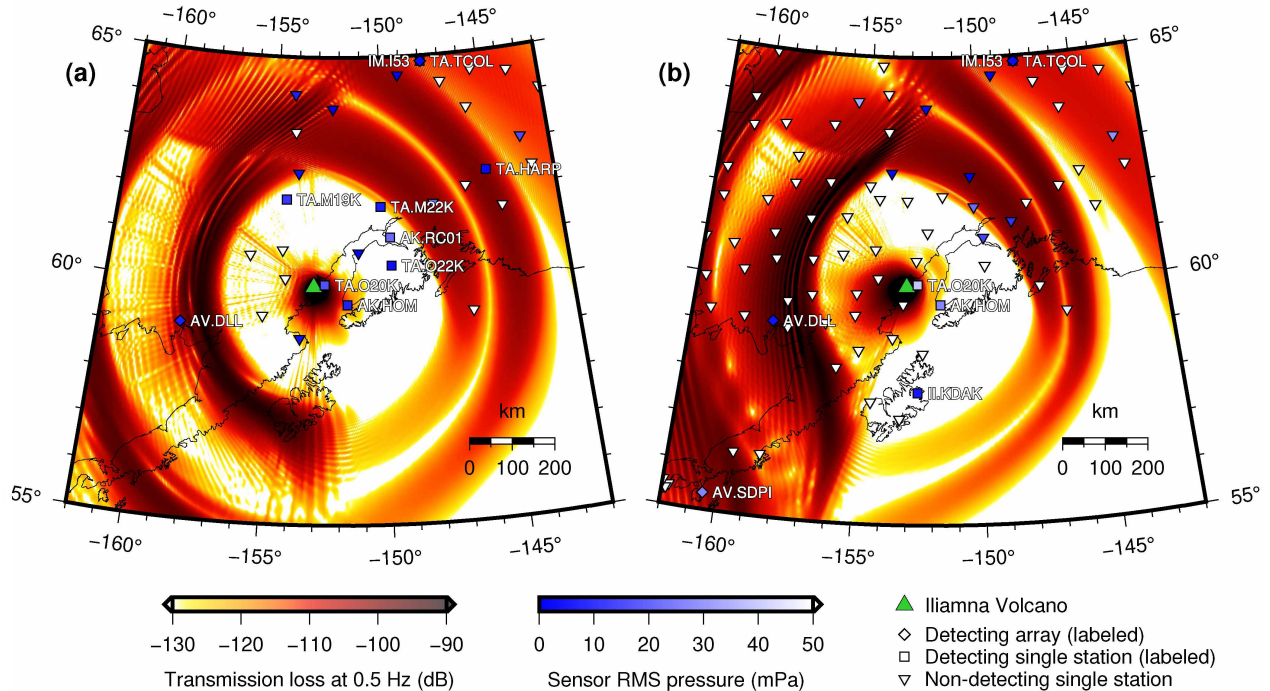


Figure 2.6 Acoustic transmission loss at the Earth’s surface, modeled at 0.5 Hz for the (a) 2016 and (b) 2019 avalanches. The atmospheric model is a single sonde (1D atmospheric profile) over the avalanche path midpoint. Iliamna Volcano is indicated by a green triangle. Diamonds/squares denote arrays/stations where the avalanche signal was detected. Inverted triangles indicate other infrasound stations where no signal was observed. The blue shades on the station markers indicate root-mean-square (RMS) pressure in the 0.5–2 Hz band for hour-long windows prior to the predicted true arrival. This is a proxy for local site noise. (See §2.4 for description of network codes.)

2.5 Methods

2.5.1 Mass Estimation

We use the satellite imagery shown in Figure 2.2 to estimate the mass for each event. We are unable to perform DEM subtraction to obtain a volume for either event due to insufficient data. Instead, we delineate the depositional area and assume a uniform (1.5 ± 1) m deposit thickness everywhere on the slope to obtain a volume. Red Glacier avalanche deposits are typically on the order of a few meters thick (Huggel et al., 2007; C. Waythomas et al., 2000), so this represents a reasonable estimate. We then multiply this volume by the density of a mixture of 50% ice (density 920 kg m^{-3}) and 50% rock (density 2500 kg m^{-3}) to obtain mass

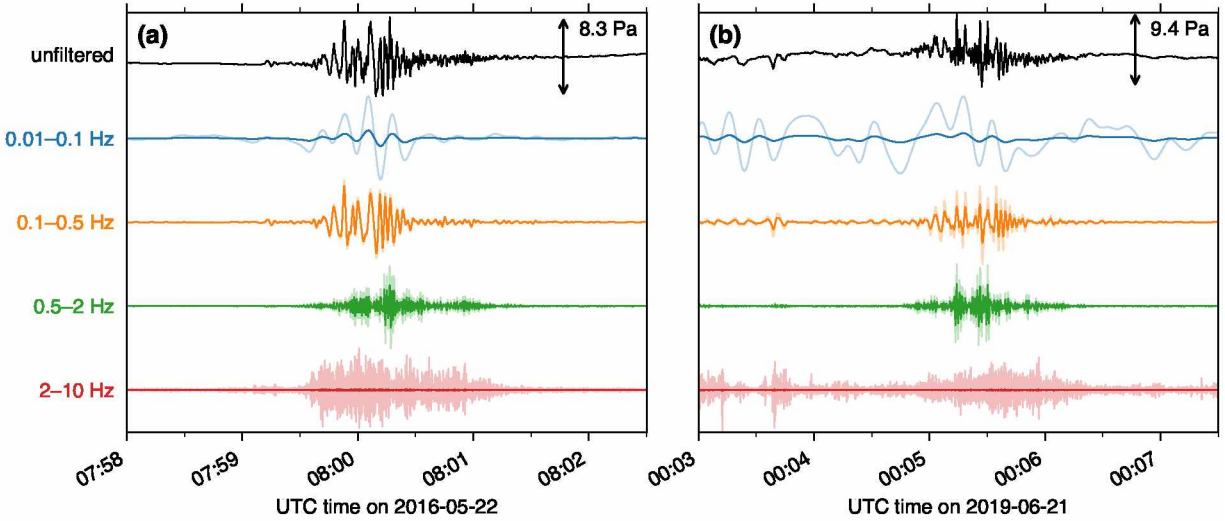


Figure 2.7 Infrasound signals in different frequency bands for the (a) 2016 and (b) 2019 avalanches. Signals were recorded on the Transportable Array station O20K, the closest infrasound sensor to Iliamna Volcano at the time. Signals plotted as solid lines are normalized relative to the black unfiltered trace. Translucent lines are individually normalized signals.

estimates. This assumed mixture is based upon the color of the deposits seen in Figure 2.2 as well as the composition inferred for previous Red Glacier avalanches (C. Waythomas et al., 2000).

2.5.2 *Infrasound Analyses*

Infrasound signals travel in atmospheric waveguides created primarily by vertical gradients in temperature and horizontal winds (Drob et al., 2003). The presence or absence of such waveguides in a given propagation direction from the source strongly controls our ability to detect and characterize infrasonic signals (Fee et al., 2013). Furthermore, cultural and natural noise, especially locally sourced wind noise, can obscure a true signal. Just as in seismology, our goal for source studies is to isolate source properties from path and station effects. To achieve this for the Iliamna avalanches, we model infrasound propagation conditions and assess station noise levels for time periods surrounding each event.

We use the AVO-G2S (ground-to-space) open-source atmospheric specification (github.com/usgs/volcano-avog2s; Schwaiger et al., 2019) to examine infrasound propagation from the avalanches. We extract a 1D atmospheric profile above the avalanche path midpoint for the forecast hours of 22 May 2016 08:00 and 21 June 2019 00:00. AVO-G2S smoothly merges lower-atmosphere numerical weather prediction (NWP) products with upper-atmosphere empirical climatologies. We use the ERA5 NWP model from the European Centre for Medium-Range Weather Forecasts. The upper atmosphere winds and temperature in AVO-G2S are defined by the 2014 update to the Horizontal Wind Model (Drob et al., 2015) and the NRLMSISE-00 atmospheric model, respectively. The output 1D profile defines temperature, zonal (east–west) and meridional (north–south) winds, density, and pressure as a function of altitude.

We then use the aforementioned profiles and the Modess code from NCPAprop (github.com/chetzer-ncpa/ncpaprop; Waxler et al., 2017) to model infrasonic transmission loss on the Earth’s surface in the region around Iliamna. The transmission loss (TL) is the accumulated sound pressure loss as a function of range and height, expressed in decibels (dB). Modess solves a generalized Helmholtz equation for the propagation of a monochromatic pulse in a stratified (i.e., 1D) atmosphere. The method of normal modes is used to solve the equation, which uses the “effective sound speed approximation” — that is, the sum of the static sound speed and the along-path contribution of the horizontal wind field define the effective sound speed. We choose a 0.5 Hz frequency for modeling, because that is the dominant frequency of the observed acoustic signal, and we set the source height at 900 m, the approximate elevation of the midpoint of the avalanche paths. We compute the surface acoustic TL in dB from 0–1000 km range for azimuths of 0–360° in 1° increments. We then map the data from range–azimuth space (with the origin being Iliamna) to longitude–latitude on the WGS84 ellipsoid and grid the result to produce continuous TL maps for the two events (Figure 2.6).

To assess the effect of local station noise on signal detection for single infrasound stations, we compute root-mean-square (RMS) pressure in the 0.5–2 Hz band on hour-long windows for each infrasound-equipped station within 900 km of Iliamna (see blue color scale in Figure 2.6). We remove the instrument response, detrend, and taper the data prior to filtering. Windows are defined to sample the data in the hour immediately preceding signal arrival at a given station to avoid possible upwards biasing of extremely quiet stations by the avalanche signal itself. This is guaranteed by specifying a maximal acoustic celerity (distance / travel time) of 350 m s^{-1} to define the moveout of the window end time. We remove stations with excessive glitches or dead channels (5 stations in 2016; 3 stations in 2019).

2.5.3 Force Inversions

We invert the long-period seismic signals generated by these events to obtain the time-varying forces that the avalanche COMs exerted on the Earth. We use a version of the approach detailed in K. E. Allstadt (2013) and applied in Coe et al. (2016). We model the avalanche as a block sliding down a slope experiencing a net force given by the balance between the slope-parallel gravitational and dynamic friction forces. By Newton’s second law, this net force is equal and opposite to the time-varying force that the avalanche COM exerts on the Earth (K. E. Allstadt, 2013). In our model, this avalanche “force-time function” is applied to the Earth as a spatially static point force, which is valid for long-wavelength signals where the shift in source location due to mass motion is small relative to the signal wavelength. We define the point force location to be the COM of the avalanche source region (see §2.5.4 and green stars in Figure 2.2).

We use data from seismic stations within 80–200 km of Iliamna. We omit all stations less than 80 km from the source because we know from satellite imagery that the COM locations for both avalanches moved up to 8 km. This constraint ensures that we only use stations for which the source-to-station distance changed by a maximum amount of 10% over the course of the event, allowing us to consider the landslide source as a point force. Limiting

our station search to 200 km results in a data volume sufficient to constrain the source yet small enough to make manual signal inspection feasible. Prior to inspection, waveforms were detrended using a second-order polynomial and rotated into the vertical–radial–transverse (Z–R–T) reference frame. We additionally deconvolve the instrument response to obtain units of displacement and apply a 15–80 s bandpass filter. The passband was selected to avoid noise associated with the secondary microseism (3–10 s, Gualtieri et al., 2015) and to ensure that the maximum period of the filtered signals is below the corner period of the seismometers used. After this processing, we select waveforms with sufficient SNR by visual inspection. This left us with 28 stations in 2016 and 23 stations in 2019.

We predict the ground displacements at each station by convolving the force-time function with the Green’s functions (GFs) between the point force location and each station. We use the wavenumber integration method, as implemented in Computer Programs in Seismology (Herrmann, 2013), to calculate the GFs from the ak135-f radial Earth velocity model (Kennett et al., 1995; Montagner & Kennett, 1996). For each station, the GFs describe the 3D displacement as a function of time induced by a unit impulse force at the source location. We filter the GFs in the same manner as the data. Mathematically, the three-component ground displacement time series predicted for a station, $\mathbf{u}(t) = [u_Z(t), u_R(t), u_T(t)]$, is given by the convolutions

$$u_Z(t) = [f_N(t) \cos \phi + f_E(t) \sin \phi] * g_{ZH}(t) + f_Z(t) * g_{ZV}(t), \quad (2.1)$$

$$u_R(t) = [f_N(t) \cos \phi + f_E(t) \sin \phi] * g_{RH}(t) + f_Z(t) * g_{RV}(t), \text{ and} \quad (2.2)$$

$$u_T(t) = [f_N(t) \sin \phi - f_E(t) \cos \phi] * g_{TH}(t), \quad (2.3)$$

where the symbol $*$ denotes convolution (Herrmann, 2013). $\mathbf{f}(t) = [f_Z(t), f_N(t), f_E(t)]$ is the 3D force-time function exerted on the Earth by the avalanche in terms of vertical (Z), north (N), and east (E) components, and ϕ is the source-to-station azimuth measured clockwise from north. The Green’s functions $g_{ZV}(t)$, $g_{ZH}(t)$, $g_{RV}(t)$, $g_{RH}(t)$, and $g_{TH}(t)$ describe how

vertical (Z), radial (R), and transverse (T) components of displacement are excited by vertical (V) and horizontal (H) force impulses. We set the sampling interval of $\mathbf{f}(t)$ to 1 second.

We invert for $\mathbf{f}(t)$ using a higher-order Tikhonov-regularized approach which we describe in detail in Appendix 2.10.

2.5.4 Trajectory Calculations

For simple mass movements, the trajectory can be calculated from the force-time function if the mass is known or can be estimated. The acceleration felt by the avalanche COM is given by Newton’s second law

$$\mathbf{a}(t) = -\frac{\mathbf{f}(t)}{m}, \quad (2.4)$$

where m and $\mathbf{a}(t)$ are the mass and acceleration of the avalanche, respectively. The sign change arises from the fact that $\mathbf{f}(t)$ is equal but opposite to the force felt by the avalanche. Integrating twice with respect to time yields the displacement. Since the avalanche paths are straightforward and we have two stable inversions, we apply the double integration method to obtain trajectories for the 2016 and 2019 events. Note that this method assumes that the mass m is constant, which is clearly not the case due to entrainment and deposition along the path. In this study, we assume that variations in mass are small enough to ignore. We start integration at the zero time and end at 200 s since the forces are essentially zero at this point. Unlike previous inversions, we add an additional, intuitive constraint that the velocity go to zero at the end of avalanche. This was implemented for each component of the velocity by subtracting a linear trend starting at zero at the zero time and ending at the value of the velocity at 200 s. Note that due to the cumulative effect of double integration, even a small amount of noise occurring early in $\mathbf{a}(t)$ can manifest as a large error in the calculated trajectory.

To compare the obtained trajectories with georeferenced data such as satellite imagery and DEMs, we pick a starting location for the COM. Note that the COM start point is not the top of the avalanche crown. We employ a semiautomatic approach in which we use the

Planet Labs NIR imagery to estimate the extent of the source region in Google Earth. We define the source region as the zone spreading from the avalanche crown down to where the scoured surface is no longer evident. We then manually outline this region and calculate the centroid of the resulting polygon. Our COM locations are both less than 500 m from the highest point of the avalanche crown; we estimate our error in specifying the COM location to be of a similar magnitude.

Two major sources of uncertainty in the trajectory calculations are related to inversion regularization and the estimated mass used to convert from force to acceleration. The Tikhonov regularization scheme (see Appendix 2.10) biases the amplitudes of $\mathbf{f}(t)$ down from their true values. This means that even if an accurate mass is known, dividing the force-time function by this mass will not recover the true acceleration of the avalanche. To achieve a more realistic trajectory length that is independent of inversion-related biases, we set a target length for the event based on retrospective satellite imagery analysis and iteratively determine the mass that results in this length. The trial mass starts at zero (giving an infinite length) and is increased in increments of 10 million kg until the length calculated with the trial mass drops below the target length. The mass obtained via this iterative process is therefore essentially a scaling factor; it is not physically meaningful.

Gualtieri and Ekström (2018) and Schöpa et al. (2018) also performed force inversions using seismic data and inferred masses from deposit imagery. However, in both of these studies the landslides flowed into water, and the authors chose the shoreline as the COM end point. Our COM end points are less clearly defined, since the avalanche mass spread out and formed flow lobes of unknown thickness (Figure 2.2). Instead of defining a length by explicitly selecting an end point for the COM, which is difficult and subjective due to poor constraints on the thickness of the deposit, we tie salient features in $\mathbf{f}(t)$ to consistent features found in satellite imagery and DEM data, as in K. E. Allstadt (2013) and Coe et al. (2016). In particular, we align a prominent northward force in $\mathbf{f}(t)$ — which is indicative of the avalanche COM applying such a force to the Earth — with the superelevation-like flow

lobe consistently found in both 2016 and 2019 as well as earlier events (see Figure 2.2 and Huggel et al., 2007). We then adjust our target length until the location of this northward force aligns with the lobe apex. Note that this method avoids the explicit identification of a COM end point.

2.6 Results

2.6.1 *Infrasound*

The 2016 avalanche was detected acoustically on two arrays and eight single stations (Figure 2.6a). The 2019 avalanche was detected on three arrays and four single stations (Figure 2.6b). We define an array detection as a signal with high correlation (median cross-correlation maxima > 0.6) across the array and a backazimuth pointing towards Iliamna (see e.g. Bishop et al., 2020, for a discussion of modern array processing techniques). We define a single station detection more qualitatively as a signal with a high SNR (i.e., an unambiguous arrival) in the 0.5–2 Hz band and an acoustic celerity relative to the well-constrained avalanche location and origin time. For both events, at local distances (< 100 km) only stations to the east of Iliamna detected the event. At greater distances (> 200 km), there are detections at many azimuths from the volcano. The larger number of infrasound stations present in 2019 reflects the westward expansion of the TA deployment, as well as an additional operational AVO array at Sand Point (station code SDPI, SW corner of Figure 2.6b).

Infrasound station noise levels varied widely (Figure 2.6), but all detecting stations in 2016 and 2019 had RMS pressure levels not exceeding 40 mPa in the 0.5–2 Hz band. For both events, several stations did not detect the avalanche in spite of having RMS pressure levels less than 40 mPa. Figure 2.6b reveals that many of the stations installed after the 2016 event were noisy during the 2019 event, limiting the effective network size increase from 2016 to 2019. For reference, the maximum signal amplitude in the 0.5–2 Hz band at TA station

TCOL (the farthest detecting single station from Iliamna) is 18 mPa in 2016 and 23 mPa in 2019.

Figure 2.6 shows the acoustic TL predicted at the Earth’s surface for the 2016 and 2019 events. Dark red bands of lower TL correspond to ground surface returns from waveguides in the atmosphere, also known as ducts. In general, propagation conditions differed between the two events within 150 km from Iliamna, becoming more similar at longer ranges. In both years, a strong duct to the west is present, with a low-TL band radially near array DLL. The radial extent of the shadow zone associated with this duct is similar for both years. However, the local preferred propagation direction differs between 2016 and 2019, with sound being guided to the southeast in 2016 and west-southwest in 2019.

In both years, many stations residing in areas of low predicted TL and therefore higher predicted amplitude (e.g. north of M19K in 2016 and north and southeast of DLL in 2019) did not detect the event. Conversely, for both events, stations detected the signal despite being located in a predicted shadow zone, such as O22K in 2016 and KDAK in 2019.

2.6.2 Seismic Inversion and Derivative Results

The force-time functions for the two events are remarkably similar, showing nearly identical timing and relative amplitude (Figure 2.8a–f). The fits of the modeled data to the true data are displayed in Figure 2.9. The variance reduction is 83% for the 2016 inversion and 74% for the 2019 inversion. Gray patches in Figure 2.8a–f denote the minimum and maximum forces derived from the jackknife iterations and indicate that our models are not very sensitive to the choice of input waveforms within our dataset. The overall amplitude of the 2019 event is larger than the 2016 event, consistent with larger seismic waveform amplitudes in 2019 (see Figures 2.4c and d and 2.9). Both results suggest similar durations of about 150 s.

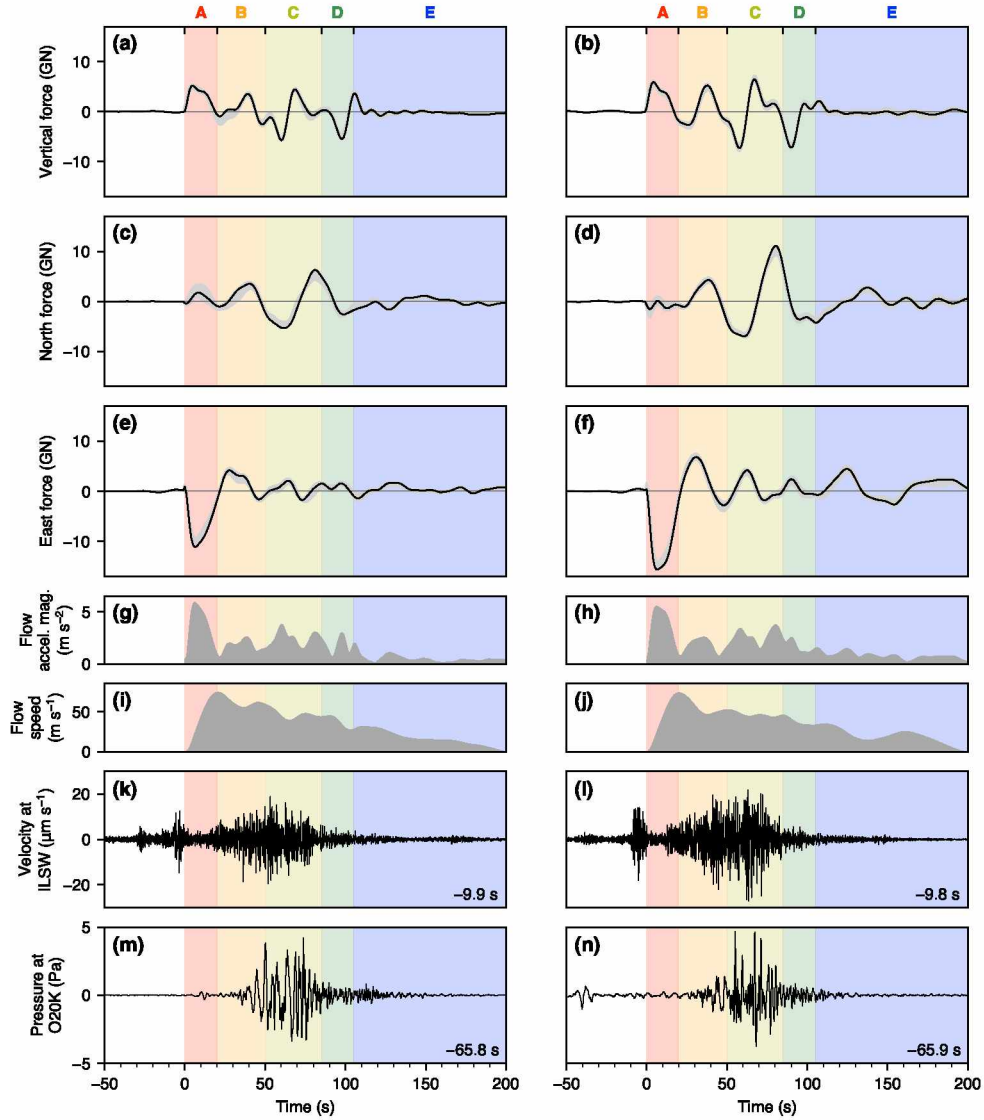


Figure 2.8 Force inversion results for the 2016 (left column) and 2019 (right column) events with seismoacoustic waveforms for reference. **(a–f)** Three-component (vertical, north, east) force-time function $\mathbf{f}(t)$. Gray patches show the jackknife-derived minimum and maximum forces for $\mathbf{f}(t)$. **(g, h)** Force-derived center of mass (COM) acceleration magnitude $\|\mathbf{a}(t)\|$. **(i, j)** Force-derived COM speed $\|\mathbf{v}(t)\|$. **(k, l)** Vertical component seismic waveforms from station ILSW shifted for travel time from the avalanche path midpoint using a Rayleigh group wavespeed at 1 Hz of 900 m s^{-1} . **(m, n)** Infrasound waveforms from station O20K shifted for travel time from the avalanche path midpoint using an acoustic wavespeed at 10°C of 337 m s^{-1} . The time shifts are indicated on the corresponding plots. Seismoacoustic waveforms are highpass filtered at 0.1 Hz. The time axes are relative to the inversion zero time. Vertical axis scales are equal for each row. Colored patches correspond to those in Figure 2.10 and letters A–E in §2.7.2.

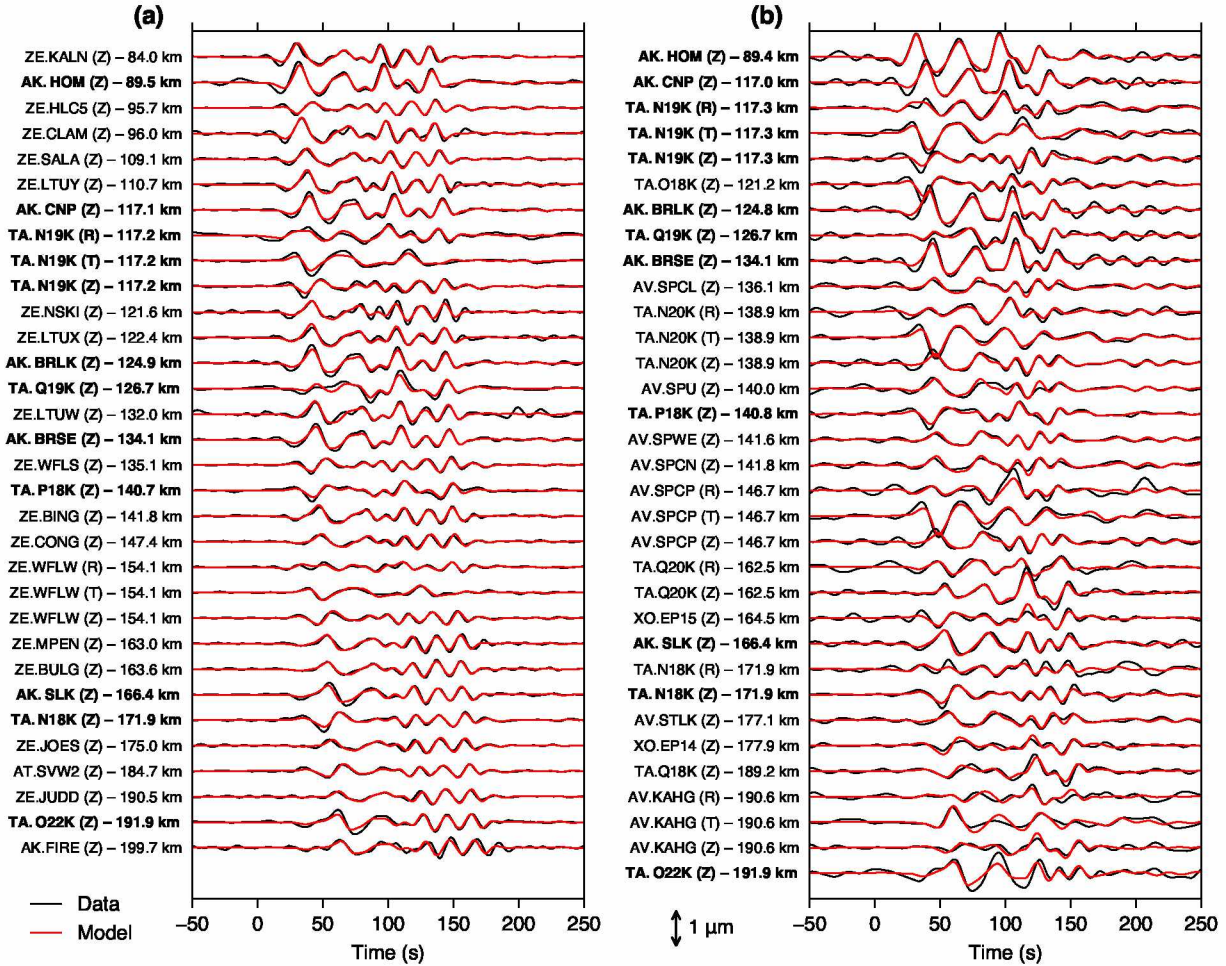


Figure 2.9 Waveform fits for the (a) 2016 and (b) 2019 force inversions. Observed data are plotted as black lines; modeled data are shown as red lines. Letters in parentheses indicate vertical (Z), radial (R), and transverse (T) components, and distance to the point force location is noted for each waveform. Boldface labels indicate components of stations used in both inversions (see Figure 2.1). Waveforms are *not* individually normalized, and the amplitude scale is identical between (a) and (b). The time axes are relative to the inversion zero time. (See §2.4 for description of network codes.)

The avalanches initiate with an upward- and westward-directed force, indicating acceleration of the avalanche down and to the east. This is followed by a complicated yet strikingly similar “coda” for the two events. There are prominent northward force peaks at ~ 40 and ~ 80 s. The second is sharper and larger amplitude than the first. There is also a broad southward force occurring after the first (broad) northward force peak with about the same amplitude,

at approximately 65 s. For both avalanches, the vertical component of $\mathbf{f}(t)$ contains two distinct “stair steps” where the force shifts from upwards, to near-zero, to downwards; these initiate at about 40 and 70 s. Both events conclude with an impulsive vertical downward force occurring at about 95 s in 2016 and 90 s in 2019. After this point, the vertical component is nearly zero, while the horizontal components show low-amplitude, long-period undulations which are more pronounced in 2019.

Seismically derived avalanche trajectories generally agree with true trajectories for both events. Map and vertical profile views of the force inversion trajectories for the two events are shown in Figure 2.10. As expected given the highly similar force-time functions, the shapes of the trajectories are very similar. The horizontal displacements indicate that the avalanche COMs moved almost due east before curving to the south, north, and south again. The vertical profiles in Figure 2.10c and d show minor undulations on an otherwise fairly constant slope, and are strictly decreasing as expected. The black lines are slices through the SfM DEM along the corresponding horizontal trajectory.

The vertical 2016 trajectory (Figure 2.10c) and horizontal 2019 trajectory (Figure 2.10b) show notable deviations from the DEM and imagery observations — we explore causes for this in §2.7.5. Jackknifed trajectories, shown as translucent colored lines in Figure 2.10, show about 1 km of spread on either side of the true location for the horizontal COM end point. For both events, the dominant eastward directionality is evident regardless of jackknife iteration. Note that the jackknifed trajectories primarily show uncertainties related to station coverage and data selection effects; other sources of trajectory uncertainties which also grow with time are not captured by the jackknife procedure and are discussed in §2.7.5.

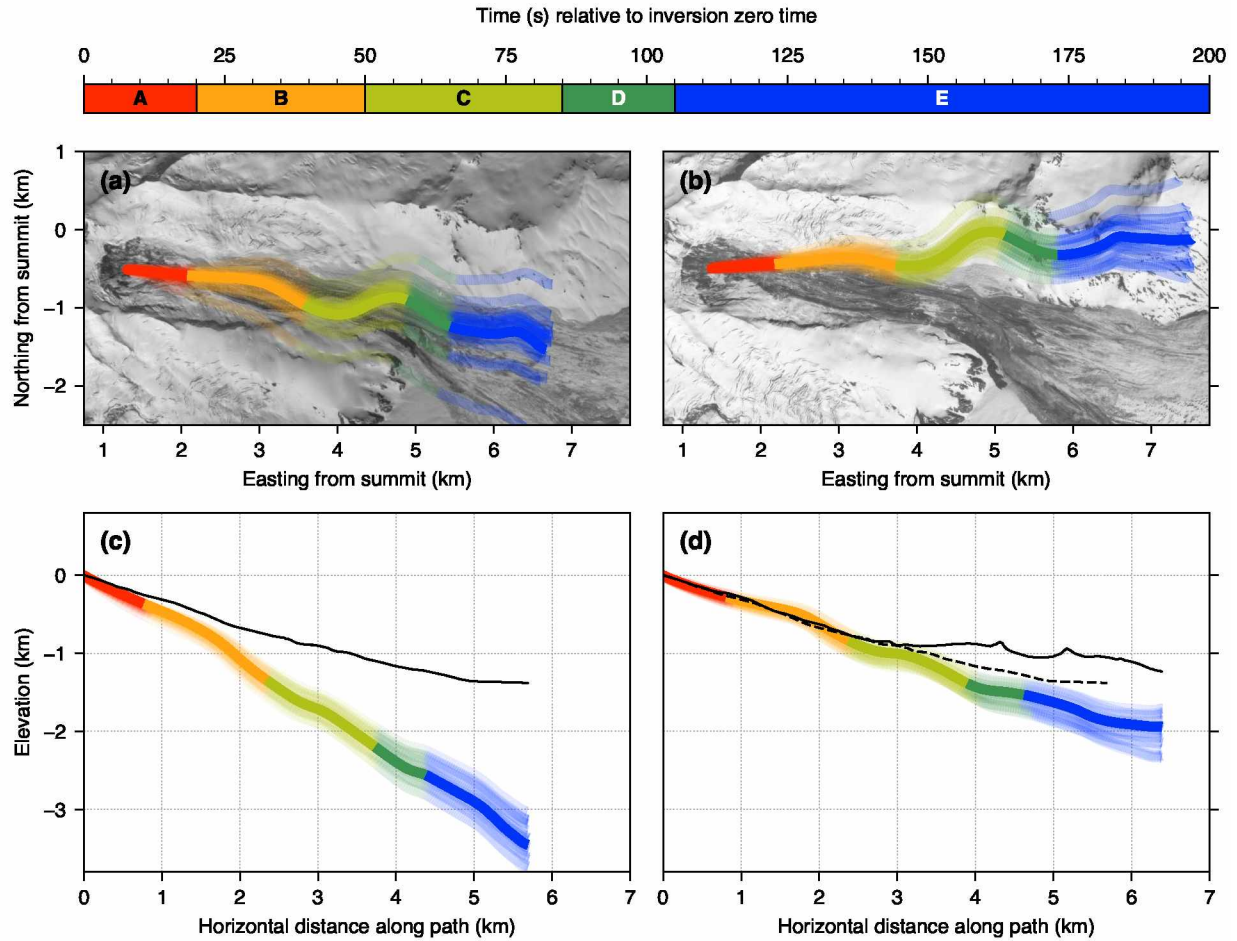


Figure 2.10 Map and profile views of trajectories integrated from the inversion force-time functions for the 2016 (a, c) and 2019 (b, d) events. Multiple translucent lines correspond to trajectories computed from the jackknife runs. Background images in (a) and (b) are the same as in Figure 2.2. Black lines in (c) and (d) are profiles through the structure from motion digital elevation model (SfM DEM) along the corresponding horizontal trajectory. Dashed line in (d) is the SfM DEM profile from (c). Colored segments correspond to those in Figure 2.8 and letters A–E in §2.7.2. Imagery © 2016 and 2019 Planet Labs, Inc.

Force-inversion derived COM runout distances and flow speeds have realistic magnitudes and are similar between the two events. Pinning the large northward force $\mathbf{f}(t)$ to the flow lobe on the orographically downslope left side of the flow path as described in §2.5.4 gives a horizontal along-path COM distance L_{COM} of 5.7 km with a corresponding mass of 2.1 billion kg for the 2016 event. For the 2019 event, $L_{COM} = 6.4$ km and the mass is 3.0 billion kg. Both trajectories indicate that most of the avalanche COM displacement occurred within the

first ~ 150 s of flow (Figure 2.10). Average and maximum speeds obtained by integration of $\mathbf{f}(t)$ are 33 and 75 m s^{-1} in 2016 and 34 and 74 m s^{-1} in 2019, respectively. Note that these results are all derived from the force inversion magnitudes. Our satellite imagery-derived calculations yield volumes of (13 ± 8) million m^3 in 2016 and (11 ± 7) million m^3 in 2019. The corresponding masses are (22 ± 14) billion kg in 2016 and (19 ± 13) billion kg in 2019.

2.7 Discussion

2.7.1 Acoustic Source Directionality

We lack sufficient infrasound station coverage to fully test an applicable acoustic source model, such as a single or distributed dipole, so we do not attempt an acoustic source inversion (e.g., Iezzi et al., 2019; Kim et al., 2012) here. Our infrasound analysis is therefore largely qualitative. By modeling infrasound propagation and site noise conditions, we sought to isolate source properties, such as size and directionality, from path effects. For example, Perttu et al. (2020) found that atmospheric propagation effects could not explain the infrasound radiation pattern observed for the 2018 Anak Krakatau flank collapse, and used this to infer that the collapse acted like a piston, pushing sound in a directed manner.

For the Iliamna avalanches, examination of acoustic propagation alone might lead one to believe that source directionality is present, given the consistent detections of stations to the east of Iliamna despite variable local propagation conditions between the two events. However, there are two complicating factors in our case. First, station noise analysis (Figure 2.6) shows that local stations to the west of Iliamna (and to the north and south as well in 2019) had high noise levels, indicating that preferential detection on stations to the east could simply be due to lower noise levels at those stations. Second, while rugged topography surrounds Iliamna, there is less topography blocking propagation to the east than to the west (Figure 2.1). Furthermore, the avalanches occurred on the east flank of Iliamna. Since infrasound propagation at local distances is strongly controlled by topography (Kim et al., 2015), propagation to the east from Iliamna may be topographically preferred. These com-

plicating factors preclude us from assessing source directionality or obtaining quantitative source estimates.

2.7.2 *Multi-Stage Failure and Flow*

Synthesis of the force-time function with high-frequency waveforms and force-derived COM acceleration magnitudes and speeds (Figure 2.8) as well as force-derived trajectories (Figure 2.10) suggests a consistent multi-stage failure and flow pattern for both avalanches. Our interpretation is as follows, with approximate times relative to the inversion zero time as well as color codes given in brackets:

- A.** Initial failure of the source region in ice or at the ice–bedrock interface and subsequent sliding at an average angle of $\sim 20\text{--}25^\circ$, manifested as a high-frequency (> 5 Hz) seismic transient and a substantial eastward acceleration. No detectable infrasound is generated by the initial failure (the small pulse visible at ~ 10 s in 2016 is not seen on any other stations or arrays and is therefore likely noise) [0–20 s; **red**].
- B.** The avalanche mass reaches its maximum speed and material becomes fragmented, changing the flow regime from coherent to granular and turbulent. This is manifested as a gradual increase in the high-frequency (> 5 Hz) seismic energy; infrasound energy begins to rise simultaneously as the flow bends to the south [20–50 s; **orange**].
- C.** The now-fragmented flow bends to the north and then to the south as both high-frequency seismic and infrasound signals reach their peak amplitudes. Flow speeds decrease but stay between $\sim 30\text{--}60$ m s $^{-1}$ [50–85 s; **light green**].
- D.** The flow encounters a change to a shallower slope angle ($< 10^\circ$) where a tributary glacier joins Red Glacier from the southwest (see Figure 2.2). This is manifested as an impulsive, relatively short-period (~ 30 s) downward force. The high-frequency seismic and infrasound signals taper off and flow speeds continue a slow decline [85–105 s; **dark green**].

E. After passing the kink in topography where slope angle decreases, the flow broadens and decelerates, forming the wide, flat debris lobe seen in Figure 2.2. The east component of $\mathbf{f}(t)$ is largely positive, indicating deceleration of the flow. The vertical component of $\mathbf{f}(t)$ is near-zero, and this portion of the flow is not seismically or acoustically energetic for frequencies > 0.1 Hz [105+ s; blue].

Our trajectories are compatible with numerical flow models for Red Glacier avalanches performed by Huggel et al. (2007) and Schneider et al. (2010), which both indicate that the avalanche COM tends to the orographic downslope right and then downslope left, in the latter case forming a superelevation-like flow lobe visible in Figure 2.2. We do not consider the possibility that the observed deposit was formed by two separate flows, as suggested by Huggel et al. (2007) for the 1980 and 2003 Red Glacier avalanches, because we do not see evidence for two separate flows in the seismoacoustic signals or in satellite imagery of the deposits (Figure 2.2), and our modeling assuming a single flow is compatible with previous modeling and observations. This suggests that only one flow took place, at least in 2016 and 2019.

2.7.3 Mass Estimation

One complication of extracting quantitative information from the force inversion results concerns the method of regularization. Since we impose penalties on the size, slope, and roughness of $\mathbf{f}(t)$ via the a_i coefficients, the resultant force amplitudes are likely artificially depressed compared to the true values, as mentioned in §2.5.4. This is evidenced by the much smaller magnitude of the masses from the force inversion trajectories versus our satellite-imagery-based estimates (2.1 and 3.0 billion kg versus 22 and 19 billion kg for the 2016 and 2019 events, respectively). Even the lower bounds on our imagery-based mass estimates are still far larger than their inversion-derived equivalents, suggesting that the force amplitudes are indeed being suppressed by the regularization scheme (see Appendix 2.10). Additionally, we are inverting a band-limited signal — energy present at very long periods (> 80 s) is

not reflected in $\mathbf{f}(t)$, which also artificially depresses $\mathbf{f}(t)$. Due to these biases, we do not apply the scaling relationship of Ekström and Stark (2013) to these results. We note that in general the masses of these events are not well constrained due to poor constraints on deposit thickness and the relative contributions of entrainment and deposition to the total failure mass. Better ground observations of avalanche deposit properties would help constrain the effect of regularization, and we encourage such studies in the future. We do note that the phase and *relative* amplitude of the force-time function between the two events (Figure 2.8a–f) are not affected by the regularization.

2.7.4 Flow Dynamics

Average flow speeds for mass movements can be estimated from the duration of the high-frequency seismic envelope if the horizontal runout length L is known (Caplan-Auerbach et al., 2004). However, it is often difficult to estimate the duration of the flow from the seismic envelope, since the noise floor can bury the earliest and latest parts of the emergent signal (Huggel et al., 2007). Caplan-Auerbach and Huggel (2007) estimated average flow speeds of about 20–50 m s⁻¹ for Red Glacier avalanches using this method. A more complete assessment of flow speeds can be obtained from numerical modeling or by examination of the speed time series $\|\mathbf{v}(t)\|$ obtained from the force inversion, as these provide both average and maximum values. Schneider et al. (2010) found an average flow speed of about 50 m s⁻¹ and peak flow speeds between 70–100 m s⁻¹ for a numerically modeled 2003 Red Glacier avalanche. Our values derived from $\|\mathbf{v}(t)\|$ (average speeds of 33 and 34 m s⁻¹ and maximum speeds of 75 and 74 m s⁻¹ in 2016 and 2019, respectively) are compatible with these results as well as those of Caplan-Auerbach and Huggel (2007), though we note that our values describe COM dynamics, while those of Caplan-Auerbach and Huggel (2007) are calculated using L and therefore apply to the flow front. Our results are also broadly compatible with other studies of similar large avalanches, such as the July 2007 Mount Steele rock–ice avalanche

(35–65 m s⁻¹ average speed; Lipovsky et al., 2008) and the June 2016 Lamplugh Glacier rock avalanche (~55 m s⁻¹ maximum speed; Dufresne et al., 2019).

Inversion-derived COM acceleration magnitudes $\|\mathbf{a}(t)\|$ and flow speeds $\|\mathbf{v}(t)\|$ are plotted in Figure 2.8g–j. The peak infrasound amplitude does not correlate with peak acceleration magnitude nor peak speed, instead occurring about 50 s after the latter. This notable latency between peak speed and peak acoustic energy might be explained by a model similar to Marchetti et al. (2019), where infrasound is produced by waves at the free surface of the flow. Such waves would take time to develop since the initially blocky mass needs to be sufficiently fragmented and turbulent, which requires high flow speeds. The infrasound and seismic waveforms (Figure 2.8k–n) do exhibit similar shapes and reach their peak values at approximately the same time (after travel time removal). This alignment of high-frequency seismic and infrasound signals has previously been observed for debris flows (Marchetti et al., 2019; Schimmel et al., 2018) and suggests that after some initial breakup period, Iliamna ice–rock avalanches may exhibit similar flow dynamics to debris flows, at least seismoacoustically.

Another possibility is that flow interaction with a particular topographic feature along the flow path is generating infrasound, and that the observed peak amplitude timing corresponds to the travel time for the flow to reach this feature. Figure 2.8m and n indicates that peak infrasound occurs anywhere from 50–85 s into the flow. Because the prominent northward force linked to the flow lobe on the orographically downslope left side of the flow occurs at about 80 s, flow turbulence at this point could be responsible for the peak in infrasound energy. Moore et al. (2017) observed a ground-coupled airwave associated with the second of two very large rock avalanches at Bingham Canyon Mine (Utah, USA). They inferred from the timing of the phase that the airwave was likely coupled into the ground when the rock avalanche was beginning to impact the pit bottom, ~50 s after the start of the event. However, this explanation makes less sense in the context of the Red Glacier avalanches because the topography of Red Glacier is far smoother (e.g., compare the black line in Figure 2.10c to Moore et al. (2017), Figure 5).

2.7.5 *Inversion Stability and Trajectory Uncertainties*

The low variance of the jackknife iterations (Figure 2.8a–f) indicates that the inversion result is largely unaffected by changes to the input data. We note two prominent issues with the calculated trajectories, however:

1. The 2019 horizontal trajectory is rotated approximately 15° counterclockwise relative to the 2016 trajectory, though both have the same shape.
2. The 2016 vertical trajectory is too steep relative to the bed topography (black line in Figure 2.10a).

There are several potential causes for these discrepancies. One possibility is that our model loses validity over the course of the event. Since the premise of the force inversion assumes a single point force, as the avalanche moves downslope and transitions from a sliding block to a more distributed, fragmented flow, our source model becomes less applicable (see Coe et al., 2016). However, the horizontal trajectories provide a reasonable quantitative estimate for the entire flow path, not just the initial period of supposed higher model validity. Ultimately, without video footage of the events, improved mass estimates, or sophisticated flow modeling, understanding where the model may begin to break down is challenging.

Another factor is noise within the passband of our inversion. We note that while the SNR for the longer-period portion of the inversion passband was generally greater in 2019 than in 2016, the SNR for shorter periods (15–25 s) was lower in 2019 than in 2016 (Figure 2.5). This greater short-period noise in 2019 is visible when comparing the waveforms in 2016 (Figure 2.9a) to those in 2019 (Figure 2.9b). We were unable to avoid this noise without increasing the minimum period of the inversion and thereby sacrificing short-period details in $\mathbf{f}(t)$, which are consistent between the two events and thus not spurious. As this short-period noise is more prominent in 2019 than 2016, it could contribute to the misaligned horizontal trajectory for the 2019 event. We note that the VR for the 2019 inversion is about 10% lower than the VR for the 2016 inversion; this is readily seen in Figure 2.9.

Finally, our inversion may be biased by uneven azimuthal station coverage or an uneven distribution of seismometer components. For most stations, horizontal components tended to be noisier than vertical components. Consequently, most of our input waveform data for the inversion is vertical component (see component labels in Figure 2.9). Mathematically, Equation 2.1 shows that given sufficient azimuthal coverage, $\mathbf{f}(t)$ should be recoverable from the vertical displacement time series $u_z(t)$ alone. However, our largely vertical-component input data could be biasing our $f_z(t)$ amplitudes too high. This in turn would produce overly steep vertical trajectories. We tested the inversion’s sensitivity to azimuthal station coverage and found that the 2019 trajectory showed negligible change unless significant deviations (e.g., only retaining stations to the south of Iliamna) were undertaken.

All of the preceding issues are exacerbated when we doubly integrate $\mathbf{f}(t)$ to obtain displacement. Therefore, a relatively small southward bias in $\mathbf{f}(t)$ could nudge the entire trajectory northward in the manner seen for the 2019 event. This also applies to the overly steep vertical trajectory in 2016 — if at any point in $\mathbf{f}(t)$ the vertical component is overestimated, the vertical trajectory will be affected from that point onwards. In spite of these issues, the consistent shape of the trajectories and the strikingly similar phase and relative amplitude of the force-time functions give us confidence in our modeling.

2.7.6 Comparing Events

A key benefit of modeling two highly similar avalanches is the opportunity to compare the inversion results, determine which features are consistent between the two events, and evaluate the inversion technique. Examination of $\mathbf{f}(t)$ for the 2016 event alone might lead one to conclude that the shorter-period details are just spurious byproducts of noise or path effects. However, the 2019 avalanche has flow and deposit characteristics that are remarkably similar to those of the 2016 event, and we observe similar details in $\mathbf{f}(t)$ in spite of varying path effects due to different station configurations in 2016 and 2019. This provides more confidence in the inversion method used here.

One notable difference between the force-time functions obtained for the two avalanches is the increased amplitude for the 2019 event. This increase is consistent across all three force components, yet it is unlikely to be an inversion artifact since both inversions have the same regularization parameters. The high-frequency seismic signals (Figure 2.8k and l) also indicate larger amplitudes for the 2019 event. Since the observed deposits have similar sizes (see Figure 2.2), this suggests that a larger amount of mass was moved in 2019 than in 2016 but with little change in runout length. The mass discrepancy could be caused by varying initial failure thicknesses (i.e., a thicker crown in 2019) or an increased portion of rock involved in the 2019 event versus the 2016 event. Unfortunately, we do not possess the field-based observations and measurements necessary to test these hypotheses.

2.7.7 Feasibility for Rapid Hazard Response

The detailed information on avalanche dynamics retrievable from the rapidly-recorded seismic signals for these events raises the question of the suitability of this method for near-real-time applications. Besides the seismic signals themselves, only two independent pieces of information are required to obtain 3D trajectories: The event location (for locating the point force) and the failure mass (for converting force to acceleration). In this study, we used high-resolution satellite imagery to estimate the former.

In the absence of any independent data, the following could be performed: The event location could be estimated using traditional earthquake or mass movement-specific location methods (see K. E. Allstadt et al., 2018, and references therein), and the failure mass could be roughly estimated from the scaling laws of Ekström and Stark (2013). A location could also be determined from infrasound signals using backprojection (see e.g. Sanderson et al., 2020). Note that due to the long wavelengths of the signals used, a precise location is not critical for the inversion process. The resulting seismically derived trajectory would be a rough approximation due to uncertainties in mass estimation and/or location. However, the *directionality* and relative size of the mass movement would be preserved, and this

information could be harnessed to remotely determine the likely path and scale of a mass movement.

Unfortunately, automatic locations are not available for the two Iliamna events or other events of comparable size. However, we note that the very large June 2016 Lamplugh Glacier, Alaska rock avalanche (see Bessette-Kirton et al., 2018; Dufresne et al., 2019) has a cataloged location and origin time. In general, at this time an automatic inversion method would likely be successful only for very large mass movements with high SNR seismic and acoustic waveforms. We note that our methods are primarily aimed at providing information complementary to other techniques; they do not currently constitute a stand-alone or automated technique. Still, in remote settings where event information from other sources may be delayed or unavailable — such as Alaska — this approach could provide key estimates of basic flow properties in near-real-time.

2.8 Conclusions

Surficial mass movements transfer energy into the solid Earth and the atmosphere, producing seismoacoustic signals that yield complementary information about event dynamics. In this study, we analyze an exceptional seismoacoustic dataset from two large, highly similar ice–rock avalanches to reconstruct the dynamics of the events. The similarity of these avalanches provides an excellent opportunity to test the robustness of our modeling methods. Our force-time functions are derived from the inversion of long-period (15–80 s) seismic signals recorded on stations > 80 km from the avalanches. They indicate that over the course of about 150 s, the avalanche COM slid to the east, was subsequently deflected slightly to the south and then to the north, and then broadly decelerated. Our results provide constraints on time-varying avalanche acceleration, velocity, and directionality. This is important for hazard mitigation as well as general understanding of seismic signals from mass movements, though better estimates of mass and flow properties from field studies (e.g., Dufresne et al.,

2019) and numerical modeling (e.g., Moretti et al., 2012) are needed to fully exploit this method’s potential.

While it was possible to model the avalanche seismic source, we lacked sufficient infrasound data to quantitatively characterize the acoustic source. After accounting for propagation effects and station noise, we cannot assess whether the Iliamna avalanches exhibit acoustic source directionality. Still, the acoustic data are qualitatively consistent with our force-derived reconstructions. It appears that infrasound from these avalanches is produced after the mass movement regime transitions from cohesive block-type failure to granular and turbulent flow, but controlled experiments and denser acoustic instrumentation are needed to fully test this hypothesis.

Iliamna Volcano is an excellent site for the seismoacoustic and geomorphological study of these impressive avalanches due to their relatively frequent occurrence at the volcano. Future work at Iliamna — as well as at other sites of repetitive surficial mass movements — should synthesize advanced numerical modeling techniques with detailed observations including video footage and repeat high-resolution DEM acquisitions. These efforts, combined with more complete acoustic station coverage — perhaps with arrays as well as single sensors — could result in a substantial increase in our understanding of the behavior of large debris avalanches and other mass movements. This insight may then be applicable for mitigation of, and response to, the significant hazards posed by these dramatic surface processes.

2.9 Code and Data Availability

We used the open-source Python package `lsforce` (code.usgs.gov/ghsc/lhp/lsforce; K. Allstadt & Toney, 2020) to perform the force inversions. All of the seismic and infrasound data used in this study are available from the Incorporated Research Institutions for Seismology Data Management Center (IRIS DMC). The CPS model file we used to compute GFs for the inversions is available at eas.slu.edu/eqc/eqc_cps/TUTORIAL/SPHERICITY/AK135/tak135sph.mod.

2.10 Appendix A: Inversion Formulation and Constraints

Consider the convolutions given by Equations 2.1–2.3. In numerical contexts, it is more convenient to formulate these convolutions as matrix multiplications. We therefore transform the Green’s functions (GFs) into convolution matrices $\mathbf{\Lambda}$ by reversing the GFs in time and staggering them as in K. E. Allstadt (2013), where the time dependence of the GF is now implicitly stored in the matrix. (For example, the multiplication $\mathbf{\Lambda}_{\mathbf{ZV}}\mathbf{f}_{\mathbf{Z}}$ corresponds to the convolution $f_{\mathbf{Z}}(t)*g_{\mathbf{ZV}}(t)$; see K. E. Allstadt (2013), Equation A5.) Making this modification, we can combine Equations 2.1–2.3 (dropping the explicit time dependence for brevity) into

$$\mathbf{u}^k = \mathbf{\Gamma}^k \mathbf{f}, \quad (2.5)$$

where now the superscript k denotes the station and $\mathbf{\Gamma}^k$ is a matrix of GF convolution matrices:

$$\mathbf{\Gamma}^k = \begin{bmatrix} \mathbf{\Lambda}_{\mathbf{ZV}}^k & \mathbf{\Lambda}_{\mathbf{ZH}}^k \cos \phi^k & \mathbf{\Lambda}_{\mathbf{ZH}}^k \sin \phi^k \\ \mathbf{\Lambda}_{\mathbf{RV}}^k & \mathbf{\Lambda}_{\mathbf{RH}}^k \cos \phi^k & \mathbf{\Lambda}_{\mathbf{RH}}^k \sin \phi^k \\ \mathbf{0} & \mathbf{\Lambda}_{\mathbf{TH}}^k \sin \phi^k & -\mathbf{\Lambda}_{\mathbf{TH}}^k \cos \phi^k \end{bmatrix}. \quad (2.6)$$

We can now write the linear forward model for N stations as

$$\mathbf{d} = \mathbf{G} \mathbf{f}, \quad (2.7)$$

with $\mathbf{d} = [\mathbf{u}^1, \mathbf{u}^2, \dots, \mathbf{u}^k, \dots, \mathbf{u}^N]^\top$ and $\mathbf{G} = [\mathbf{\Gamma}^1, \mathbf{\Gamma}^2, \dots, \mathbf{\Gamma}^k, \dots, \mathbf{\Gamma}^N]^\top$. The superscript \top denotes the transpose; \mathbf{d} is a 1D column vector consisting of the data predicted for each component of each station \mathbf{u}^k concatenated end-to-end. This is an ill-conditioned problem, so regularization is required to reduce the condition number of \mathbf{G} . We invert for \mathbf{f} using a higher-order Tikhonov-regularized least squares formulation (e.g., Aster et al., 2013). The solution is

$$\mathbf{f} = [\mathbf{G}^\top \mathbf{G} + \alpha^2 (a_0 \mathbf{I} + a_1 \mathbf{L}_1^\top \mathbf{L}_1 + a_2 \mathbf{L}_2^\top \mathbf{L}_2)]^{-1} \mathbf{G}^\top \mathbf{d}, \quad (2.8)$$

where \mathbf{I} is the identity matrix and \mathbf{L}_1 and \mathbf{L}_2 are first- and second-order roughening matrices which approximate the first and second derivatives, respectively. The coefficients a_0 , a_1 , and a_2 control the degree of importance given to “small,” “flat,” and “smooth” models, respectively. They must sum to one:

$$\sum_{i=0}^2 a_i = 1. \quad (2.9)$$

The regularization parameter α is chosen to balance the constraints on the model specified by the a_i coefficients while still fitting the data well. We use the L-curve criterion (Hansen, 1992) to find the optimal value for α . For both inversions, we found the optimal values for these parameters were $\alpha = 5.3 \times 10^{-17}$ and $a_i = [0.4, 0, 0.6]$. This selection of a_i parameters prioritizes a model that is both small in magnitude (more centered on zero) and smooth. The inclusion of the higher-order regularization matrices \mathbf{L}_1 and \mathbf{L}_2 in Equation 2.8 separates this method from the method used in K. E. Allstadt (2013) and Coe et al. (2016), which only included zeroth-order Tikhonov regularization.

To characterize the fit of the model to the data, we compute the variance reduction (VR), which is defined as

$$\text{VR} = \left(1 - \frac{\|\mathbf{d} - \mathbf{d}_{\text{obs}}\|^2}{\|\mathbf{d}_{\text{obs}}\|^2} \right) \times 100\%, \quad (2.10)$$

where \mathbf{d}_{obs} are the observed data and \mathbf{d} are the synthetic data predicted by the forward model (Equation 2.7).

In addition to regularization, we constrain all of the components of \mathbf{f} to sum to zero to conserve the total momentum of the Earth (see K. E. Allstadt, 2013, Appendix A). We also enforce all components of \mathbf{f} be zero prior to a specified “zero time.” We choose the zero time to correspond to the point where the vertical component $f_z(t)$ is non-zero and rising, signaling the initial downward acceleration of the avalanche. The zero time for the 22 May 2016 event is 07:57:57 and the zero time for the 21 June 2019 event is 00:03:13. The selection of the zero time was unambiguous for both events.

To assess the stability of the inversion, we use a variation on the jackknife technique (e.g., Coe et al., 2016; Moretti et al., 2015). We run 20 iterations of the inversion, each time randomly discarding 30% of the waveforms.

2.11 Acknowledgements

We used the Python seismological framework ObsPy (www.obspy.org; Beyreuther et al., 2010) extensively in this study. We also used the spectral estimation Python wrapper mtspec ([krischer.github.io/mtspec](https://github.com/krischer/mtspec); Krischer, 2016) to generate the PSDs in Figure 2.5. Figures were created using Matplotlib (matplotlib.org; Hunter, 2007), the Generic Mapping Tools (GMT; www.generic-mapping-tools.org; Wessel et al., 2019), and PyGMT (www.pygmt.org; Uieda et al., 2022), the Python interface for GMT.

We thank Hannah Dietterich and Tim Orr for their contributions to the Iliamna SfM project. Jacqueline Caplan-Auerbach and Chris Waythomas helped us understand the recent history and typical character of Iliamna avalanches. Taryn Lopez provided us with information about zones of recent fumarolic activity on Iliamna. We thank Carl Tape for early access to embargoed SALMON data. The quality of this manuscript was significantly improved by the helpful comments of Janet Slate, Mark Reid, Velio Coviello, and one anonymous reviewer.

R. Matoza was supported by NSF grants EAR-1614855 and EAR-1847736. The authors also acknowledge support from NSF grant EAR-1614323 and from AVO through the U.S. Geological Survey Volcano Hazards Program.

Ch'naqał'in (Iliamna Volcano) is located on the ancestral lands of the Dena'ina people of south-central Alaska.

2.12 References

Allstadt, K., McVey, B., & Malone, S. (2017). *Seismogenic landslides, debris flows, and outburst floods in the western United States and Canada from 1977 to 2017: U.S. Geological Survey data release*. <https://doi.org/10.5066/F7251H3W>

- Allstadt, K., & Toney, L. (2020). *lsforce*. U.S. Geological Survey. <https://doi.org/10.5066/P9CR20KW>
- Allstadt, K. E. (2013). Extracting source characteristics and dynamics of the August 2010 Mount Meager landslide from broadband seismograms. *Journal of Geophysical Research: Earth Surface*, *118*(3), 1472–1490. <https://doi.org/10.1002/jgrf.20110>
- Allstadt, K. E., Matoza, R. S., Lockhart, A. B., Moran, S. C., Caplan-Auerbach, J., Haney, M. M., Thelen, W. A., & Malone, S. D. (2018). Seismic and acoustic signatures of surficial mass movements at volcanoes. *Journal of Volcanology and Geothermal Research*, *364*, 76–106. <https://doi.org/10.1016/j.jvolgeores.2018.09.007>
- Aster, R., Borchers, B., & Thurber, C. (2013). *Parameter Estimation and Inverse Problems*. Elsevier. <https://doi.org/10.1016/C2009-0-61134-X>
- Bessette-Kirton, E. K., Coe, J. A., & Zhou, W. (2018). Using stereo satellite imagery to account for ablation, entrainment, and compaction in volume calculations for rock avalanches on glaciers: Application to the 2016 Lamplugh rock avalanche in Glacier Bay National Park, Alaska. *Journal of Geophysical Research: Earth Surface*, *123*(4), 622–641. <https://doi.org/10.1002/2017JF004512>
- Beyreuther, M., Barsch, R., Krischer, L., Megies, T., Behr, Y., & Wassermann, J. (2010). ObsPy: A Python toolbox for seismology. *Seismological Research Letters*, *81*(3), 530–533. <https://doi.org/10.1785/gssrl.81.3.530>
- Bishop, J. W., Fee, D., & Szuberla, C. A. L. (2020). Improved infrasound array processing with robust estimators. *Geophysical Journal International*, *221*(3), 2058–2074. <https://doi.org/10.1093/gji/ggaa110>
- Caplan-Auerbach, J., & Huggel, C. (2007). Precursory seismicity associated with frequent, large ice avalanches on Iliamna volcano, Alaska, USA. *Journal of Glaciology*, *53*(180), 128–140. <https://doi.org/10.3189/172756507781833866>
- Caplan-Auerbach, J., Prejean, S. G., & Power, J. a. (2004). Seismic recordings of ice and debris avalanches of Iliamna Volcano, Alaska. *Acta Vulcanologica*, *16*(1-2), 9–20.
- Coe, J. A., Baum, R. L., Allstadt, K. E., Kochevar, B. F., Schmitt, R. G., Morgan, M. L., White, J. L., Stratton, B. T., Hayashi, T. A., & Kean, J. W. (2016). Rock-avalanche dynamics revealed by large-scale field mapping and seismic signals at a highly mobile avalanche in the West Salt Creek valley, western Colorado. *Geosphere*, *12*(2), 607–631. <https://doi.org/10.1130/GES01265.1>
- Davies, T., McSaveney, M., & Kelfoun, K. (2010). Runout of the Socompa volcanic debris avalanche, Chile: a mechanical explanation for low basal shear resistance. *Bulletin of Volcanology*, *72*(8), 933–944. <https://doi.org/10.1007/s00445-010-0372-9>

- Delle Donne, D., Ripepe, M., De Angelis, S., Cole, P. D., Lacanna, G., Poggi, P., & Stewart, R. (2014). Chapter 9 Thermal, acoustic and seismic signals from pyroclastic density currents and Vulcanian explosions at Soufrière Hills Volcano, Montserrat. *Geological Society, London, Memoirs*, *39*(1), 169–178. <https://doi.org/10.1144/m39.9>
- Drob, D. P., Emmert, J. T., Meriwether, J. W., Makela, J. J., Doornbos, E., Conde, M., Hernandez, G., Noto, J., Zawdie, K. A., McDonald, S. E., Huba, J. D., & Klenzing, J. H. (2015). An update to the Horizontal Wind Model (HWM): The quiet time thermosphere. *Earth and Space Science*, *2*(7), 301–319. <https://doi.org/10.1002/2014EA000089>
- Drob, D. P., Picone, J. M., & Garcés, M. (2003). Global morphology of infrasound propagation. *Journal of Geophysical Research: Atmospheres*, *108*(D21), 1–12. <https://doi.org/10.1029/2002JD003307>
- Dufresne, A., Wolken, G. J., Hibert, C., Bessette-Kirton, E. K., Coe, J. A., Geertsema, M., & Ekström, G. (2019). The 2016 Lamplugh rock avalanche, Alaska: deposit structures and emplacement dynamics. *Landslides*, *16*(12), 2301–2319. <https://doi.org/10.1007/s10346-019-01225-4>
- Ekström, G., & Stark, C. P. (2013). Simple scaling of catastrophic landslide dynamics. *Science*, *339*(6126), 1416–1419. <https://doi.org/10.1126/science.1232887>
- Fee, D., & Matoza, R. S. (2013). An overview of volcano infrasound: From hawaiian to plinian, local to global. *Journal of Volcanology and Geothermal Research*, *249*(3), 123–139. <https://doi.org/10.1016/j.jvolgeores.2012.09.002>
- Fee, D., Waxler, R., Assink, J., Gitterman, Y., Given, J., Coyne, J., Mialle, P., Garces, M., Drob, D., Kleinert, D., Hofstetter, R., & Grenard, P. (2013). Overview of the 2009 and 2011 Sayarim infrasound calibration experiments. *Journal of Geophysical Research: Atmospheres*, *118*(12), 6122–6143. <https://doi.org/10.1002/jgrd.50398>
- Gualtieri, L., & Ekström, G. (2018). Broad-band seismic analysis and modeling of the 2015 Taan Fjord, Alaska landslide using Instaseis. *Geophysical Journal International*, *213*(3), 1912–1923. <https://doi.org/10.1093/gji/ggy086>
- Gualtieri, L., Stutzmann, E., Capdeville, Y., Farra, V., Mangeney, A., & Morelli, A. (2015). On the shaping factors of the secondary microseismic wavefield. *Journal of Geophysical Research: Solid Earth*, *120*(9), 6241–6262. <https://doi.org/10.1002/2015JB012157>
- Haney, M. M., Matoza, R. S., Fee, D., & Aldridge, D. F. (2018). Seismic equivalents of volcanic jet scaling laws and multipoles in acoustics. *Geophysical Journal International*, *213*(1), 623–636. <https://doi.org/10.1093/gji/ggx554>

- Hansen, P. C. (1992). Analysis of discrete ill-posed problems by means of the L-curve. *SIAM Review*, *34*(4), 561–580. <https://doi.org/10.1137/1034115>
- Havens, S., Marshall, H.-P., Johnson, J. B., & Nicholson, B. (2014). Calculating the velocity of a fast-moving snow avalanche using an infrasound array. *Geophysical Research Letters*, *41*(17), 6191–6198. <https://doi.org/10.1002/2014GL061254>
- Herrick, J. A., Neal, C. A., Cameron, C. E., Dixon, J. P., & McGimsey, R. G. (2014). *2012 volcanic activity in Alaska—Summary of events and response of the Alaska Volcano Observatory, U.S. Geological Survey Scientific Investigations Report 2014-5160, 81 p.* <https://doi.org/10.3133/sir20145160>
- Herrmann, R. B. (2013). Computer Programs in Seismology: An evolving tool for instruction and research. *Seismological Research Letters*, *84*(6), 1081–1088. <https://doi.org/10.1785/0220110096>
- Hibert, C., Ekström, G., & Stark, C. P. (2017). The relationship between bulk-mass momentum and short-period seismic radiation in catastrophic landslides. *Journal of Geophysical Research: Earth Surface*, *122*(5), 1201–1215. <https://doi.org/10.1002/2016JF004027>
- Huggel, C., Caplan-Auerbach, J., Waythomas, C. F., & Wessels, R. L. (2007). Monitoring and modeling ice-rock avalanches from ice-capped volcanoes: A case study of frequent large avalanches on Iliamna Volcano, Alaska. *Journal of Volcanology and Geothermal Research*, *168*(1-4), 114–136. <https://doi.org/10.1016/j.jvolgeores.2007.08.009>
- Huggel, C., Haeberli, W., Kääh, A., Bieri, D., & Richardson, S. (2004). An assessment procedure for glacial hazards in the Swiss Alps. *Canadian Geotechnical Journal*, *41*(6), 1068–1083. <https://doi.org/10.1139/t04-053>
- Hungr, O., Leroueil, S., & Picarelli, L. (2014). The Varnes classification of landslide types, an update. *Landslides*, *11*(2), 167–194. <https://doi.org/10.1007/s10346-013-0436-y>
- Hunter, J. D. (2007). Matplotlib: A 2D graphics environment. *Computing in Science & Engineering*, *9*(3), 90–95. <https://doi.org/10.1109/MCSE.2007.55>
- Iezzi, A. M., Fee, D., Kim, K., Jolly, A. D., & Matoza, R. S. (2019). Three-dimensional acoustic multipole waveform inversion at Yasur Volcano, Vanuatu. *Journal of Geophysical Research: Solid Earth*, *124*(8), 8679–8703. <https://doi.org/10.1029/2018JB017073>
- Johnson, J. B., & Palma, J. L. (2015). Lahar infrasound associated with Volcán Villarrica’s 3 March 2015 eruption. *Geophysical Research Letters*, *42*(15), 6324–6331. <https://doi.org/10.1002/2015GL065024>

- Johnson, J. B., & Ronan, T. J. (2015). Infrasound from volcanic rock-falls. *Journal of Geophysical Research: Solid Earth*, *120*(12), 8223–8239. <https://doi.org/10.1002/2015JB012436>
- Kawakatsu, H. (1989). Centroid single force inversion of seismic waves generated by landslides. *Journal of Geophysical Research*, *94*(B9), 12363–12374. <https://doi.org/10.1029/JB094iB09p12363>
- Kennett, B. L. N., Engdahl, E. R., & Buland, R. (1995). Constraints on seismic velocities in the Earth from traveltimes. *Geophysical Journal International*, *122*(1), 108–124. <https://doi.org/10.1111/j.1365-246X.1995.tb03540.x>
- Kim, K., Fee, D., Yokoo, A., & Lees, J. M. (2015). Acoustic source inversion to estimate volume flux from volcanic explosions. *Geophysical Research Letters*, *42*(13), 5243–5249. <https://doi.org/10.1002/2015GL064466>
- Kim, K., Lees, J. M., & Ruiz, M. (2012). Acoustic multipole source model for volcanic explosions and inversion for source parameters. *Geophysical Journal International*, *191*(3), 1192–1204. <https://doi.org/10.1111/j.1365-246X.2012.05696.x>
- Kogelnig, A., Hübl, J., Suriñach, E., Vilajosana, I., & McArdell, B. W. (2014). Infrasound produced by debris flow: Propagation and frequency content evolution. *Natural Hazards*, *70*(3), 1713–1733. <https://doi.org/10.1007/s11069-011-9741-8>
- Krischer, L. (2016). *mtspec Python wrappers 0.3.2*. Zenodo. <https://doi.org/10.5281/zenodo.321789>
- Lipovsky, P. S., Evans, S. G., Clague, J. J., Hopkinson, C., Couture, R., Bobrowsky, P., Ekström, G., Demuth, M. N., Delaney, K. B., Roberts, N. J., Clarke, G., & Schaeffer, A. (2008). The July 2007 rock and ice avalanches at Mount Steele, St. Elias Mountains, Yukon, Canada. *Landslides*, *5*(4), 445–455. <https://doi.org/10.1007/s10346-008-0133-4>
- Marchetti, E., Ripepe, M., Olivieri, G., & Kogelnig, A. (2015). Infrasound array criteria for automatic detection and front velocity estimation of snow avalanches: towards a real-time early-warning system. *Natural Hazards and Earth System Sciences*, *15*(11), 2545–2555. <https://doi.org/10.5194/nhess-15-2545-2015>
- Marchetti, E., van Herwijnen, A., Christen, M., Silengo, M. C., & Barfucci, G. (2020). Seismo-acoustic energy partitioning of a powder snow avalanche. *Earth Surface Dynamics*, *8*(2), 399–411. <https://doi.org/10.5194/esurf-8-399-2020>

- Marchetti, E., Walter, F., Barfucci, G., Genco, R., Wenner, M., Ripepe, M., McArdell, B., & Price, C. (2019). Infrasonic array analysis of debris flow activity and implication for early warning. *Journal of Geophysical Research: Earth Surface*, *124*(2), 567–587. <https://doi.org/10.1029/2018JF004785>
- Matoza, R., Fee, D., Green, D., & Mialle, P. (2019). Volcano Infrasonic and the International Monitoring System. In A. Le Pichon, E. Blanc, & A. Hauchecorne (Eds.), *Infrasonic monitoring for atmospheric studies* (pp. 1023–1077). Cham: Springer International Publishing. https://doi.org/10.1007/978-3-319-75140-5_33
- Montagner, J.-P., & Kennett, B. L. N. (1996). How to reconcile body-wave and normal-mode reference earth models. *Geophysical Journal International*, *125*(1), 229–248. <https://doi.org/10.1111/j.1365-246X.1996.tb06548.x>
- Moore, J. R., Pankow, K. L., Ford, S. R., Koper, K. D., Hale, J. M., Aaron, J., & Larsen, C. F. (2017). Dynamics of the Bingham Canyon rock avalanches (Utah, USA) resolved from topographic, seismic, and infrasonic data. *Journal of Geophysical Research: Earth Surface*, *122*(3), 615–640. <https://doi.org/10.1002/2016JF004036>
- Moran, S. C., Matoza, R. S., Garcés, M. A., Hedlin, M. A. H., Bowers, D., Scott, W. E., Sherrod, D. R., & Vallance, J. W. (2008). Seismic and acoustic recordings of an unusually large rockfall at Mount St. Helens, Washington. *Geophysical Research Letters*, *35*(19), L19302. <https://doi.org/10.1029/2008GL035176>
- Moretti, L., Allstadt, K., Mangeney, A., Capdeville, Y., Stutzmann, E., & Bouchut, F. (2015). Numerical modeling of the Mount Meager landslide constrained by its force history derived from seismic data. *Journal of Geophysical Research: Solid Earth*, *120*(4), 2579–2599. <https://doi.org/10.1002/2014JB011426>
- Moretti, L., Mangeney, A., Capdeville, Y., Stutzmann, E., Huggel, C., Schneider, D., & Bouchut, F. (2012). Numerical modeling of the Mount Steller landslide flow history and of the generated long period seismic waves. *Geophysical Research Letters*, *39*(16), n/a-n/a. <https://doi.org/10.1029/2012GL052511>
- Perttu, A., Caudron, C., Assink, J., Metz, D., Tailpied, D., Perttu, B., Hibert, C., Nurfitriani, D., Pilger, C., Muzli, M., Fee, D., Andersen, O., & Taisne, B. (2020). Reconstruction of the 2018 tsunamigenic flank collapse and eruptive activity at Anak Krakatau based on eyewitness reports, seismo-acoustic and satellite observations. *Earth and Planetary Science Letters*, *541*, 116268. <https://doi.org/10.1016/j.epsl.2020.116268>
- Plafker, G., & Ericksen, G. E. (1978). Nevados Huascarán avalanches, Peru. In B. Voight (Ed.), *Developments in geotechnical engineering* (Vol. 14, pp. 277–314). Elsevier. <https://doi.org/10.1016/B978-0-444-41507-3.50016-7>

- Poppeliers, C., Wheeler, L. B., & Preston, L. (2020). The effects of atmospheric models on the estimation of infrasonic source functions at the Source Physics Experiment. *Bulletin of the Seismological Society of America*, 1–13. <https://doi.org/10.1785/0120190241>
- Power, J. A., Haney, M. M., Botnick, S. M., Dixon, J. P., Fee, D., Kaufman, A. M., Ketner, D. M., Lyons, J. J., Parker, T., Paskievitch, J. F., Read, C. W., Searcy, C., Stihler, S. D., Tepp, G., & Wech, A. G. (2020). Goals and development of the Alaska Volcano Observatory seismic network and application to forecasting and detecting volcanic eruptions. *Seismological Research Letters*. <https://doi.org/10.1785/0220190216>
- Ripepe, M., De Angelis, S., Lacanna, G., Poggi, P., Williams, C., Marchetti, E., Donne, D. D., & Olivieri, G. (2009). Tracking pyroclastic flows at Soufrière Hills Volcano. *Eos, Transactions American Geophysical Union*, 90(27), 229. <https://doi.org/10.1029/2009EO270001>
- Ripepe, M., De Angelis, S., Lacanna, G., & Voight, B. (2010). Observation of infrasonic and gravity waves at Soufrière Hills Volcano, Montserrat. *Geophysical Research Letters*, 37(19), n/a-n/a. <https://doi.org/10.1029/2010GL042557>
- Roman, D. C., Power, J. A., Moran, S. C., Cashman, K. V., Doukas, M. P., Neal, C. A., & Gerlach, T. M. (2004). Evidence for dike emplacement beneath Iliamna Volcano, Alaska in 1996. *Journal of Volcanology and Geothermal Research*, 130(3-4), 265–284. [https://doi.org/10.1016/S0377-0273\(03\)00302-0](https://doi.org/10.1016/S0377-0273(03)00302-0)
- Sanderson, R. W., Matoza, R. S., Fee, D., Haney, M. M., & Lyons, J. J. (2020). Remote Detection and Location of Explosive Volcanism in Alaska With the EarthScope Transportable Array. *Journal of Geophysical Research: Solid Earth*, 125(4), e2019JB018347. <https://doi.org/10.1029/2019JB018347>
- Schimmel, A., & Hübl, J. (2016). Automatic detection of debris flows and debris floods based on a combination of infrasound and seismic signals. *Landslides*, 13(5), 1181–1196. <https://doi.org/10.1007/s10346-015-0640-z>
- Schimmel, A., Hübl, J., McArdell, B., & Walter, F. (2018). Automatic identification of alpine mass movements by a combination of seismic and infrasound sensors. *Sensors*, 18(5), 1658. <https://doi.org/10.3390/s18051658>
- Schneider, D., Bartelt, P., Caplan-Auerbach, J., Christen, M., Huggel, C., & McArdell, B. W. (2010). Insights into rock-ice avalanche dynamics by combined analysis of seismic recordings and a numerical avalanche model. *Journal of Geophysical Research: Earth Surface*, 115(4), 1–20. <https://doi.org/10.1029/2010JF001734>
- Schneider, D., Huggel, C., Haerberli, W., & Kaitna, R. (2011). Unraveling driving factors for large rock-ice avalanche mobility. *Earth Surface Processes and Landforms*, 36(14), 1948–1966. <https://doi.org/10.1002/esp.2218>

- Schöpa, A., Chao, W.-A., Lipovsky, B. P., Hovius, N., White, R. S., Green, R. G., & Turowski, J. M. (2018). Dynamics of the Askja caldera July 2014 landslide, Iceland, from seismic signal analysis: precursor, motion and aftermath. *Earth Surface Dynamics*, *6*(2), 467–485. <https://doi.org/10.5194/esurf-6-467-2018>
- Schwaiger, H. F., Iezzi, A. M., & Fee, D. (2019). AVO-G2S: A modified, open-source Ground-to-Space atmospheric specification for infrasound modeling. *Computers & Geosciences*, *125*(February 2018), 90–97. <https://doi.org/10.1016/j.cageo.2018.12.013>
- Tape, C., Christensen, D., Moore-Driskell, M. M., Sweet, J., & Smith, K. (2017). Southern Alaska Lithosphere and Mantle Observation Network (SALMON): A seismic experiment covering the active arc by road, boat, plane, and helicopter. *Seismological Research Letters*, *88*(4), 1185–1202. <https://doi.org/10.1785/0220160229>
- Uieda, L., Tian, D., Leong, W. J., Jones, M., Schlitzer, W., Grund, M., Toney, L., Yao, J., Magen, Y., Materna, K., Frölich, Y., Belem, A., Newton, T., Anant, A., Ziebarth, M., Quinn, J., & Wessel, P. (2022). *PyGMT: A Python interface for the Generic Mapping Tools*. Zenodo. <https://doi.org/10.5281/zenodo.6702566>
- Ulivieri, G., Marchetti, E., Ripepe, M., Chiambretti, I., De Rosa, G., & Segor, V. (2011). Monitoring snow avalanches in Northwestern Italian Alps using an infrasound array. *Cold Regions Science and Technology*, *69*(2-3), 177–183. <https://doi.org/10.1016/j.coldregions.2011.09.006>
- Voight, B. (Ed.). (1978). *Rockslides and Avalanches, 1: Natural Phenomena* (Vol. 14). Elsevier.
- Waxler, R. M., Assink, J. D., Hetzer, C., & Velea, D. (2017). NCPAprop—A software package for infrasound propagation modeling. *The Journal of the Acoustical Society of America*, *141*(5), 3627–3627. <https://doi.org/10.1121/1.4987797>
- Waythomas, C., Miller, T., & Begét, J. (2000). Record of late Holocene debris avalanches and lahars at Iliamna Volcano, Alaska. *Journal of Volcanology and Geothermal Research*, *104*(1-4), 97–130. [https://doi.org/10.1016/S0377-0273\(00\)00202-X](https://doi.org/10.1016/S0377-0273(00)00202-X)
- Waythomas, C. F., & Miller, T. P. (1999). *Preliminary volcano-hazard assessment for Iliamna Volcano, Alaska: U.S. Geological Survey Open-File Report 99-373*, 31 p.
- Werner, C. A., Doukas, M. P., & Kelly, P. J. (2011). Gas emissions from failed and actual eruptions from Cook Inlet Volcanoes, Alaska, 1989–2006. *Bulletin of Volcanology*, *73*(2), 155–173. <https://doi.org/10.1007/s00445-011-0453-4>
- Wessel, P., Luis, J. F., Uieda, L., Scharroo, R., Wobbe, F., Smith, W. H. F., & Tian, D. (2019). The Generic Mapping Tools Version 6. *Geochemistry, Geophysics, Geosystems*, *20*(11), 5556–5564. <https://doi.org/10.1029/2019GC008515>

- Yamasato, H. (1997). Quantitative analysis of pyroclastic flows using infrasonic and seismic data at Unzen Volcano, Japan. *Journal of Physics of the Earth*, 45(6), 397–416. <https://doi.org/10.4294/jpe1952.45.397>
- Zimmer, V. L., Collins, B. D., Stock, G. M., & Sitar, N. (2012). Rock fall dynamics and deposition: An integrated analysis of the 2009 Ahwiyah Point rock fall, Yosemite National Park, USA. *Earth Surface Processes and Landforms*, 37(6), 680–691. <https://doi.org/10.1002/esp.3206>
- Zimmer, V. L., & Sitar, N. (2015). Detection and location of rock falls using seismic and infrasound sensors. *Engineering Geology*, 193, 49–60. <https://doi.org/10.1016/j.enggeo.2015.04.007>

Chapter 3: Waveform Features Strongly Control Subcrater Classification Performance for a Large, Labeled Volcano Infrasonic Dataset[‡]

3.1 Abstract

Volcano infrasound data contain a wealth of information about eruptive patterns, for which machine learning (ML) is an emerging analysis tool. Although global catalogs of labeled infrasound events exist, the application of supervised ML to local (< 15 km) volcano infrasound signals has been limited by a lack of robust labeled datasets. Here, we automatically generate a labeled dataset of > 7,500 explosions recorded by a five-station infrasound network at the highly-active Yasur Volcano, Vanuatu. Explosions are located via backprojection and associated with one of Yasur's two summit subcraters. We then apply a supervised ML approach to classify the subcrater of origin. When trained and tested on data from the same station, our chosen algorithm is > 95% accurate; when training and testing on different stations, accuracy drops to about 75%. The choice of waveform features provided to the algorithm strongly influences classification performance.

3.2 Introduction

Machine learning (ML) has shown promise within seismology and infrasound studies for finding patterns in waveforms that are not easily perceived by humans, and for automating large-scale data analysis (Kong et al., 2019). In a volcanic context, ML can identify eruptive trends and help reduce analyst workload (Carniel & Raquel Guzmán, 2020). However, the application of supervised ML to local volcano infrasound signals has to date been limited by a lack of large labeled datasets. Therefore, previous research has focused on unsupervised techniques, with a limited number of supervised approaches using relatively small labeled datasets. Feature extraction — the process of summarizing data examples by calculating a

[‡]Toney, L., Fee, D., Witsil, A., & Matoza, R. S. (2022). Waveform features strongly control subcrater classification performance for a large, labeled volcano infrasound dataset. *The Seismic Record*, 2(3), 167–175. <https://doi.org/10.1785/0320220019>

collection of waveform attributes — is a key step in ML pipelines (Christ et al., 2018). These studies have employed diverse approaches for feature extraction, with variable results.

At Etna (Italy), Cannata et al. (2011) used an unsupervised algorithm to cluster infrasound signals into three groups, and then used those groups to train a support vector machine (SVM) to recognize the active vent with implications for monitoring. A. J. Witsil and Johnson (2020) and Watson (2020) used unsupervised learning to cluster recorded infrasound signals — at Stromboli (Italy) and Etna, respectively — into groups representing different modes of activity, and then analyzed the contributions of these groups over time to characterize changing eruptive modes. Liu et al. (2014) achieved an accuracy of 98% using SVMs to classify volcano, tsunami, and earthquake classes using features derived from the Hilbert–Huang transform, while Li et al. (2016) obtained an accuracy of 86% using a different feature extraction technique (spectral entropy). Ortiz et al. (2020) applied unsupervised clustering to infrasound array detections for three volcanoes in Ecuador, finding good agreement with analyst-derived explosion catalogs.

The aforementioned supervised approaches (Li et al., 2016; Liu et al., 2014) were successful but limited by their small, manually-created training datasets. This motivates the development of methods which produce large volumes of training data automatically. Here, we algorithmically generate a labeled dataset and then apply a supervised learning approach to classify the subcrater of origin for Strombolian explosion signals recorded by a local infrasound network at Yasur Volcano, Vanuatu. Yasur is a basaltic-andesitic scoria cone located on Tanna Island in the island nation of Vanuatu (Figure 3.1a) (Iezzi et al., 2019). The volcano is continuously active, producing thousands of explosions per day from various vents, and its summit consists of a bifurcated crater containing two subcraters, termed “S” and “N” for “south” and “north,” respectively (Jolly et al., 2017; Simons et al., 2020). There were multiple vents active in the two subcraters during the deployment whose data we use here (Jolly et al., 2017; Matoza et al., 2022). In addition to classifying the labeled explosion

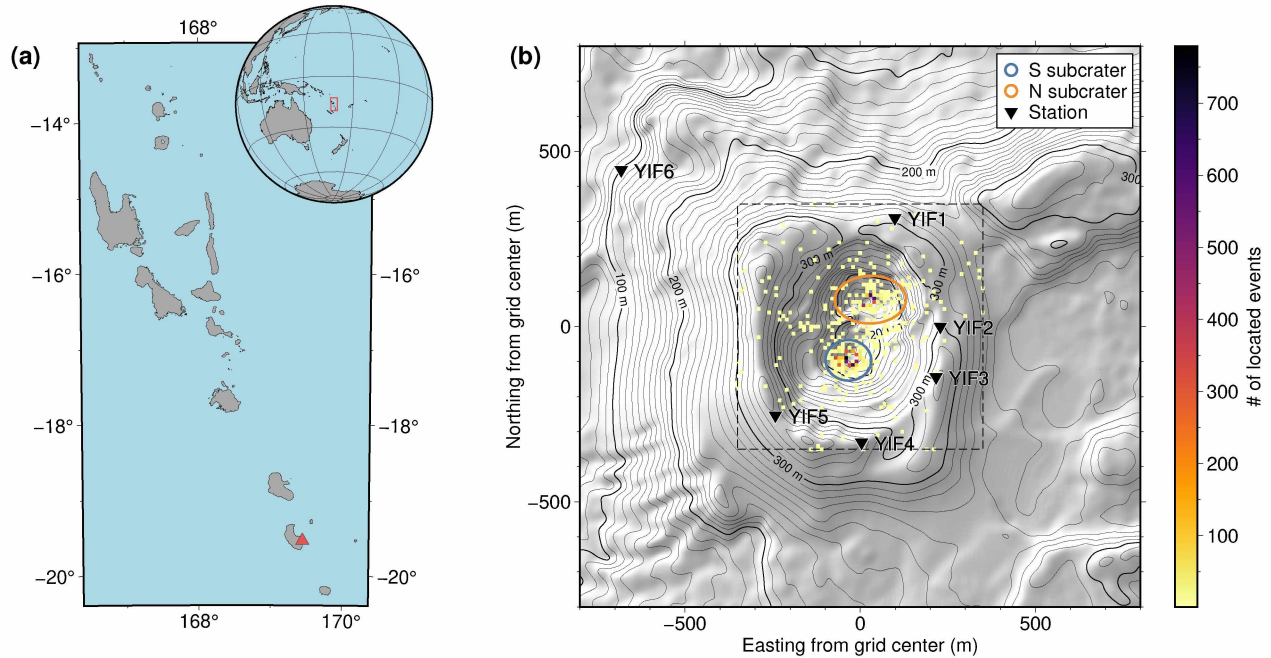


Figure 3.1 Map of the study region. **(a)** Location of the nation of Vanuatu. The red box in the globe inset has the same extent as the main map. Yasur Volcano is indicated with a red triangle. **(b)** Spatial histogram of 7,877 RTM-FDTD locations generated over the six-day-long deployment, overlain on a shaded relief map of Yasur Volcano. Ellipses denote $2\text{-}\sigma$ regions for the south and north subcraters. Dashed box delineates grid search bounds for RTM-FDTD. Infrasound stations are denoted by black inverted triangles.

waveforms, we explore the effects of different extracted waveform features on classification performance.

3.3 Data

We use data from a six-day-long deployment at Yasur which took place in July–August 2016 (Fee, Matoza, & Jolly, 2016). The infrasound component of the deployment comprised a ground-based network of sensors surrounding the summit crater of Yasur (Figure 3.1b) as well as sensors connected to a tethered aerostat. For more deployment information, see Jolly et al. (2017), Iezzi et al. (2019), and Matoza et al. (2022).

In this work, we use data from ground-based stations YIF1–YIF5. Station YIF6 was not online for the entire deployment. These five Chaparral Model 60 sensors recorded data at 400

Hz sampling rate for approximately 138 hours from 04:00 on 27 July to 22:00 on 1 August (these and all following times in UTC) (Figure 3.2a). We downsample all data to 50 Hz and apply a 0.2–4 Hz bandpass filter before processing. This filter band proved effective for locating explosions in a previous study using this dataset (Fee et al., 2021).

3.4 Methods

Our classification goal is to determine whether a given explosion waveform originates from a vent in the south subcrater or a vent in the north subcrater. This is therefore a binary classification problem. To create our labeled dataset, we use a network-based algorithm to generate a catalog of event locations and associate these locations to a subcrater. We extract vectors of features from the waveforms in this dataset. Finally, we use the labeled feature vectors to train and test an ML classifier.

3.4.1 Creation of Labeled Dataset

Following Fee et al. (2021), we use the Python package *rtm* to locate acoustic sources via reverse time migration with finite-difference time-domain travel time removal (RTM–FDTD). RTM–FDTD computes travel times for acoustic waves propagating over a digital elevation model (DEM) of the complex topography of Yasur, which improves location accuracy and precision. The source search grid is 350×350 m with a grid spacing of 10 m and is centered on the midpoint between the two DEM minima corresponding to the lowest points in each subcrater. The grid spacing, chosen primarily for speed, does not allow us to reliably differentiate vents within each subcrater. Hence, we assume that inter-subcrater waveform variability is more significant than intra-subcrater waveform variability.

For RTM–FDTD, we process the waveforms from stations YIF1–YIF5 by decimating to 20 Hz — for computational speed — and applying a 60-s-long adaptive gain control (AGC), which reduces the dominance of large-amplitude signals on the stack function (Walker et al., 2010). The stack function comprises the sums of the amplitude envelopes of the processed,

normalized, and time-shifted waveforms of all five stations. To pick peaks in the stack function, we set a threshold of 4 (i.e., 80% of total possible stack value) and require a 30 s gap between adjacent peaks. This produces a catalog of 7,877 events over six days which is plotted as a spatial histogram in Figure 3.1b. We note that multiple explosions may occur within a single 30 s time window.

We fit a regularized two-component Gaussian mixture model to the collection of catalog locations to define a $2\text{-}\sigma$ confidence ellipse around each subcrater (see colored ellipses in Figure 3.1b). Located waveforms are associated with either the S or N subcrater if they fall within that subcrater distribution’s ellipse. After this association step, we arrive at a labeled catalog of 7,571 events: 5,036 S subcrater events and 2,535 N subcrater events. The temporal evolution of the labeled catalog is plotted in Figure 3.2b. We window waveforms from the continuous time series data using the catalog time t_0 (from RTM–FDTD) as the start time and $t_0 + 5$ s as the end time. Since each labeled event in the catalog is recorded on five stations, we have a total of 37,855 labeled waveforms (of which 25,180 are S subcrater and 12,675 are N subcrater). These labeled waveforms, summarized in Figure 3.2c,d, show impulsive initial transients followed by 1–2 seconds of coda.

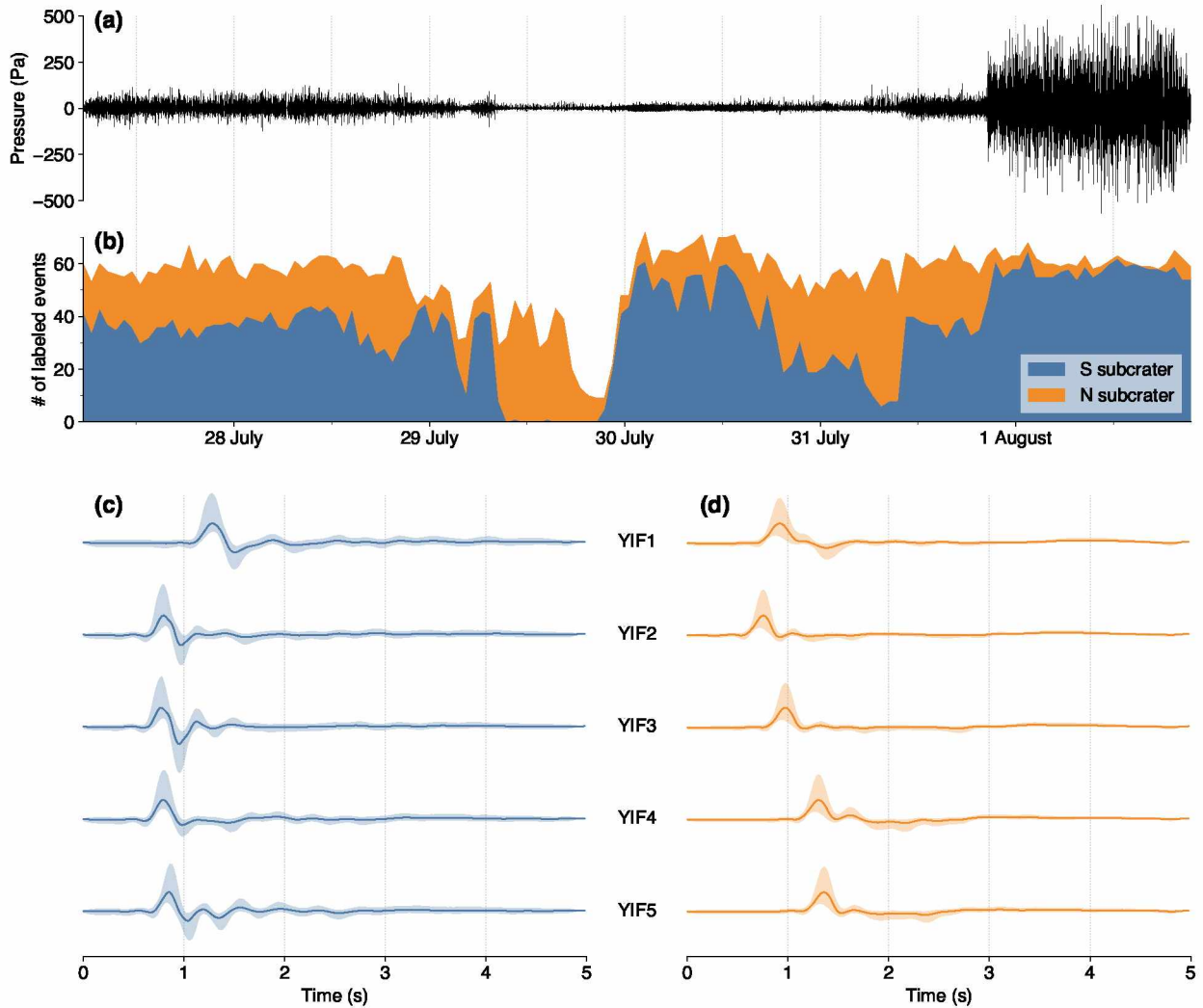


Figure 3.2 (a) Pressure waveform for station YIF3, filtered as described in the text. (b) Number of labeled S and N subcrater events computed in hour-long rolling windows. Medians (lines) and 25th and 75th percentiles (shaded regions) of (c) 25,180 S subcrater waveforms and (d) 12,675 N subcrater waveforms, plotted by station. Traces are filtered as described in the text and individually normalized to their median.

3.4.2 Feature Extraction

We extract features from the 250-sample-long labeled waveforms to input to our ML classifier. We remove the instrument response and normalize waveforms prior to feature extraction, and for two of the three extracted feature sets we apply a random time shift.

These steps minimize the effect of distance from the source on the feature signature of the waveforms by removing amplitude and travel time information, respectively.

A common issue with feature engineering is that one does not usually know which features are optimal for a given classification problem. A more rigorous approach is to use a large number of features and let an algorithm determine which are most relevant. We use the *TSFRESH* Python package (Christ et al., 2018) to automatically extract over 700 time- and frequency-domain features from the labeled waveforms. *TSFRESH* has been used in a volcanic context on seismic data from Whaakari / White Island, New Zealand (Dempsey et al., 2020).

The collection of hundreds of features likely includes many that are irrelevant for the classification task. To improve classification results, as well as make the algorithm more efficient, we select an optimal subset of 10 *TSFRESH* features: We apply sequential feature selection (SFS; Ferri et al., 1994) on data from the entire deployment across all stations. SFS is a greedy algorithm that iteratively picks the best-performing feature (evaluated using classification accuracy scores) from the available pool of features. These 10 features are listed in Table S1, available in the supplemental material to this article. We note that they are specific to the context of Yasur Volcano and the timeframe of the 2016 deployment, and that most do not have a clear physical meaning.

We additionally produce a full set of *TSFRESH* features from non-time-shifted waveforms (i.e., travel time is preserved), and, for comparison to the 10 SFS-selected *TSFRESH* features, a set of 10 features which have been employed for unsupervised ML classification on volcano infrasound (see, e.g., Watson, 2020; A. J. Witsil & Johnson, 2020). These previously-used features comprise statistical moments and measures of the time- and frequency-domain amplitude distributions, as well as four additional frequency domain features (for more information, see Table 1 in A. J. Witsil & Johnson, 2020). We refer to these features as the “manual” features, and note that they have been successful for previous unsupervised clustering analysis (Watson, 2020; A. J. Witsil & Johnson, 2020).

3.4.3 Support Vector Classification

We train a linear SVM classifier, as implemented in *scikit-learn* (Pedregosa et al., 2011), for each of the three extracted feature sets mentioned earlier. SVMs find the optimal hyperplane in feature space which maximizes the margin between the two classes of the training dataset. We initially chose SVMs over the myriad other options available because 1) it has been applied to infrasound data before (Albert & Linville, 2020; Cannata et al., 2011) and 2) it is a simple and easily interpretable classifier.

Temporal and station-wise subsets of the labeled catalog form our training and validation datasets. We formulate two classification problems to evaluate the performance of the SVM. We refer to these as the “generalization case” and the “same-station” case. The generalization case trains an SVM on a subset comprised of all but one day and all but one station of the total labeled dataset. The validation subset consists of data from the excluded station on the excluded day. The same-station case uses the same temporal subsetting as the generalization case, but for station-wise subsetting we train and test on one station at a time — including training and testing on the same station. We only show results from a temporal subset of 27–31 July (train) and 1 August (test). For each classification problem, we balance classes — after temporally subsetting — by downsampling the majority class.

3.5 Results

3.5.1 Trends in Labeled Catalog

The labeled catalog of events shows clear trends which correlate with waveform characteristics (Figure 3.2a,b). The relative contribution of events from the S and N subcraters is balanced, and the total number of events per hour is steady, until just before 29 July. The contribution from the S subcrater diminishes, and the total rate of events and average explosion amplitudes decline, until 30 July. At that time, the event rate returns to baseline and the contribution from the S subcrater varies from 20–80%. Finally, just before 1 August,

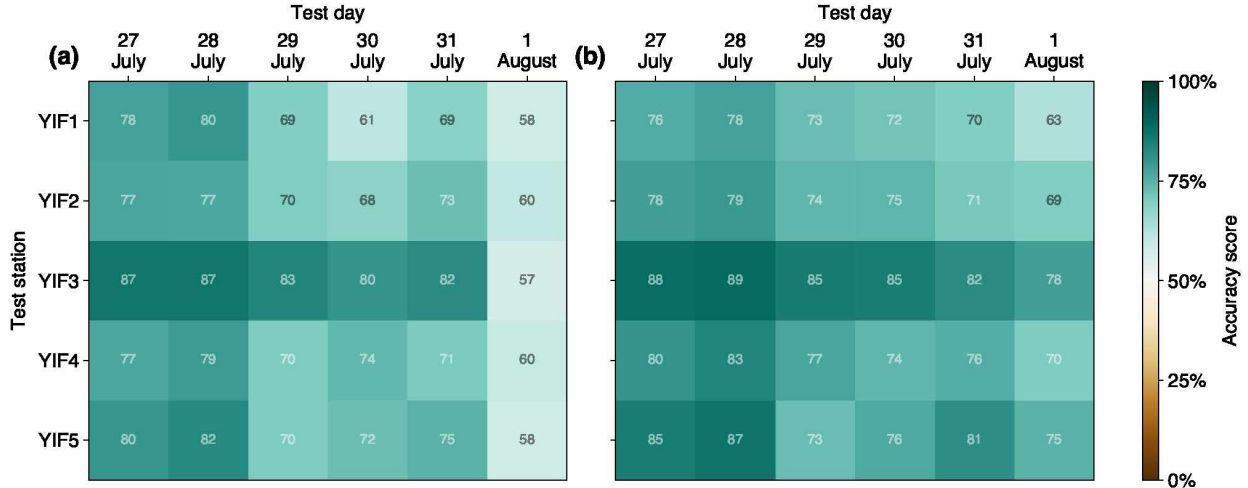


Figure 3.3 Accuracy scores for “generalization case” training/testing subsets using 10 manual features **(a)** and 10 SFS-selected *TSFRESH* features **(b)**. Each cell’s score is obtained by training on all available data excluding the given day (column) and station (row) of the cell. For example, in **(b)**, training on waveforms from stations YIF1–YIF4 between 28 July and 1 August results in 85% accuracy on validation waveforms from YIF5 on 27 July.

as explosion amplitudes increase dramatically, the contribution from the N subcrater shrinks to near-zero.

3.5.2 Classification Accuracy

We evaluate all classification problems using the classification accuracy score, which is the fraction of correct classifications out of the total number of classifications. For the generalization case, we achieve mean classification accuracies of 73% (maximum 87%) for time-shifted manual features (Figure 3.3a) and 77% (maximum 89%) for SFS-selected time-shifted *TSFRESH* features (Figure 3.3b). The SFS-selected *TSFRESH* features have more uniform accuracy scores across the matrix, but especially during 1 August, when compared to the manual features.

Classification accuracies for the same-station case are shown in Figure 3.4a. We obtain a mean same-station (diagonal in Figure 3.4a) classification accuracy of 96% using all non-time-shifted *TSFRESH* features, averaging over all six temporal train-test partitions. The

maximum single-station score, 99%, occurs for station YIF1 when testing on 1 August, the final day of the deployment (top-left entry in Figure 3.4a). Note that Figure 3.4a shows the accuracies for a problem where we test on 1 August. The off-diagonal entries in Figure 3.4a, which represent the classifier’s generalization to different stations, generally show progressively poorer performance for stations that are farther away from each other. However, a correlation between the accuracies for stations YIF4 and YIF5 is evident.

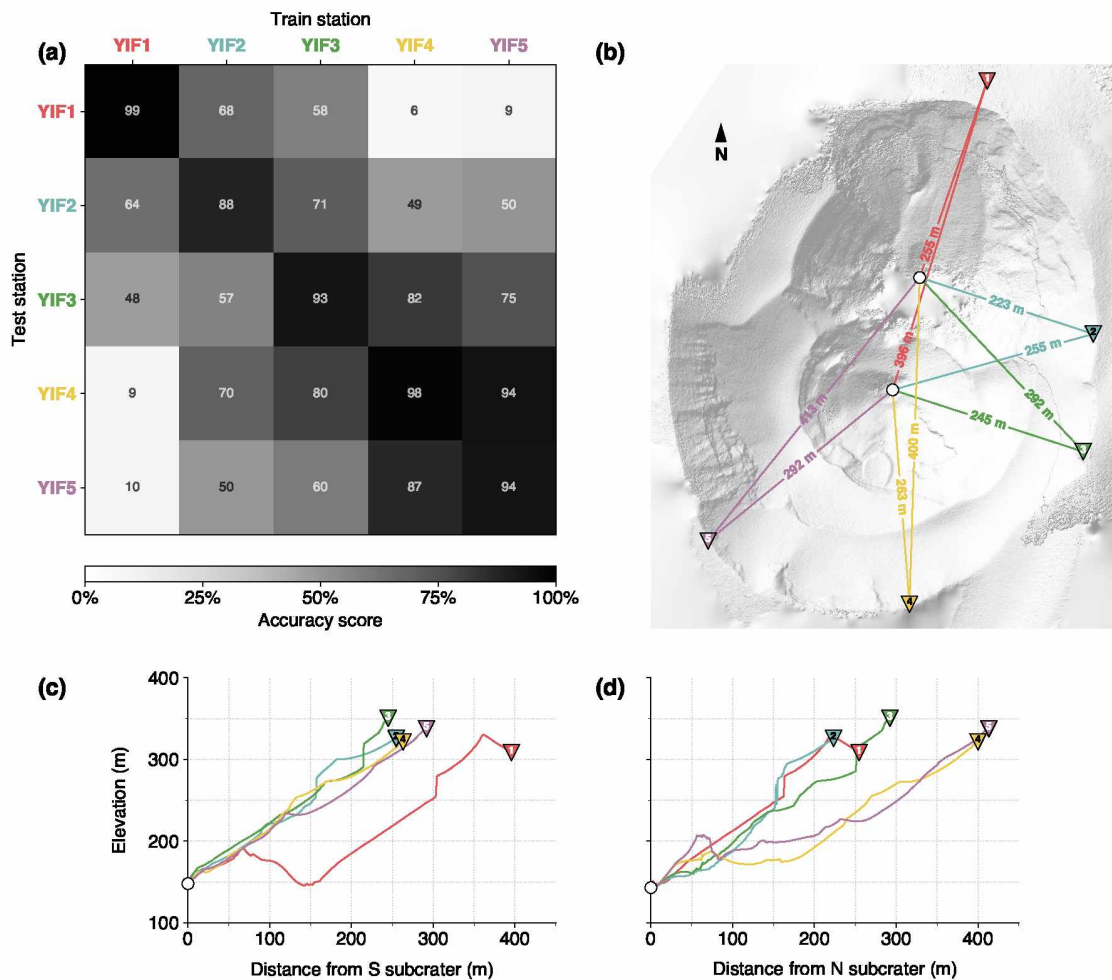


Figure 3.4 Accuracy scores and subcrater–station geometry and profiles. **(a)** Accuracy scores for various “same-station case” train-test pairings using non-time-shifted *TSFRESH* features. The training time window is 27–31 July; we test on 1 August. **(b)** Map view showing distances from each station to the bottom of each subcrater (subcrater locations are estimated from digital elevation model minima). Vertical profiles from the south subcrater **(c)** and the north subcrater **(d)** to each station. Spatial scale is identical to **(b)**. For station legend, see colors in **(a)**.

3.6 Discussion

We show here that starting with a large collection of features and employing an automated feature selection scheme can yield superior classification results when compared to using domain-knowledge derived (“manual”) features (Figure 3.3). This automated feature extraction and selection scheme is superior because it makes fewer assumptions about the system. Note, however, that we are still limited by the features built into *TSFRESH*. There are perhaps additional features which are relevant for a classification problem that are not contained within the *TSFRESH* feature set. This is where a deep learning approach may deliver a superior classification result, since such an approach avoids explicit feature specification altogether. One important trade-off, however, is interpretability: Though outside the scope of this article, with linear SVMs we can examine the weights (hyperplane coefficients) of each feature to understand how the classifier is behaving. Furthermore, one can explore eruptive source processes and propagation effects through the feature importances. This is more challenging, though not impossible, with deep learning algorithms.

Yasur Volcano is a dynamic system, and even on the six-day-long timescale of this study, notable changes in the intensity of activity are observed (Figure 3.2a,b) which are consistent with seismoacoustic analyses of Matoza et al. (2022). Furthermore, Yasur’s bifurcated summit crater and its associated topographic features have a large impact on the character of recorded infrasound (Fee et al., 2021; Iezzi et al., 2019). Both of these volcano-specific factors pose challenges for classification, because a useful classification workflow inherently involves generalization either to new time periods or new station locations at the same volcano (or at a different volcano altogether). Furthermore, our catalog is automatically labeled, so there are likely misclassified events or noise (however, manual inspection of labeled waveforms did not indicate that such misclassifications were common). It is critical to note that these challenges can be addressed through clever training, design, and application of the classification algorithm. For example, training on a diverse collection of waveforms, or leveraging data augmentation (A. Witsil et al., 2022), can improve generalization.

The same-station classification results shown in Figure 3.4a demonstrate excellent generalization in time and poor generalization to other stations. Plots like Figure 3.4a produced for different test days show similar or superior results — this is because, by testing on the final day of the deployment when the eruptive pattern was different (Figure 3.2a,b), we are challenging the algorithm to work on an eruptive period unlike what it encountered during training. Generalization to other stations is poor due to vast differences in topographic path between source and receiver. Figures 3.4b–d show map and profile views of the paths from each subcrater DEM minimum to each station. Source–receiver distances and topographic complexity vary considerably. This has profound effects on generalization, which we illustrate with two examples below.

1. Consider training on YIF1 and testing on YIF5 (Figure 3.4a). The model learns to associate a smaller travel time with the N subcrater, as that subcrater is closer to YIF1. When we test this model using data from YIF5, the classification accuracy is 10%, i.e., the algorithm picks the wrong subcrater 90% of the time. Examining Figure 3.4b we see that the smaller travel time for YIF5 is associated with the S subcrater, not the N subcrater.
2. There is a strong correlation between YIF4 and YIF5 accuracies (Figure 3.4a). This is explained by the relative similarity of the path lengths between each subcrater and YIF4 and YIF5, and the similar topographic profiles seen in Figure 3.4c,d. This similarity allows a model trained using YIF4 data to perform well on YIF5 data, and vice versa — the topographic effect on the waveforms is similar for these similar paths.

Both of these examples suggest that the features used for this problem — non-time-shifted *TSFRESH* features — are strongly path-dependent. (See Figure S1 for a version of Figure 4a made using time-shifted *TSFRESH* features.) These examples showcase the importance of feature extraction on classification results. This has implications for future ML studies where feature engineering is necessary. Randomly time-shifting waveforms is a basic step

towards removing the effect of path; a more rigorous approach could involve deconvolving the full numerically-computed Green’s function from each labeled explosion waveform. Such an approach would allow a classifier to train directly on features more closely linked to the explosion source, as opposed to path, and would help the classifier generalize to new network geometries. However, we note that to maximize classifier accuracy for a fixed path, waveform path information should be retained, as it provides additional information useful for determining the correct location (e.g., modification of waveform spectra by vent-proximal topography, (Johnson et al., 2018)).

Using an SVM, we achieve classification accuracies on par with Cannata et al. (2011), who used a single station to achieve 95% accuracy classifying explosive events to either of Etna’s Southeast and Northeast Craters. Cannata et al. (2011) used a three-dimensional feature space composed of frequency and quality factor and peak-to-peak amplitude. Note that we discard amplitude information by normalizing each labeled waveform, but for same-station classification we retain travel time information. Albert and Linville (2020) used SVMs to obtain 75% accuracy for a binary source type classification (volcano versus earthquake) problem. Large path differences between the globally-recorded waveforms used in their study reduced the generalization performance of their algorithm. While our study is not directly comparable due to its local scale and classification type, we note that we also see a significant reduction in accuracy when we force the algorithm to generalize to new paths (e.g., compare Figure 3.3 to Figure 3.4a diagonal). Future improvements in ML-based volcano infrasound research could account for path effects through waveform modeling, as has been done in seismology (Kuang et al., 2021), or through synthetic training data such as in A. Witsil et al. (2022).

To compare our ML-based classification to a more traditional method, we use the stacked waveforms shown in Figure 3.2c,d as templates for a correlation analysis (e.g., Green & Neuberg, 2006). Details on this method and results are available in the supplemental material to this article. We obtain a mean same-station classification accuracy of 91%, which is lower

than the accuracy of 96% obtained using ML. We note that the key benefit of the ML application arises in situations where generalization to other stations is desired, as this is not possible using waveform correlation methods.

3.7 Conclusions

We assemble a large, multi-station, labeled dataset for a binary classification problem tasked with locating the source of explosive volcano infrasound signals within multiple subcraters using a crater-rim infrasound network at Yasur Volcano. We experiment with three different strategies for extracting features from the labeled waveforms: 10 “manual” features, 10 automatically selected *TSFRESH* features, and a full set of non-time-shifted *TSFRESH* features. For each of these strategies, we explore SVM classification performance and evaluate generalization potential for different time periods and different station combinations.

“Shallow learners” such as SVMs are readily interpretable, but they require explicitly-defined features which are often obtained from domain knowledge — this can be arbitrary and can introduce bias. The choice of features depends on the classification goal (generalization, Figure 3.3, or single-station performance, Figure 3.4). The 10 SFS-selected, time-shifted *TSFRESH* features are better suited for studying source processes and their variation over time (Watson, 2020; A. J. Witsil & Johnson, 2020), while the full set of non-time-shifted *TSFRESH* features are more useful for reliable location of explosive activity using a single station. Feature engineering is the most important aspect of classification workflow design for these problems.

Our very high single-station performance could be exploited to locate explosions to a subcrater or vent using data from a single permanent infrasound station (once an SVM was trained with data from, for example, a larger temporary network). The addition of a noise class would allow the algorithm, if running on rolling windows, to detect explosions as well as locate them. These applications are limited, however, in that any substantial change in crater morphology or atmosphere may violate the assumptions of the trained model.

This entire workflow (labeled dataset creation, training, and classification on new data) could be applied to other volcanoes or sources producing frequent explosions. Workflows such as this will only become more feasible and relevant as infrasound data volumes increase and more readily-labeled events are observed. A more ambitious goal would involve the application of this automatic labeled dataset generation technique to a source type classification problem; for example, image processing on video data to create a catalog of event source types. This approach would then be feasible even for single-vent systems. Future work should additionally assess the performance of deep learners such as convolutional neural networks on large, labeled infrasound datasets such as the one we introduce here.

3.8 Data and Resources

The data from this deployment are available through the IRIS Data Management Center as network code '3E' and station codes 'YBAL,YIB2,YIF1,YIF2,YIF3,YIF4,YIF5,YIF6' (Fee, Haney, et al., 2016).

The Python code written to perform this work — including labeled dataset creation — is publicly available under an MIT license on GitHub at https://github.com/liamtoney/yasur_ml; the code relies heavily upon the Python seismological framework *ObsPy* (Beyreuther et al., 2010). Figure 3.1 was made using *PyGMT* (v0.6.0; Uieda et al., 2022; Wessel et al., 2019). Figures 3.2–3.4 and S1 were made using *Matplotlib* (Hunter, 2007).

The supplemental material contains the methods for our cross-correlation analysis, supporting Table S1, and supporting Figure S1. This material can be accessed by clicking [here](#).

3.9 Acknowledgments

We thank Leighton Watson and another anonymous reviewer for their helpful comments on this manuscript.

We thank the Vanuatu Meteorology and Geohazards Department (Esline Garaebiti, Sandrine Cevuard, Janvion Cevuard, Athanase Worwor, and Julius Mala) and the entire field

team (David Fee, Robin Matoza, Alex Iezzi, Arthur Jolly, Richard Johnson, Bruce Christenson, Ben Kennedy, Geoff Kilgour, Nick Key, Rebecca Fitzgerald, Adrian Tessier, Allison Austin, and Di Christenson) for their efforts in obtaining the data used in this study. RSM acknowledges NSF grant EAR-1847736.

This work was supported by the Nuclear Arms Control Technology (NACT) program at the Defense Threat Reduction Agency (DTRA) through contract HDTRA121C0030. Cleared for release.

3.10 References

- Albert, S., & Linville, L. (2020). Benchmarking Current and Emerging Approaches to Infrasound Signal Classification. *Seismological Research Letters*, *91*(2A), 921–929. <https://doi.org/10.1785/0220190116>
- Beyreuther, M., Barsch, R., Krischer, L., Megies, T., Behr, Y., & Wassermann, J. (2010). ObsPy: A Python toolbox for seismology. *Seismological Research Letters*, *81*(3), 530–533. <https://doi.org/10.1785/gssrl.81.3.530>
- Cannata, A., Montalto, P., Aliotta, M., Cassisi, C., Pulvirenti, A., Privitera, E., & Patanè, D. (2011). Clustering and classification of infrasonic events at Mount Etna using pattern recognition techniques. *Geophysical Journal International*, *185*(1), 253–264. <https://doi.org/10.1111/j.1365-246X.2011.04951.x>
- Carniel, R., & Raquel Guzmán, S. (2020). Machine Learning in Volcanology: A Review. In K. Nemeth (Ed.), *Volcanoes - updates in volcanology*. IntechOpen. <https://doi.org/10.5772/intechopen.94217>
- Christ, M., Braun, N., Neuffer, J., & Kempa-Liehr, A. W. (2018). Time Series Feature Extraction on basis of Scalable Hypothesis tests (tsfresh – A Python package). *Neurocomputing*, *307*, 72–77. <https://doi.org/10.1016/j.neucom.2018.03.067>
- Dempsey, D. E., Cronin, S. J., Mei, S., & Kempa-Liehr, A. W. (2020). Automatic precursor recognition and real-time forecasting of sudden explosive volcanic eruptions at Whakaari, New Zealand. *Nature Communications*, *11*(1), 3562. <https://doi.org/10.1038/s41467-020-17375-2>
- Fee, D., Haney, M., Matoza, R., Szuberla, C., Lyons, J., & Waythomas, C. (2016). Seismic Envelope-Based Detection and Location of Ground-Coupled Airwaves from Volcanoes in Alaska. *Bulletin of the Seismological Society of America*, *106*(3), 1024–1035. <https://doi.org/10.1785/0120150244>

- Fee, D., Matoza, R. S., & Jolly, A. (2016). *Yasur volcano temporary deployment, summer 2016*. International Federation of Digital Seismograph Networks. <https://doi.org/10.7914/SN/3E2016>
- Fee, D., Toney, L., Kim, K., Sanderson, R. W., Iezzi, A. M., Matoza, R. S., De Angelis, S., Jolly, A. D., Lyons, J. J., & Haney, M. M. (2021). Local Explosion Detection and Infrasound Localization by Reverse Time Migration Using 3-D Finite-Difference Wave Propagation. *Frontiers in Earth Science*, 9, Article 620813. <https://doi.org/10.3389/feart.2021.620813>
- Ferri, F., Pudil, P., Hatef, M., & Kittler, J. (1994). Comparative study of techniques for large-scale feature selection. In *Machine intelligence and pattern recognition* (Vol. 16, pp. 403–413). <https://doi.org/10.1016/B978-0-444-81892-8.50040-7>
- Green, D. N., & Neuberg, J. (2006). Waveform classification of volcanic low-frequency earthquake swarms and its implication at Soufrière Hills Volcano, Montserrat. *Journal of Volcanology and Geothermal Research*, 153(1-2), 51–63. <https://doi.org/10.1016/j.jvolgeores.2005.08.003>
- Hunter, J. D. (2007). Matplotlib: A 2D graphics environment. *Computing in Science & Engineering*, 9(3), 90–95. <https://doi.org/10.1109/MCSE.2007.55>
- Iezzi, A. M., Fee, D., Kim, K., Jolly, A. D., & Matoza, R. S. (2019). Three-dimensional acoustic multipole waveform inversion at Yasur Volcano, Vanuatu. *Journal of Geophysical Research: Solid Earth*, 124(8), 8679–8703. <https://doi.org/10.1029/2018JB017073>
- Johnson, J. B., Watson, L. M., Palma, J. L., Dunham, E. M., & Anderson, J. F. (2018). Forecasting the Eruption of an Open-Vent Volcano Using Resonant Infrasound Tones. *Geophysical Research Letters*, 45(5), 2213–2220. <https://doi.org/10.1002/2017GL076506>
- Jolly, A. D., Matoza, R. S., Fee, D., Kennedy, B. M., Iezzi, A. M., Fitzgerald, R. H., Austin, A. C., & Johnson, R. (2017). Capturing the Acoustic Radiation Pattern of Strombolian Eruptions using Infrasound Sensors Aboard a Tethered Aero-
stat, Yasur Volcano, Vanuatu. *Geophysical Research Letters*, 44(19), 9672–9680. <https://doi.org/10.1002/2017GL074971>
- Kong, Q., Trugman, D. T., Ross, Z. E., Bianco, M. J., Meade, B. J., & Gerstoft, P. (2019). Machine Learning in Seismology: Turning Data into Insights. *Seismological Research Letters*, 90(1), 3–14. <https://doi.org/10.1785/0220180259>
- Kuang, W., Yuan, C., & Zhang, J. (2021). Real-time determination of earthquake focal mechanism via deep learning. *Nature Communications*, 12(1), 1432. <https://doi.org/10.1038/s41467-021-21670-x>

- Li, M., Liu, X., & Liu, X. (2016). Infrasound signal classification based on spectral entropy and support vector machine. *Applied Acoustics*, *113*, 116–120. <https://doi.org/10.1016/j.apacoust.2016.06.019>
- Liu, X., Li, M., Tang, W., Wang, S., & Wu, X. (2014). A New Classification Method of Infrasound Events Using Hilbert-Huang Transform and Support Vector Machine. *Mathematical Problems in Engineering*, *2014*, 1–6. <https://doi.org/10.1155/2014/456818>
- Matoza, R. S., Chouet, B. A., Jolly, A. D., Dawson, P. B., Fitzgerald, R. H., Kennedy, B. M., Fee, D., Iezzi, A. M., Kilgour, G. N., Garaebiti, E., & Cevuard, S. (2022). High-rate very-long-period seismicity at Yasur volcano, Vanuatu: Source mechanism and decoupling from surficial explosions and infrasound. *Geophysical Journal International*, *187*(4)(June), 717–725. <https://doi.org/10.1093/gji/ggab533>
- Ortiz, H. D., Matoza, R. S., Garapaty, C., Rose, K., Ramón, P., & Ruiz, M. C. (2020). Multi-year regional infrasound detection of Tungurahua, El Reventador, and Sangay volcanoes in Ecuador from 2006 to 2013. In *Proceedings of meetings on acoustics* (Vol. 41, p. 022003). <https://doi.org/10.1121/2.0001362>
- Pedregosa, F., Varoquaux, G., Gramfort, A., Michel, V., Thirion, B., Grisel, O., Blondel, M., Prettenhofer, P., Weiss, R., Dubourg, V., Vanderplas, J., Passos, A., Cournapeau, D., Brucher, M., Perrot, M., & Duchesnay, E. (2011). Scikit-learn: Machine Learning in Python. *Journal of Machine Learning Research*, *12*, 2825–2830.
- Simons, B. C., Cronin, S. J., Eccles, J. D., Jolly, A. D., Garaebiti, E., & Cevuard, S. (2020). Spatiotemporal variations in eruption style and magnitude at Yasur volcano, Vanuatu: part 2—extending Strombolian eruption classifications. *Bulletin of Volcanology*, *82*(11), 70. <https://doi.org/10.1007/s00445-020-01404-5>
- Uieda, L., Tian, D., Leong, W. J., Jones, M., Schlitzer, W., Grund, M., Toney, L., Yao, J., Magen, Y., Materna, K., Frölich, Y., Belem, A., Newton, T., Anant, A., Ziebarth, M., Quinn, J., & Wessel, P. (2022). *PyGMT: A Python interface for the Generic Mapping Tools*. Zenodo. <https://doi.org/10.5281/zenodo.6702566>
- Walker, K. T., Hedlin, M. A. H., de Groot-Hedlin, C., Vergoz, J., Le Pichon, A., & Drob, D. P. (2010). Source location of the 19 February 2008 Oregon bolide using seismic networks and infrasound arrays. *Journal of Geophysical Research*, *115*(B12), B12329. <https://doi.org/10.1029/2010JB007863>
- Watson, L. M. (2020). Using unsupervised machine learning to identify changes in eruptive behavior at Mount Etna, Italy. *Journal of Volcanology and Geothermal Research*, *405*, 107042. <https://doi.org/10.1016/j.jvolgeores.2020.107042>

- Wessel, P., Luis, J. F., Uieda, L., Scharroo, R., Wobbe, F., Smith, W. H. F., & Tian, D. (2019). The Generic Mapping Tools Version 6. *Geochemistry, Geophysics, Geosystems*, *20*(11), 5556–5564. <https://doi.org/10.1029/2019GC008515>
- Witsil, A., Fee, D., Dickey, J., Pena, R., Waxler, R., & Blom, P. (2022). Detecting Large Explosions with Machine Learning Models Trained on Synthetic Infrasound Data. *Geophysical Research Letters*, 1–15. <https://doi.org/10.1029/2022GL097785>
- Witsil, A. J., & Johnson, J. B. (2020). Analyzing continuous infrasound from Stromboli volcano, Italy using unsupervised machine learning. *Computers & Geosciences*, *140*(January), 104494. <https://doi.org/10.1016/j.cageo.2020.104494>

Chapter 4: Examining Infrasound Propagation at High Spatial Resolution Using a Nodal Seismic Array[§]

4.1 Abstract

Infrasound — acoustic waves in the atmosphere below 20 Hz — is a useful monitoring tool. Topography and atmospheric structure strongly control infrasound propagation, and at common source–receiver distances neither of these effects can be ignored when quantitative source constraints are sought. Detailed spatial measurements of the infrasound wavefield would inform propagation models and improve source estimates. However, the “large-N” deployment strategy now well-known in seismology has not yet been realized for infrasound studies. Here, we use the 900-node seismic array from the 2014 Imaging Magma Under St. Helens (iMUSH) experiment as a proxy for a large-N infrasound network, by leveraging acoustic–seismic coupled arrivals. The active-source component of iMUSH consisted of 23 shallowly buried explosions around Mount Saint Helens volcano; these explosions produced epicentral infrasound recorded on the nodes. We find that the bulk presence of ground-coupled infrasound on the nodes is controlled by wind noise and source–receiver distance, with observed arrivals for eight explosions. Explosions with the most extensive coupling produce complex spatial waveform patterns across the array. These patterns are related to both topographic and atmospheric propagation effects, as well as spatially variable site (coupling) effects. We compare our observations to simple topographic diffraction and high-resolution wind advection models and full-wave numerical simulations. We find strong spatial correlations between (1) coupled arrival strength and modeled topographic obstruction and (2) coupled arrival time and along-path winds. Our seismoacoustic analyses and results are applicable to other existing and future nodal seismic datasets and can expand the utility of such deployments.

[§]Toney, L., Fee, D., Schmandt, B., & Bishop, J. W. (in review). Examining infrasound propagation at high spatial resolution using a nodal seismic array. *Journal of Geophysical Research: Solid Earth*.

4.2 Introduction

Infrasound, or atmospheric acoustic waves with frequencies < 20 Hz, is a useful tool for monitoring and characterizing surface or near-surface environmental and anthropogenic processes. Such processes include volcanic eruptions (Fee & Matoza, 2013; J. B. Johnson & Ripepe, 2011; Watson et al., 2022), surficial mass movements (Allstadt et al., 2018; Kogelnig et al., 2014), glacial dynamics (Campus & Christie, 2010; Marchetti et al., 2021), anthropogenic explosions (Ceranna et al., 2009; Che et al., 2021; Hedlin et al., 2002), and even earthquakes (J. Johnson et al., 2020; Mutschlecner, 2005). An understanding of infrasound propagation is essential for optimizing detection and quantitative characterization of these infrasound sources.

Infrasound propagation is generally regarded to be dominated by topographic effects (scattering, diffraction, etc.) at local (< 15 km from source; Fee & Matoza, 2013) distances (e.g., Lacanna & Ripepe, 2013) and atmospheric effects (waveguides formed by temperature and horizontal winds) at regional (> 50 km from source) distances (e.g., Iezzi et al., 2019). However, there exists an intermediate source–receiver distance zone where neither atmospheric nor topographic propagation effects can be neglected (Lacanna et al., 2014). This intermediate zone poses a challenge to infrasound propagation modeling: it is computationally expensive to numerically simulate 3D infrasound propagation over topography in these relatively large domains (K. Kim & Pasyanos, 2022), and existing atmospheric specifications commonly used in propagation modeling schemes do not capture the smaller-scale complexities of the temperature and wind fields (K. Kim & Rodgers, 2017).

Infrasound is typically recorded using one or both of two distinct deployment styles: networks of single sensors and collections of multi-sensor arrays. Both of these styles provide spatially sparse wavefield sampling compared to their seismic counterparts. In particular, so-called “large-N” seismic sensor deployments have yielded subsurface images of unprecedented resolution (Karplus & Schmandt, 2018). To date, this deployment strategy — while common in industry applications (Dean et al., 2018) and growing popular in academic seis-

mology (Sweet et al., 2018) — has not been realized for infrasound studies. However, the nodal seismometers typically used in large-N arrays are well-suited to record acoustic–seismic coupled energy due to their surficial location (e.g., see Novoselov et al., 2020).

Acoustic–seismic coupling refers to the transfer of atmospheric acoustic energy into the ground, which can be recorded by seismometers. Such arrivals, sometimes referred to as “ground-coupled airwaves,” have been observed from numerous aerial sources such as bolides (Walker et al., 2010) and air traffic (Meng & Ben-Zion, 2018). The nature of acoustic–seismic coupling is sensitive to near-surface geological properties (Novoselov et al., 2020; Wills et al., 2022) and acoustic wave incidence angle, and therefore can exhibit significant spatial variability (Bishop et al., 2022). Seismic–acoustic coupling refers to the generation of acoustic waves in the atmosphere from seismic waves traveling or incident on Earth’s surface. Such coupling in the near-source region, or “epicentral” infrasound, is observed for large earthquakes and buried explosions (Arrowsmith et al., 2010; Averbuch et al., 2020; J. Johnson et al., 2020). Seismic–acoustic coupling proximal to the receiver, or “local” infrasound, has been used to calibrate infrasound sensors (Fee et al., 2023; T. S. Kim, 2004) and even compute earthquake magnitudes (Macpherson et al., 2023). In this work, we analyze propagating epicentral infrasound from buried explosions.

The Imaging Magma Under St. Helens (iMUSH) seismic imaging experiment took place during 2014–2016 at Mount Saint Helens volcano (MSH) in Washington state (Kiser et al., 2019; Ulberg et al., 2020). The active-source portion of the experiment consisted of 23 shallowly buried (~ 24 m depth) chemical explosions during a nine-day-long interval in July and August 2014 (Figure 4.1). The eight shots farthest from MSH had 900 kg charge weights, while the remaining shots had 450 kg charge weights (R. Wang et al., 2020). About 900 vertical-component, 10-Hz nodes were deployed for approximately two weeks, contemporaneously with the active-source explosions, and recorded at 250 Hz sampling rate (Hansen & Schmandt, 2015). The nodal array was dense, with a median spacing between adjacent nodes of 209 m (minimum 24 m, maximum 636 m).

The iMUSH shots coupled energy into the atmosphere. This energy traveled as atmospheric acoustic waves and coupled into the ground at the nodes, in addition to being recorded on several regional infrasound stations. In this work, we leverage this seismic-acoustic and subsequent acoustic-seismic coupling phenomenon to investigate topographic and atmospheric effects on infrasound propagation in the intermediate (about 2–90 km) source-receiver distance zone formed by the shots and nodes. We process seismic data from the 23 shots as recorded on the nodal seismic array. We perform simple modeling to approximate the effects of topographic diffraction on the infrasound wavefield, and we quantitatively compare coupled infrasound arrival patterns with high-resolution wind data. We also perform 2D finite-difference modeling incorporating both topography and range-independent atmospheric profiles to compare with our dense coupled measurements.

4.3 Data & Methods

4.3.1 Seismic data processing

We cut shot gathers from the continuous nodal seismic data using the known shot times and locations. The start time of the waveforms in each shot gather is 30 s prior to the shot time. The end time is calculated by dividing the distance of the farthest node from the shot by an end-member minimum celerity (C ; distance / travel time) of 280 m/s. The number of waveforms per shot gather varies from ~ 860 to ~ 900 as a result of data availability gaps at some nodes for some shots. We remove the full instrument response and downsample the waveforms to 125 Hz before applying a 5–50 Hz bandpass filter. The bandpass corners are chosen to maximize signal-to-noise of the broadband coupled infrasound arrivals on the nodes.

To highlight the coupled infrasound arrival transients, we apply short-term average to long-term average ratio (STA/LTA; Allen, 1978) processing with the short-term average window length set to 0.2 s and the long-term average window length set to 2 s. Like the bandpass filter corners, these parameters were chosen as they best highlighted the coupled

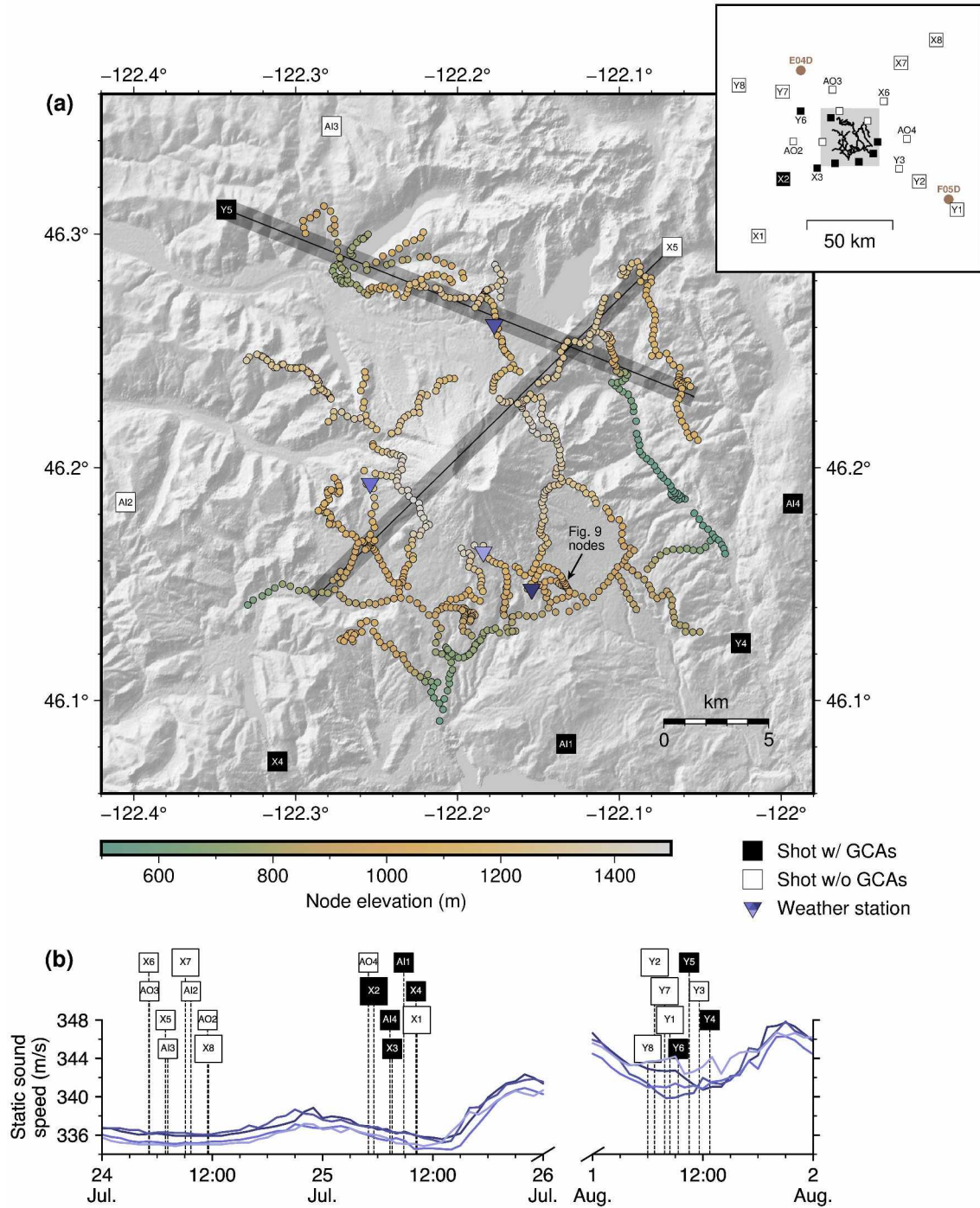


Figure 4.1 (a) Shaded relief map of the Mount Saint Helens vicinity showing nodes (circles), iMUSH shot locations (squares), and weather stations (inverted triangles). Nodes are colored by elevation. Arrow points to the general location of the 12 nodes whose data are plotted in Figure 4.9. Black lines denote the two transects for which we numerically model infrasound propagation; shaded boxes indicate the inclusion region for node waveforms. Inset shows an expanded view including the locations of all 23 shots; gray box delineates main map extent and EarthScope Transportable Array infrasound stations F05D and E04D are shown as brown dots. (b) Timeline of shots, with static sound speeds calculated from temperature measurements (see Equation 4.3) at the four weather stations shown in (a) plotted as colored lines. (Vertical position of shot markers is solely for visual clarity.) Times are in UTC. In both (a) and (b), shot markers are sized by the shot charge weight (450 or 900 kg) and colored by the presence (black) or absence (white) of observations of ground-coupled airwaves (GCAs) on the nodes.

infrasound arrival in the resulting STA/LTA-processed shot gathers. These processed shot gathers are shown in Figure 4.2. We use relative STA/LTA values rather than absolute amplitude-based metrics due to the complex nature of acoustic–seismic coupling (see §4.5.2).

To examine the intra-array variability of STA/LTA amplitudes, we define a celerity window $320 \leq C \leq 350$ m/s and find the maximum of the STA/LTA function within that window for each node. We also identify the time corresponding to the maximum and use that as an effective pick time. Finally, using the filtered signals (no STA/LTA processing) we calculate the root-mean-square (RMS) seismic velocity for 20 s windows occurring immediately before the shot time as a measure of pre-event noise.

4.3.2 Topographic ray path analysis

Diffraction is the component of the infrasound wavefield that cannot be explained by geometric acoustics (Pierce, 2019). Diffraction occurs wherever intervening topography obscures the line-of-sight path from source to receiver. In such cases, acoustic wavefronts must propagate over topographic features to reach the receiver. This process results in a loss of energy due to increased spreading and an increase in travel time due to the longer propagation distance (Fee et al., 2021). Diffraction is a significant component of the topographical influence on the infrasound wavefield (K. Kim & Lees, 2011; Lacanna & Ripepe, 2013; Maher et al., 2021).

Fully assessing the impact of topography on the wavefield requires a 3D simulation (e.g., Fee et al., 2021; Lacanna & Ripepe, 2020) which is infeasible here due to the size of our domain and our frequencies of interest, so instead we estimate the effects of diffraction for the entire array using a “shortcut” approach based on the Fresnel number. The Fresnel number, N , quantifies diffraction and is defined as

$$N = \frac{(R_f - R_d)}{\lambda/2}, \quad (4.1)$$

where λ is the wavelength; R_f is the length of the shortest diffracted path over topography, and R_d the length of the direct path (i.e., line-of-sight slant distance), from source to receiver (Maher et al., 2021). Empirically-derived relations between N and the so-called insertion loss — the attenuation caused by the insertion of an obstruction between source and receiver — have been developed (Maekawa, 1968) and evaluated against observations and full 3D numerical simulations (Maher et al., 2021). Here, however, we calculate only the numerator of Equation 4.1 and use this path length difference value as a proxy for the amount of topographic obstruction present in the vertical plane between each shot and each node.

We calculate the direct and shortest diffracted path lengths to obtain the path length difference ($R_f - R_d$) for every shot–node pair. Paths are calculated using the 1 arc-second (~ 30 m) horizontal resolution Shuttle Radar Topography Mission (SRTM) digital elevation model (DEM). The shots and nodes are assumed to be clamped to the topography (i.e., we do not use the field-measured elevations).

4.3.3 Atmospheric data and models

We incorporate data from ground-based meteorological stations as well as mesoscale and global atmospheric models to understand atmospheric propagation effects. We use hourly temperature time series from four Snow Telemetry (SNOTEL) sites located around MSH and within the nodal array (purple inverted triangles in Figure 4.1a).

We use horizontal wind grids from North American Mesoscale Forecast System (NAM) “nest” numerical weather prediction products for the continental United States (2.5 km horizontal resolution). These grids provide wind speed and direction at 10 m above ground level at hourly forecast intervals. The higher resolution of these grids allows them to better resolve topography (Gowan et al., 2018). We note that these are not a reanalysis product.

The NAM weather forecast products provide relatively high horizontal resolution but are not available on pressure levels (i.e., at multiple heights in the atmosphere), which we require as input for the numerical modeling we describe subsequently. Therefore we additionally use

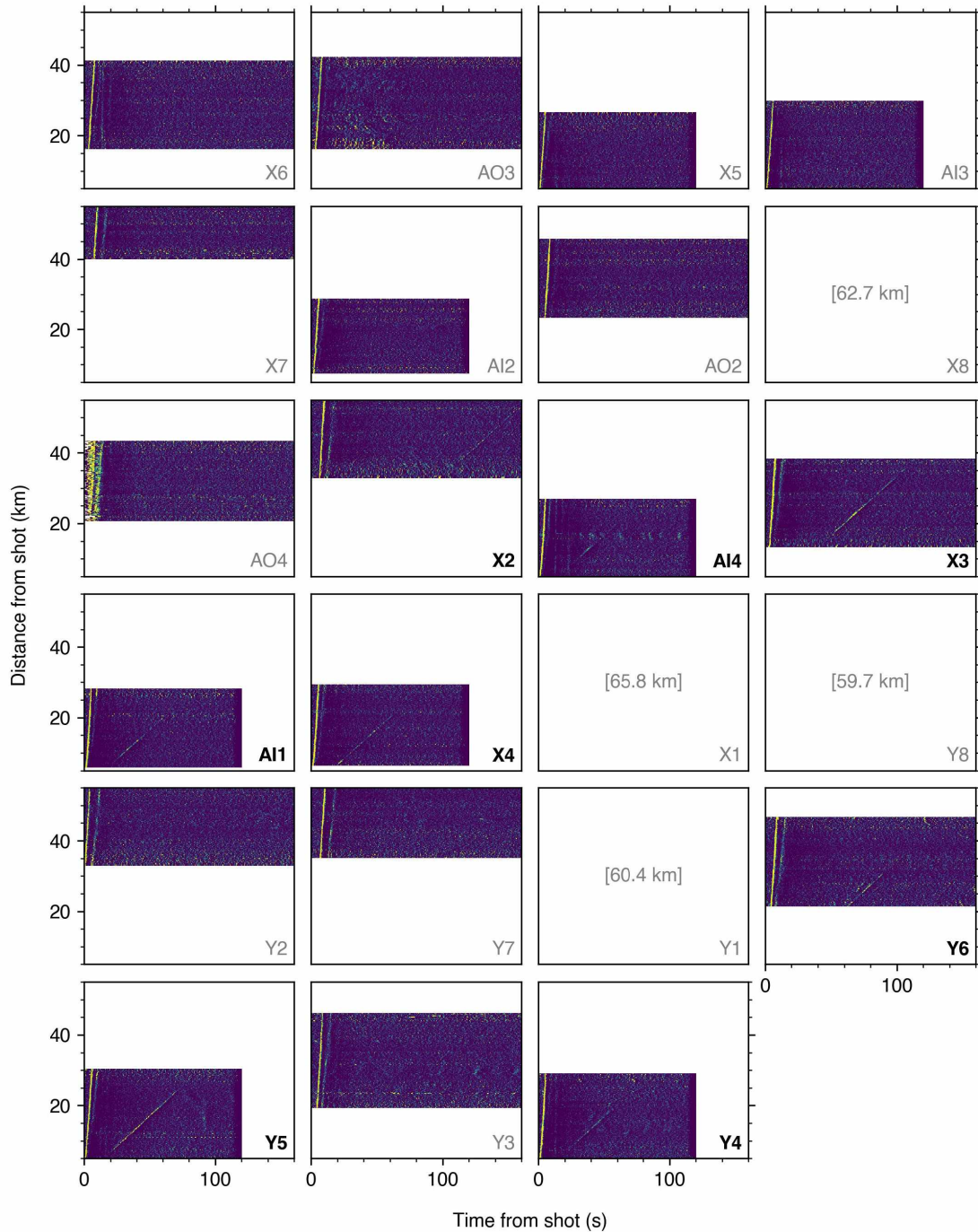


Figure 4.2 Short-term average to long-term average ratio (STA/LTA) shot gathers recorded on the nodal array for the 23 iMUSH shots. Yellow shades indicate larger STA/LTA amplitudes. Shots are arranged chronologically and the shot name is given in the bottom-right corner of each subpanel. Shots with observed coupled arrivals have shot names in boldface. Gathers for shots farther than 55 km from the closest node are not plotted, as none of these shots produced observable coupled arrivals; the distance to the closest node is given in square brackets for these shots.

ERA5 weather forecast reanalysis products from the European Centre for Medium-Range Weather Forecasts. For each shot, we use the spatially nearest 1D profile, at the nearest hour to the shot time. Each profile contains horizontal wind components, geopotential, and temperature on 37 pressure levels (from approximately 100–200 m to 49 km above sea level).

For shot Y5, we process the NAM wind data to produce estimates of the wind’s influence on travel time at each node. We interpolate the wind speed and direction grids onto profiles with 500 m spacing extending from the shot to each node. For each point on the interpolated wind profile, we compute the wind component in the direction of propagation, w_p , which is a scalar given by

$$w_p = \hat{\mathbf{p}} \cdot \mathbf{w}, \quad (4.2)$$

where $\hat{\mathbf{p}}$ is a unit vector pointing from the shot to the node (i.e., the propagation direction) and \mathbf{w} is the wind vector. We then take the median over all w_p in the profile to obtain a single value of the along-propagation wind component for each node.

4.3.4 Numerical modeling of the infrasound wavefield

We use a finite-difference time-domain (FDTD) code to simulate infrasound propagation for 2D transects originating at specific shots and spanning the nodal array. This parallelized code, which was developed outside of this paper (see §4.7), solves 2D linearized, inviscid Euler equations for moving media in a stratified (1D profile) atmosphere. The code interpolates atmospheric profiles and terrain transects onto a Cartesian grid; for these simulations we use a spatial discretization of 2 m. Waves at the edge of the domain are damped with perfectly matched layers. The numerical scheme uses second-order centered differences in the domain interior which switch to one-sided differences on the edge of the domain. Second-order one-sided differences are used on the stair step terrain boundary, which also applies a rigid boundary condition (Pierce, 2019). The equations of motion are solved in time using a standard fourth-order Runge–Kutta method, with a simulation-specific time step of 0.004 s.

We drive our governing equations with a monopole volume source, and a raised-cosine filter source time function with a cutoff frequency of 4 Hz. The cutoff frequency is selected based on spectral analysis of the nearest EarthScope Transportable Array (TA) infrasound stations to the iMUSH shots (see Figure 4.1a inset and Figure 4.10). We do not use the observed spectral content of the coupled arrivals on the nodes to determine the cutoff frequency, because the gain of the acoustic–seismic transfer function often increases with frequency (Matoza & Fee, 2014). This high-pass filter effect would result in an artificially high choice of cutoff frequency. For our chosen spatial discretization and cutoff frequency, we maintain > 30 grid points per wavelength (S. Wang, 1996). We simulate infrasound propagation over two 24-km profiles originating from shots Y5 and X5 (transects are shown on Figure 4.1a). Terrain profiles are interpolated from the same SRTM DEM mentioned in §4.3.2. Atmospheric input variables are taken from the ERA5 model as described in §4.3.3. The atmospheric profiles used in our numerical modeling are plotted in Figure 4.11.

4.4 Results

4.4.1 Presence of acoustic–seismic coupled arrivals on nodes

We observe clear acoustic–seismic coupled arrivals on the nodes for eight of 23 shots (Figure 4.2; Table 4.1). Arrivals are observed at shot–node distances from about 7 km to over 50 km (Figure 4.2), and at a variety of shot–array azimuths (Figure 4.1a). Only one of the larger-yield (900 kg charge weight) shots, X2, produced observed coupled arrivals; this shot was the most distant from the nodal array of all shots with observed coupled arrivals (Figure 4.3; Table 4.1).

No coupled arrivals were observed for any of the shots in the first of the three temporal shot clusters (Figure 4.3; clusters shown in Figure 4.1b). Median RMS seismic velocities for the shots in this first cluster are $> 0.4 \mu\text{m/s}$, while median RMS velocities for all other shots are $\leq 0.2 \mu\text{m/s}$ (Figure 4.3; Table 4.1). There is no temporal pattern associated with coupled arrival presence within the latter two shot clusters (Figure 4.1b).

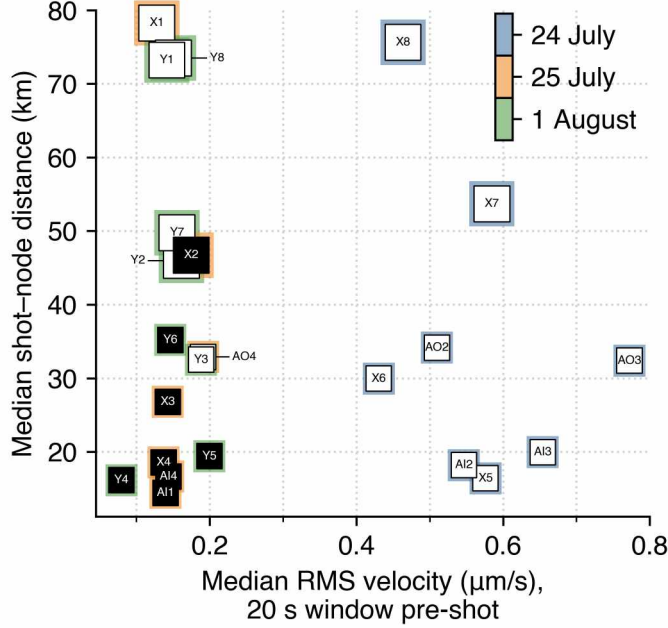


Figure 4.3 Scatter plot of median shot-node distances versus median pre-shot root-mean-square (RMS) seismic velocities for each iMUSH shot. Medians are taken over all of the nodes in the array. Colored borders around each shot marker indicate the day the shot took place (shots occurred in three clusters). Shot markers are colored and sized as in Figure 4.1. See also Table 4.1.

Shot Y5 shows the strongest coupled infrasound arrival (largest STA/LTA amplitudes occurring over the broadest distance range), followed by shot X3. Conversely, shot AI4 shows the weakest coupled infrasound arrival, with lower STA/LTA amplitudes occurring over a narrow distance band. We focus on observations from, and modeling of, a positive example — shot Y5 — and a negative example — shot X5 — in the subsequent portion of this work.

4.4.2 Atmospheric state during the shots

While seismic sensors are generally prone to wind noise (C. W. Johnson et al., 2019), particularly at frequencies of approximately 1 Hz and greater for vertical components (Lott et al., 2017), unburied nodes are especially sensitive to this noise by virtue of their surface exposure (Sweet et al., 2018). The much larger pre-shot RMS noise we observe for the first eight shots suggests that winds were higher during the day of those shots (24 July UTC; all times hereafter in UTC). The NAM wind grid for the shot X5 time confirms the presence

Table 4.1 Summary of acoustic–seismic coupled arrival observations and conditions for each shot, sorted chronologically. Black and gray text indicate shots with and without observed coupled arrivals, respectively. Root-mean-square (RMS) seismic velocities are calculated for 20 s windows pre-shot. Shot coordinates and elevations are available in Table S1 of R. Wang et al. (2020).

Shot	UTC time in 2014 (MM-DD hh:mm:ss)	Weight (kg)	Median RMS velocity ($\mu\text{m/s}$)	Median shot–node distance (km)	Coupled arrivals?
X6	07-24 05:05:00	450	0.43	30.0	False
AO3	07-24 05:10:00	450	0.77	32.4	False
X5	07-24 06:55:00	450	0.58	16.4	False
AI3	07-24 07:10:00	450	0.65	20.0	False
X7	07-24 09:05:00	900	0.58	53.7	False
AI2	07-24 09:40:00	450	0.55	18.2	False
AO2	07-24 11:30:00	450	0.51	34.2	False
X8	07-24 11:35:00	900	0.46	75.6	False
AO4	07-25 05:00:00	450	0.19	32.9	False
X2	07-25 05:35:00	900	0.17	46.7	True
AI4	07-25 07:20:00	450	0.14	16.7	True
X3	07-25 07:35:00	450	0.14	26.8	True
AI1	07-25 08:50:00	450	0.14	14.4	True
X4	07-25 10:10:00	450	0.14	18.6	True
X1	07-25 10:16:00	900	0.13	78.3	False
Y8	08-01 06:00:00	900	0.15	73.5	False
Y2	08-01 06:44:50	900	0.16	46.0	False
Y7	08-01 07:50:00	900	0.16	49.8	False
Y1	08-01 08:25:00	900	0.14	73.2	False
Y6	08-01 09:20:00	450	0.15	35.2	True
Y5	08-01 10:30:00	450	0.20	19.4	True
Y3	08-01 11:35:00	450	0.19	32.5	False
Y4	08-01 12:45:00	450	0.08	16.2	True

of strong winds (1.6–9.0 m/s) during this day of shooting (Figure 4.4a). Conversely, winds are weaker (0.4–5.4 m/s) and less consistent in direction during the time of shot Y5 (Figure 4.4b), although there is generally a northerly (along-path) component to the winds. The wind directions shown in Figure 4.4a are generally representative of the wind state during the shots occurring on 24 July; the wind directions shown in Figure 4.4b are typical of the winds observed during the other shots on 25 July and 1 August.

The static sound speed, c , is proportional to the square root of air temperature:

$$c = \sqrt{\frac{\gamma RT}{M}}, \quad (4.3)$$

where γ is the adiabatic index (about 1.4 for dry air), M is the molar mass (0.02896 kg/mol for dry air), T is air temperature in kelvin, and R is the molar gas constant (Pierce, 2019). Temperature data from the four SNOTEL sites around MSH (Figure 4.1a) show diurnal variations as well as markedly higher temperatures during 1 August, when the final day of shooting occurred. This translates to a significant increase in the static sound speed during this interval — inferred sound speeds are approximately 335–337 m/s during the first two days of shooting, and rise to 340–344 m/s during the last cluster of shots (Figure 4.1b).

4.4.3 *Spatial variability of acoustic–seismic coupled arrival amplitudes*

The observation of strong coupled arrivals across a broad range of shot–node distances for shot Y5 motivates a closer look at the spatial distribution of coupled arrival amplitudes. Coupled arrival STA/LTA amplitudes for each node are obtained as detailed in §4.3.1 and plotted in map view in Figure 4.5a. Clear spatially coherent regions of relatively higher and lower amplitudes are seen. Lower amplitudes are present to the southwest, south, and southeast of the MSH edifice. Larger amplitudes occur to the northwest, north, and northeast of the edifice.

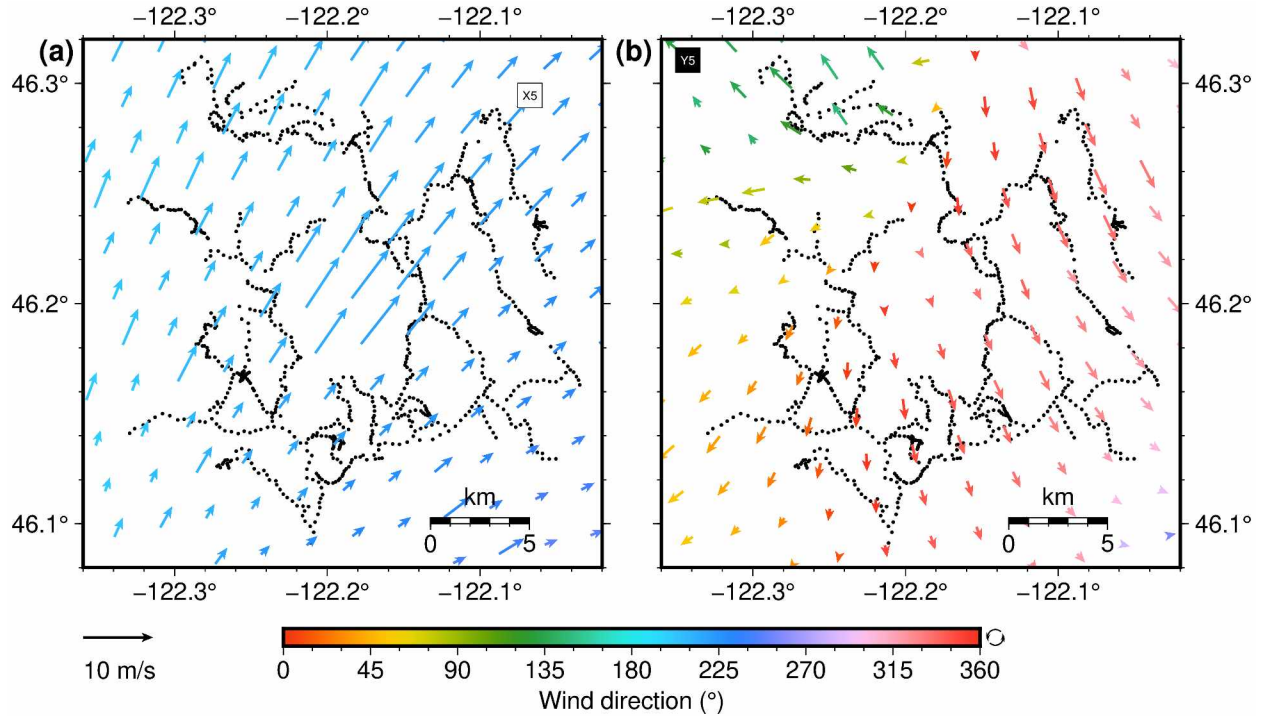


Figure 4.4 Wind speed and direction at 10 m above ground level during (a) shot X5 and (b) shot Y5. Wind data are sourced from North American Mesoscale Forecast System “nest” numerical weather prediction products for 2014-07-24 07:00 UTC (a) and 2014-08-01 11:00 UTC (b), the closest hours to each shot. Nodes are shown as black dots. Shot markers are colored and sized as in Figure 4.1.

STA/LTA amplitudes correlate strongly with topographic features for shot Y5 (Figure 4.5). For example, the line of nodes on the ridge closest to shot Y5 shows large amplitudes, while nodes in the valley lying directly to the south of this ridge have lower amplitudes. Likewise, the ridge extending northeast from the MSH edifice shows larger amplitudes, as does the south-southeast trending ridge furthest to the northeast. The valley in between this ridge and the edifice, conversely, has much lower amplitudes. Amplitudes on the shot-facing portion of the MSH edifice are relatively high, while amplitudes on the side of the edifice opposite the shot are low.

Calculated path length differences for shot Y5 and the nodes are shown in Figure 4.5b. There is a strong spatial correlation between areas of higher STA/LTA amplitude and shorter path length difference, and vice versa. Path length differences range from 13 to 274 m. (For a 2 Hz wave traveling at 340 m/s, the wavelength is 170 m and therefore the Fresnel number

ranges from 0.2 to 3.2.) Observed kilometer-scale features, such as amplitude differences within the intersection of nodes due north of the MSH summit at about $(46.28^\circ, -122.18^\circ)$, and between ridges and valleys, are reflected in the path length differences. In general, with the possible exception of a few groups of nodes located to the west of the MSH edifice, all of the larger-scale coupling trends evident in the observed amplitudes are present in the path length differences.

We note that the 7 km minimum distance quoted in §4.4.1 likely reflects that coupled acoustic arrivals are masked by the seismic surface wave coda for near-shot distances. We can quantify this masking distance d_{mask} via

$$d_{\text{mask}} = t_{\text{coda}} \left(\frac{1}{c} - \frac{1}{v_{\text{P}}} \right)^{-1}, \quad (4.4)$$

where c is the bulk sound speed, v_{P} is the bulk P-wave speed, and t_{coda} is the estimated length of the seismic coda. Using $c = 340$ m/s, $v_{\text{P}} = 5$ km/s (Kiser et al., 2019), and $t_{\text{coda}} = 20$ s (estimated from manual inspection of raw shot gathers), the masking distance is 7.3 km. A higher-frequency passband was tested, which removed the lower-frequency overlapping seismic arrival coda and recovered coupled arrival observations closer to the source. However, distant observations were suppressed as a result of greater attenuation at this high-frequency passband, so we used 5–50 Hz as the best compromise. Nodes within the masking distance are shown as empty circles in Figure 4.5a.

4.4.4 *Travel time variations and azimuth dependence*

A map view of the arrival time picks for shot Y5 is shown in Figure 4.6a. Here we are converting the arrival time picks to a modified “celerity,” where in the numerator we use the shortest diffracted path length, R_{f} in Equation 4.1, instead of horizontal source–receiver distance. This helps account for the effect of topography on the travel time and celerity estimates. Modified celerity values for nodes with STA/LTA amplitudes > 7 range from

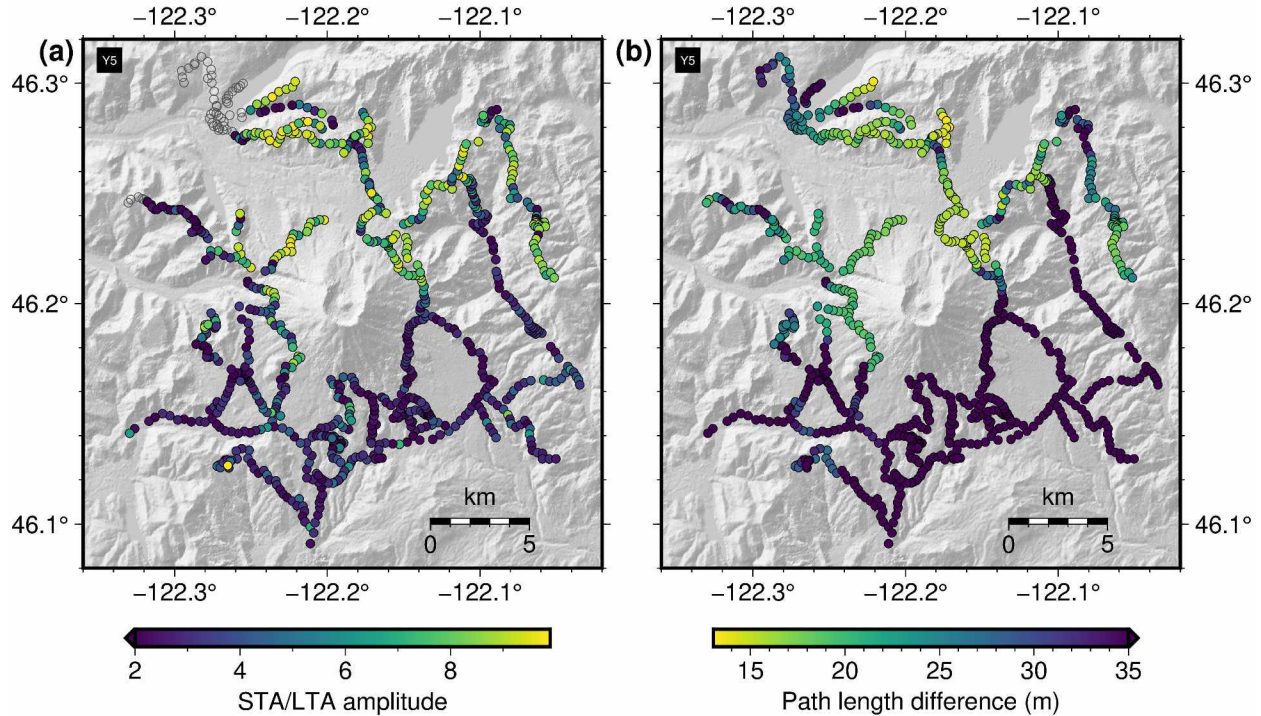


Figure 4.5 Comparison between coupled arrival short-term average to long-term average ratio (STA/LTA) amplitudes **(a)** and differences between direct and shortest diffracted paths **(b)** for shot Y5. Empty circles in **(a)** indicate nodes within the near-source zone where coupled arrivals are masked by the seismic coda (see Equation 4.4). Shot markers are colored and sized as in Figure 4.1.

324–348 m/s, with a median of 340.5 m/s. In Figure 4.6a we have mapped the STA/LTA amplitude to transparency to highlight picks with higher confidence due to stronger arrivals. There is a clear azimuthal dependence in the modified celerity estimates, with nodes to the northern part of the array registering slower celerities than those towards the middle latitudes of the array, on the northern portion of the MSH edifice.

Estimates for the median along-propagation NAM model wind component (w_p ; see Equation 4.2) for each node are plotted in an identical fashion in Figure 4.6b. Median w_p values range from -3.6 to 0.9 m/s. For most nodes, the net effect of the wind field is a reduction in celerity (median $w_p < 0$), with the northwest portion of the array showing the largest reductions (slower arrivals), and consistently smaller reductions (faster arrivals) below about 46.22° latitude. There is broad agreement between the observed travel times (Figure 4.6a) and the model (Figure 4.6b) for regions of slower and faster arrivals.

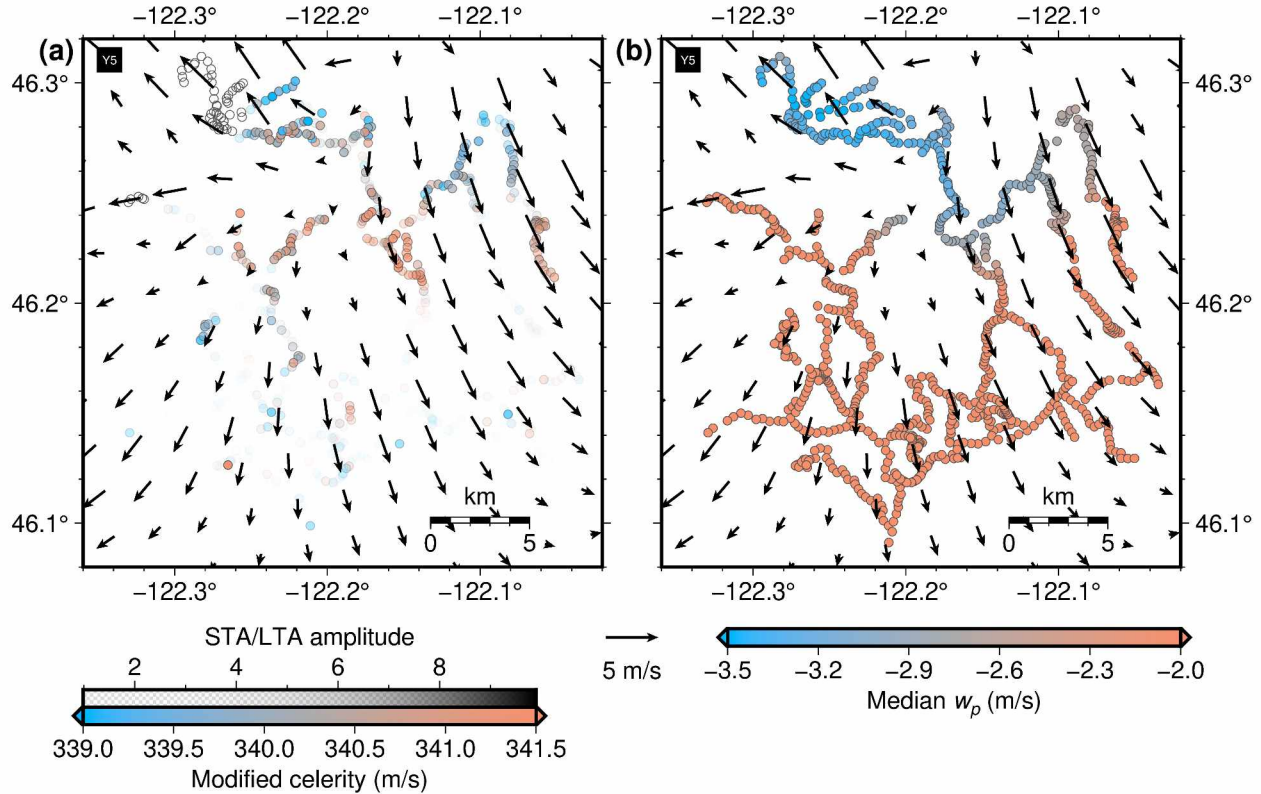


Figure 4.6 Comparison between measured celerities for coupled arrivals and modeled along-path winds for shot Y5. **(a)** Modified celerities (shortest diffracted path divided by measured travel time) for each node. Short-term average to long-term average ratio (STA/LTA) amplitudes are mapped to marker transparency. Empty circles indicate nodes within the near-source zone where coupled arrivals are masked by the seismic coda (see Equation 4.4). **(b)** Median along-path wind component (w_p ; see Equation 4.2) calculated for each node from the North American Mesoscale Forecast System “nest” numerical weather prediction product. Wind vectors are from the same wind field as shown in Figure 4.4b. Shot markers are colored and sized as in Figure 4.1.

4.4.5 Infrasound wavefield simulations

The results of our FDTD propagation modeling for the shot Y5 and shot X5 transects are shown in Figures 4.7a–c and 4.8a–c. Panel (a) displays acoustic wavefield snapshots for each transect at 4 s intervals from 0–5 km in altitude and 0–24 km in range. Each snapshot is normalized by its peak compressional amplitude. Panel (b) shows predicted ground transmission loss along the simulated transect. The transmission loss is the accumulated attenuation relative to a reference distance of 24 m. Panel (c) shows simulated acoustic waveforms at 200

m intervals, with colors indicating predicted amplitude. Both simulations show a complex wavefield produced by interactions with topography. Generally, the simulated waveforms become more complex, and the signal duration lengthens, as distance from the source increases. The shot X5 simulation in particular develops pronounced, lengthened (up to 2 s duration) coda as distance from the source increases.

Waveform amplitudes also generally decay with distance, albeit with some amplitude increases: topography-induced focusing effects are evident in the ground transmission loss and waveforms at numerous locations along each transect. These effects are especially visible in the waveforms at 8–8.5 km, 12–13 km, and 16.5–17 km for the shot Y5 transect (Figure 4.7c) and 5.5–6 km and 7–7.5 km for the shot X5 transect (Figure 4.8c). Diffraction of infrasound around topographic barriers is also clearly visible in the wavefield snapshots, such as near the source at 0.5–1 km in the shot Y5 transect (Figure 4.7a) and 14.5–16 km in the shot X5 transect (Figure 4.8a). Diffraction is associated with lower infrasound amplitudes which are reflected in the wavefield snapshots as well as the colors of the waveforms in Figures 4.7c and 4.8c. We note that for both simulations, the input atmospheric profiles do not suggest that refraction (i.e., propagation in an atmospheric waveguide) would occur (see Figure 4.11b,d). We also note that the trapped energy visible in the shot X5 wavefield snapshots and transmission loss plot at > 17 km range (Figure 4.8a,b) is a simulation artifact related to the tapering of the wind field to zero at the terrain surface; this is not physical.

The simulated waveforms show clear travel time variations related to longer diffracted path lengths over topography. This is especially clear in the shot X5 simulation, where infrasound is traveling almost directly over the summit of MSH (see black line for transect X5 in Figure 4.1a) resulting in large (~ 0.5 s) travel time delays on the side of the edifice opposite the shot (15–24 km in Figure 4.8c). Smaller-scale travel time variations in the vicinity of topographic obstructions are seen for both transects, however, such as the delayed waveforms at 1 km in the shot Y5 transect (Figure 4.7c). Note that we are plotting these

waveforms with reduced time, using the static sound speeds calculated from the MSH weather stations at the time of these two shots (see Figure 4.1b).

Seismic waveforms from nodes within 500 m of each transect (see shaded regions padding the transects in Figure 4.1a) are shown in Figures 4.7d and 4.8d. Colors again indicate relative waveform amplitude. For shot Y5, acoustic wave arrivals are clear at most nodes in the transect, although systematic patterns in waveform characteristics are not apparent. There is no clear amplitude decay with distance from the source, and signal duration does not show any systematic increase with distance. There are a few areas where the topography-induced amplitude variations shown in the synthetics are seen in the observed waveforms. At 12–13 km into the transect — where a topographic dip occurs followed by a steeply rising mound — we see decreasing amplitudes moving along the downward portion of the slope, followed by a larger-amplitude waveform as the slope begins to rise (Figure 4.7d). This may indicate focusing as observed in the synthetic waveforms at this location, but we cannot rule out that this is a coincidence given the large variability in waveform amplitudes along the transect in general. For shot X5, the waveforms are dominated by wind noise, and no clear coupled arrivals are observed.

4.5 Discussion

4.5.1 Factors controlling the presence of coupled signals on nodes

We focus first on the bulk presence or absence of coupled arrivals on the nodes for each shot. The entire first cluster of shots, occurring on 24 July, produced no observed coupled arrivals on the nodal network. This is explained by the high noise levels on the nodes (Figure 4.3) due to consistently high winds (see, e.g., Figure 4.4a) during this day. Nodal data for the remaining shots have RMS noise levels which are consistently below $0.2 \mu\text{m/s}$. Shots X1, Y8, and Y1 are more than 70 km from the nodal array. Infrasound from these shots undergoes greater attenuation due to longer shot–node paths, and therefore coupled arrivals may be below the noise level on the nodes, despite the larger yield of these shots.

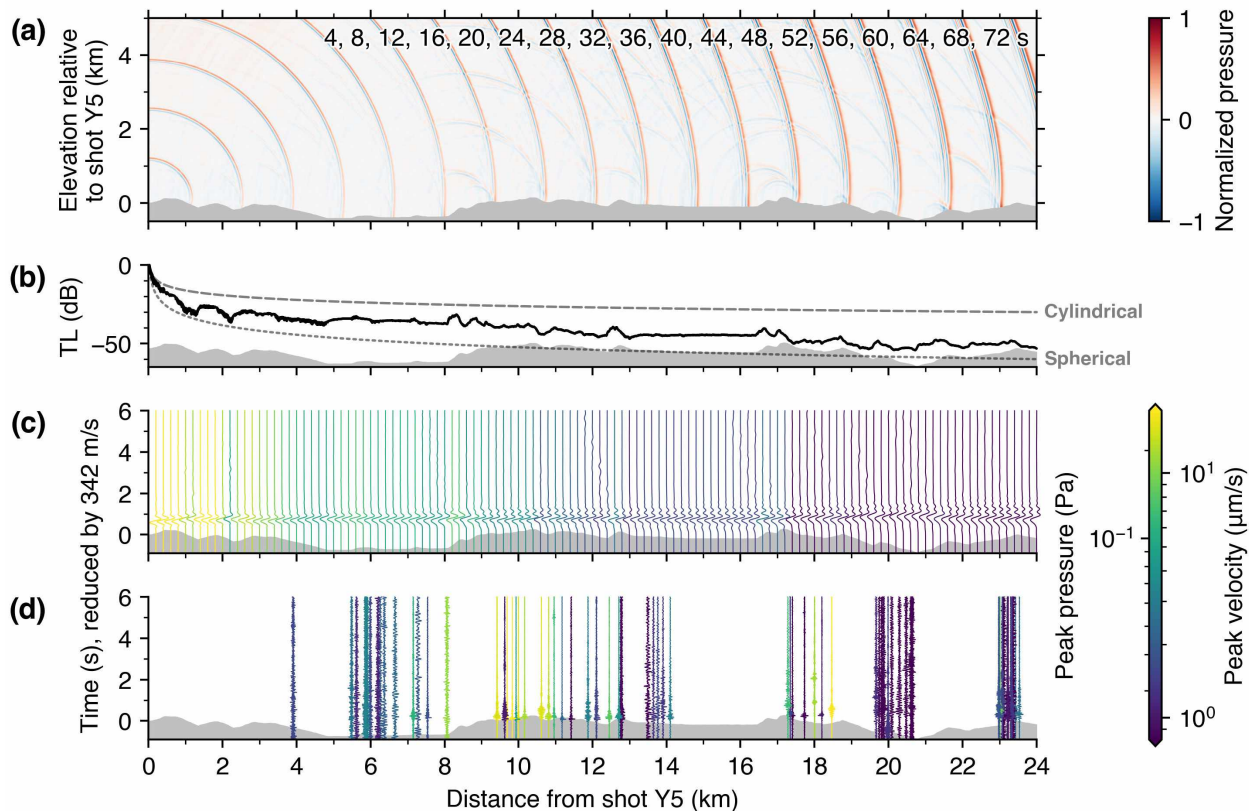


Figure 4.7 Finite-difference time-domain simulation output compared to recorded waveforms on the nodes for the shot Y5 transect. **(a)** Simulated pressure wavefield snapshots at four-second intervals. Each snapshot is individually normalized. Red colors indicate compression; blue colors indicate rarefaction. **(b)** Ground transmission loss (TL) obtained from simulated waveforms. For reference, dashed and dotted lines show predicted geometric attenuation based upon cylindrical and spherical spreading. **(c)** Simulated waveforms from synthetic receivers spaced at 200 m intervals along the topographic surface. Waveforms are individually normalized and colored by their peak pressures. **(d)** Observed seismic waveforms from nodes within 500 m of the simulation transect (see black line and shaded box in Figure 4.1a.). Waveforms are individually normalized and colored by their peak velocities. Note that we are using reduced time for the y -axes in **(c)** and **(d)**. Topography along this transect is shown as a gray shaded region in all subplots.

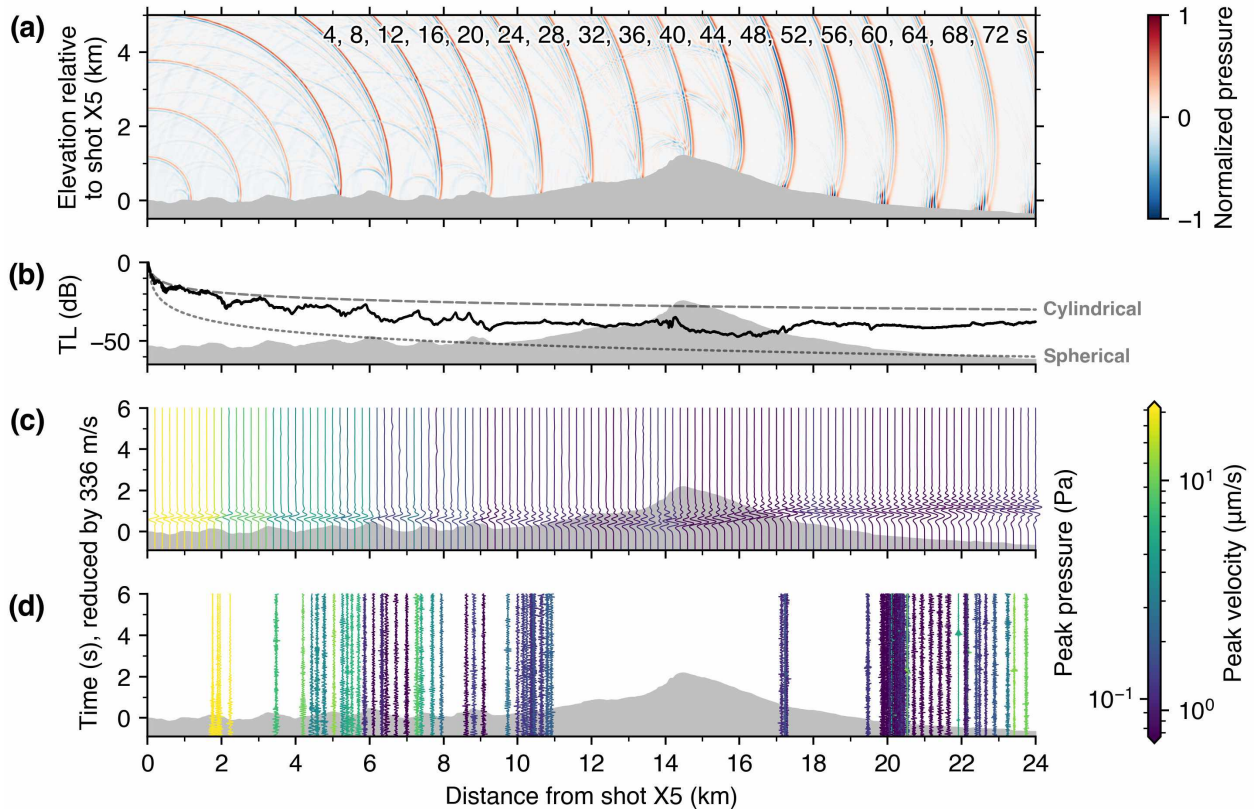


Figure 4.8 Same as Figure 4.7, but for the shot X5 transect.

Shots AO4, Y2, Y7, Y3 are conspicuous in that their noise levels and median shot–node distances are similar to other shots with observed coupled arrivals. We believe that likely non-favorable winds or seismic–acoustic source coupling played a role in the lack of coupled recordings from these shots. However, exploring this in detail is outside of the scope of this work and challenging given 3D atmospheric complexities poorly constrained by the models and limited information about shot source coupling.

We note that we are assuming that iMUSH shots of equal charge weight coupled equal energy into the atmosphere. However, differences in burial depth and near-surface geologic structure and composition can influence seismoacoustic energy partitioning for buried explosions (Ford et al., 2014; Poppeliers et al., 2019). While iMUSH shot burial depths were fairly uniform, we cannot rule out the impact of near-source geology on the degree of seismic–acoustic coupling produced by each shot. For example, in another study examining iMUSH

explosive sources, R. Wang et al. (2020) note that shot X4 generated surface rupture, which may affect seismic–acoustic coupling for this shot.

4.5.2 Spatial coherence of STA/LTA amplitude and path length differences

The strong spatial correlations between observed STA/LTA amplitudes and diffracted path length differences shown in Figure 4.5 demonstrate that infrasound energy loss due to diffraction over topography plays a significant role for the source–receiver distances and topography of this study area. We note that the STA/LTA amplitude measurement is not a direct amplitude measurement; rather, it is sensitive to the relatively impulsive nature of the coupled arrivals and can be considered a proxy for signal-to-noise. Hence, fine-scale differences in STA/LTA amplitude are less reliable than a binary “high versus low” assessment.

We assessed the spatial variability of coupled arrival amplitudes (waveform peak-to-peak values) rather than STA/LTA processed data, and found that the resulting spatial patterns showed more scatter. We believe this to be caused by highly spatially heterogeneous acoustic–seismic coupling throughout the nodal array. In Figure 4.9 we show seismic waveforms and spectrograms, windowed around clear coupled arrivals from shot X4, for 12 nodes spaced within approximately 900 m (see arrow in Figure 4.1a for general location). The peak-to-peak amplitudes of stations spaced within an infrasound wavelength (170 m, e.g., for a 2 Hz wave traveling at 340 m/s) can be larger than a factor of four different from one another — compare, for example, nodes 4304 and 4305 in Figure 4.9. Figure 4.9 additionally highlights that frequency content can vary drastically between adjacent nodes. For example, node 4303 has a peak frequency of ~ 35 Hz, while neighboring node 4308 has a peak frequency of ~ 25 Hz. Waveform durations can also vary on small spatial scales — for example, see the waveforms shown in Figure 4.7d at 10–12 km and 18–19 km ranges. Collectively, these observations are consistent with growing evidence for complexities in acoustic–seismic coupling (e.g., Fee et al., 2016; Langston, 2004; Wills et al., 2022), and they suggest that caution should be

exercised in using acoustic–seismic coupled arrivals within seismic data to infer acoustic amplitude-, frequency-, and signal-duration-based information.

While the simple diffraction analysis we perform appears to capture a large component of the topographic effect on waveform amplitudes, it is important to note the limitations of this simplification. Maher et al. (2021) point out that the insertion loss derived from diffracted path analysis can underestimate infrasound amplitudes because it does not account for energy focusing. Focusing can be significant for extreme topography (e.g., Lacanna & Ripepe, 2020). Furthermore, our diffraction analysis is frequency-independent as we compute only the numerator of Equation 4.1. In reality, different frequencies of the wavefield will diffract different amounts. The full-wave modeling we perform accounts for these frequency-dependent effects.

By examining individual source–receiver paths, our path length difference analysis also assumes that all diffraction occurs in the vertical plane containing source and receiver. In reality, out-of-plane effects from topography can further modulate infrasound amplitudes (Blom, 2020). We note that our FDTD modeling is also limited to 2D transects, but it does include finite-frequency effects such as focusing and scattering, as well as atmospheric state. However, one benefit of the diffracted path analysis is that we can simulate paths for all ~ 900 nodes in our analysis relatively quickly; running a FDTD simulation transect for each shot–node path would take hundreds of hours on our computing infrastructure.

4.5.3 Factors influencing infrasound travel times

Examining travel time measurements on the nodes is appealing because we can avoid reckoning with an unknown, presumably highly-heterogeneous acoustic–seismic transfer function. The density of travel time measurements shown in Figure 4.6a invites a closer look at the spatial variation of propagation effects that can cause the observed differences in travel time. We attribute the spatial patterns in Figure 4.6a exclusively to local-scale atmospheric spatial

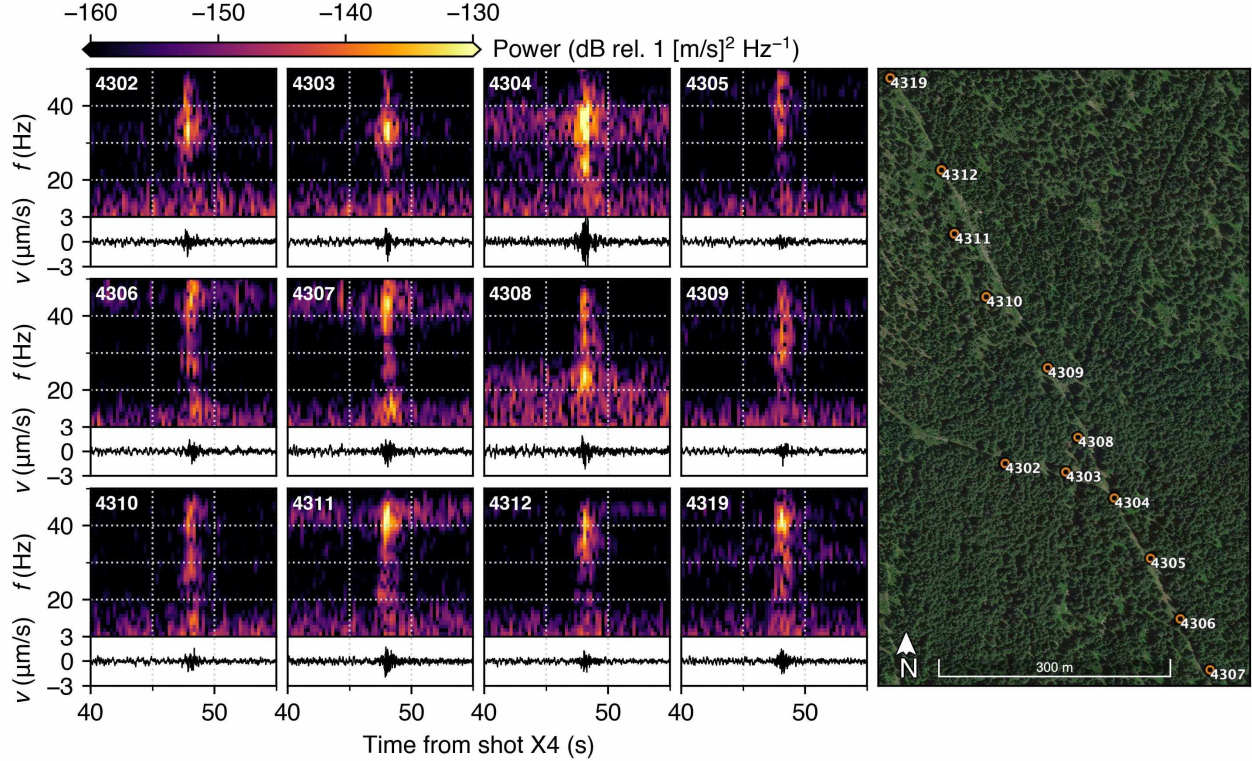


Figure 4.9 Waveforms and spectrograms for coupled arrivals from shot X4 observed on 12 closely-spaced nodes (see arrow in Figure 4.1a for general location). Warmer colors indicate larger signal power. The node ID is in the top-left corner of each spectrogram. All axis and colormap scaling is identical. v = ground velocity; f = frequency. The map shows the locations of these 12 nodes. Background image is from July 2014; © Google Earth.

variability, as we are plotting a modified celerity which incorporates the shortest diffracted path over topography.

The two atmospheric parameters having the strongest influence on travel times are the static sound speed (Equation 4.3), which is governed by temperature, and the horizontal wind speed and direction (Lacanna et al., 2014). In Figure 4.6b we show the modeled impact of the latter of these two parameters, summarized as the median of w_p along each shot node path. Median w_p captures the net upwind and downwind propagation of infrasound and can be considered as the impact of advection on the wavefield.

The observed travel times for shot Y5 are slower than the median w_p advection modeling predicts for the southern half of the array (below about 46.2° latitude in Figure 4.6). This

inconsistency could be due to micro-scale effects not captured in the NAM mesoscale model. All shots took place at night, local time, suggesting the presence of nocturnal boundary layers in the valleys and broad plains surrounding MSH. Such boundary layers have cooler temperatures, resulting in slower travel times and more efficient propagation due to waveguide formation (Keith Wilson et al., 2003). We also note that the NAM winds we use are only available at a single vertical level; winds at height may not reflect those at 10 m above ground level and could produce a different net effect on travel times. Furthermore, we have limited high-amplitude coupled measurements in the southern half of the array, so the slower observed arrivals may just represent scatter in these more limited travel time measurements.

4.5.4 Propagation at intermediate source–receiver distances

Modeling infrasound propagation at intermediate source–receiver distances (15–50 km), where both atmospheric and topographic effects are important, remains a significant challenge. Our analyses, particularly Figures 4.5 and 4.6, clearly show that at the distances specific to the iMUSH active-source experiment (2–90 km), neither of these effects can be ignored. Complete modeling of the seismoacoustic wavefield for iMUSH would require a code which incorporates topography, atmospheric state, and seismic–acoustic and acoustic–seismic coupling.

The current cutting-edge approach to full-wave acoustic propagation modeling involves numerical simulations to directly solve the wave equation on 2D or 3D grids over topography, as done in this work. However, such simulations become prohibitively computationally costly for larger domains and higher source frequencies. This is the case even for situations where extensive computational resources are available, such as in K. Kim and Pasyanos (2022) where the source frequency was limited to below 0.9 Hz despite the presence of higher-frequency energy. 2D simulations are much less costly than 3D simulations, but they cannot capture potentially important effects of variable crosswinds and wavefront interaction with out-of-plane topography (Blom, 2020). Figure 4.4 shows significant crosswinds which would

advect sound into or out of a given 2D plane. We note that simplified and more efficient propagation models, such as geometric ray tracing, would not predict arrivals on the nodes given the wind and temperature profiles from the spatially coarse ERA5 model (Figure 4.11). Finite-frequency effects, which are not captured by geometric methods, should be considered for propagation at these source–receiver distances.

In this work, we model infrasound propagation over topography via a “shortcut” method using diffracted path analysis (see §4.3.2) as well as a full numerical scheme (see §4.3.4). The diffracted path analysis captures the general effects of diffraction on infrasound amplitudes quite well (Figure 4.5). Important diffraction effects such as the far-field impact of near-source topography on infrasound amplitudes, which have been noted in previous modeling work such as Matoza et al. (2009) and Lacanna et al. (2014) (as well as in our FDTD simulations; see, e.g., the first few wavefield snapshots in Figure 4.7a), should theoretically be included in the diffracted path analysis. Numerical simulations capture additional physics not included in our frequency-independent diffracted path analysis such as focusing and scattering. For example, the ground transmission loss predicted by our simulations shows marked increases at shot-facing topographic rises, indicating strong focusing (Figures 4.7b and 4.8b). Still, at intermediate source–receiver distances, diffracted path analysis represents a computationally efficient way to estimate topographic impact without the need for computationally costly simulations within these relatively large domains (Ishii et al., 2020).

Incorporating atmospheric effects in infrasound modeling is difficult because atmospheric models represent only one realization of parameter estimates. Additionally, the spatiotemporal resolution of available products is often lower than necessary. One approach to accounting for uncertainty in global-scale atmospheric models is to realistically perturb individual profiles and run simulations using the perturbed parameters (Hupe et al., 2019; K. Kim & Pasyanos, 2022; Perttu et al., 2020; Smets et al., 2015; Witsil et al., 2022). However, on smaller spatial scales — such as the domain we consider in this work — higher-spatial-resolution models are required. These mesoscale models face similar limitations in that they

represent only one realization of atmospheric state. Their higher spatial resolution and inclusion of orographic effects makes them potentially more useful, but integration of these models into existing propagation modeling codes is difficult and currently unavailable. We also note that access to archived model output is inconsistent and not well-documented, since these are primarily weather forecast products used in the short-term.

The fact that our observations are coupled acoustic–seismic waveforms on seismometers complicates comparison with model outputs. Translating modeled pressure waveforms to seismic waveforms requires the specification of an acoustic–seismic transfer function. If co-located infrasound sensors existed within the nodal array, we could use these to infer a transfer function. However, this function is presumably so spatially heterogeneous that a bulk or averaged transfer function would not successfully reproduce our observed waveforms. Adding additional co-located infrasound sensors would better capture the transfer function, but this defeats the purpose of leveraging a nodal seismic array. Previous work has modeled coupled seismoacoustic wave propagation (Bishop et al., 2022; Matoza et al., 2009); however, neither of these models include the laterally varying and layered material properties needed to capture the variation in coupling. It is unclear how these properties would be measured or specified with spatial resolution fine enough to warrant inclusion in infrasound modeling. This makes modeling acoustic-to-seismic coupling in real-world environments and domain sizes nearly impossible with currently available geologic information.

4.5.5 Applications

Unknown acoustic–seismic transfer functions pose a large challenge when working with coupled signal amplitudes (Hedlin et al., 2010). Considerable research is needed to accurately constrain acoustic–seismic coupling and how it varies even on small spatial scales. Experiments with numerous co-located seismic and acoustic sensors, as well as constraints on shallow subsurface structure, may help illuminate acoustic–seismic coupling (e.g., Novoselov et al., 2020). This work shows that the frequency and amplitude of coupled arrivals can vary

on spatial scales less than the infrasound wavelength (Figure 4.9). Therefore, time-based analyses are likely to be more robust and useful than amplitude-based methods for leveraging existing and future nodal seismic array data. Here we outline a handful of time-based methods for which coupled arrivals on dense seismic arrays may be useful.

In this work, we use known, impulsive sources to study infrasound propagation on a nodal seismic array. An emerging field of study focuses on using known infrasound sources to invert for atmospheric parameters (Assink et al., 2014; Drob et al., 2010). Passive sources such as the microbarom (e.g., Haney, 2009) and local noise from water features (Ortiz et al., 2021) have been used to retrieve time-varying gross ambient air temperatures and winds. Active sources have been used for coda wave analysis to recover air temperature ratios between explosion pairs (Marcillo et al., 2014), and for travel time tomography at the micro-scale (200 m) to obtain temperature and wind fields (Keith Wilson & Thomson, 1994). In theory, one could leverage the density of stations present in the iMUSH or another seismic array to obtain many propagation paths for travel time tomography. We foresee that active sources would be required to couple enough energy into the ground at the nodes to produce detectable arrivals. While pursuing travel time tomography for the iMUSH dataset is beyond the scope of this paper, we note that Figure 4.6 demonstrates that measurable spatial travel time differences exist.

Though examining the seismoacoustic source was not a focus of this work, source characterization is another area where nodal seismic arrays have demonstrable potential. Meng and Ben-Zion (2018) used a dense seismic array in the California desert to track individual aircraft via their spectral signature (i.e., Doppler shift) and signal distribution across the approximately 600×600 m array. Studies have backprojected acoustic–seismic coupled arrivals to locate surficial or aerial sources (Fee et al., 2021; Walker et al., 2010). An advantage of backprojection is that highly processed (e.g., enveloped, smoothed) waveforms are easily incorporated — minimizing possible lack of coherence between coupled signals recorded at sites with differing acoustic–seismic transfer functions. Array processing may be performed with

coupled arrivals on seismic data (e.g., de Groot-Hedlin & Hedlin, 2019). Here, the spacing of seismometers in a dense array may be within the correlation length of infrasound. However, even at these close inter-station distances, coupled arrivals may not be phase coherent, as discussed in Fee et al. (2016) and shown in Figure 4.9 for this study area.

4.6 Conclusions

In this work we examine acoustic–seismic coupled arrivals from buried explosions on a dense nodal seismic array of ~ 900 sensors. The goal was to use this large- N seismic array as a proxy for a large- N infrasound network, as we currently do not have infrasound deployments with this spatial density or quantity of sensors. The “intermediate” spatial domain of this experiment is notable in that neither topographic nor atmospheric effects may be ignored. The presence of coupled arrivals on the nodes for a given explosion appears to be largely controlled by the distance of the shot from the nodal network as well as wind-induced background noise. For select shots, we examine spatial patterns in infrasound propagation in detail and find that both topographic and atmospheric effects are visible in measured amplitudes and travel times and that these can be explained by simple modeling. Our initial modeling consists of predicting diffracted paths over topography and travel time deviations derived from high-resolution 2D atmospheric models. We also compare our observations with numerical models for infrasound propagation which incorporate topography and 1D atmospheric profiles. The models predict notable acoustic waveform variability related to topography, but we find that comparing this result with our observations is hindered by the unknown and highly spatially variable acoustic–seismic transfer function across the nodal array. Additional research is required to better understand acoustic–seismic coupling. The methods we develop here, including the use of mesoscale atmospheric models, may be applied to other nodal seismic and infrasound datasets. Advances in self-contained sensor technology motivate the eventual deployment of large- N infrasound networks to further probe the propagation effects relevant at the scales we investigate here.

4.7 Data Availability Statement

Nodal seismic data from the iMUSH experiment are available through the IRIS Data Management Center as network code 1D (Schmandt, 2014). TA data are available from the same location as network code TA (IRIS Transportable Array, 2003). Temperature data from the four SNOTEL sites (stations MRBW1, SHPW1, SPTWL, SWCW1) are available at <https://download.synopticdata.com>. The NAM weather models are available in the archive at <https://mtarchive.geol.iastate.edu> (full paths to files used are provided in our code repository).

The Python code written to perform this work is publicly available under an MIT license on GitHub at <https://github.com/liamtoney/nodal>. Access to the FDTD propagation code used in this work is available by contacting Jordan W. Bishop (jwbishop@lanl.gov). The Python seismological framework *ObsPy* (Beyreuther et al., 2010) was used extensively in this work. We used *infresnel* (v0.1.0; Toney, 2022) to calculate direct and diffracted paths for our propagation analysis. The spectra in Figure 4.10e were produced using *multitaper* (Prieto, 2022). Figures were made with *PyGMT* (v0.7.0; Uieda et al., 2022; Wessel et al., 2019) and *Matplotlib* (Hunter, 2007).

The supplemental material (see §4.10) contains supporting Figures 4.10 and 4.11.

4.8 Acknowledgments

This work benefited from a discussion with Mie Ichihara. We thank National Weather Service meteorologist Jonathan Chriest for helpful guidance on weather model output selection and access.

This work was supported by the Nuclear Arms Control Technology (NACT) program at the Defense Threat Reduction Agency (DTRA) through contract HDTRA121C0030. Approved for public release; distribution is unlimited.

4.9 References

- Allen, R. V. (1978). Automatic earthquake recognition and timing from single traces. *Bulletin of the Seismological Society of America*, *68*(5), 1521–1532. <https://doi.org/10.1785/BSSA0680051521>
- Allstadt, K. E., Matoza, R. S., Lockhart, A. B., Moran, S. C., Caplan-Auerbach, J., Haney, M. M., Thelen, W. A., & Malone, S. D. (2018). Seismic and acoustic signatures of surficial mass movements at volcanoes. *Journal of Volcanology and Geothermal Research*, *364*, 76–106. <https://doi.org/10.1016/j.jvolgeores.2018.09.007>
- Arrowsmith, S. J., Johnson, J. B., Drob, D. P., & Hedlin, M. A. H. (2010). The seismoacoustic wavefield: A new paradigm in studying geophysical phenomena. *Reviews of Geophysics*, *48*(4), RG4003. <https://doi.org/10.1029/2010RG000335>
- Assink, J. D., Pichon, A. L., Blanc, E., Kallel, M., & Khemiri, L. (2014). Evaluation of wind and temperature profiles from ECMWF analysis on two hemispheres using volcanic infrasound. *Journal of Geophysical Research: Atmospheres*, *119*(14), 8659–8683. <https://doi.org/10.1002/2014JD021632>
- Averbuch, G., Assink, J. D., & Evers, L. G. (2020). Long-range atmospheric infrasound propagation from subsurface sources. *The Journal of the Acoustical Society of America*, *147*(2), 1264–1274. <https://doi.org/10.1121/10.0000792>
- Beyreuther, M., Barsch, R., Krischer, L., Megies, T., Behr, Y., & Wassermann, J. (2010). ObsPy: A Python toolbox for seismology. *Seismological Research Letters*, *81*(3), 530–533. <https://doi.org/10.1785/gssrl.81.3.530>
- Bishop, J. W., Fee, D., Modrak, R., Tape, C., & Kim, K. (2022). Spectral Element Modeling of Acoustic to Seismic Coupling Over Topography. *Journal of Geophysical Research: Solid Earth*, *127*(1). <https://doi.org/10.1029/2021JB023142>
- Blom, P. (2020). The influence of irregular terrain on infrasonic propagation in the troposphere. *The Journal of the Acoustical Society of America*, *148*(4), 1984–1997. <https://doi.org/10.1121/10.0002128>
- Campus, P., & Christie, D. R. (2010). Worldwide Observations of Infrasonic Waves. In A. Le Pichon, E. Blanc, & A. Hauchecorne (Eds.), *Infrasound monitoring for atmospheric studies* (pp. 185–234). Dordrecht: Springer Netherlands. https://doi.org/10.1007/978-1-4020-9508-5_6
- Ceranna, L., Le Pichon, A., Green, D. N., & Mialle, P. (2009). The Buncefield explosion: a benchmark for infrasound analysis across Central Europe. *Geophysical Journal International*, *177*(2), 491–508. <https://doi.org/10.1111/j.1365-246X.2008.03998.x>

- Che, I.-Y., Kim, K., Le Pichon, A., Park, J., Arrowsmith, S., & Stump, B. (2021). Illuminating the North Korean nuclear explosion test in 2017 using remote infrasound observations. *Geophysical Journal International*, *228*(1), 308–315. <https://doi.org/10.1093/gji/ggab338>
- Dean, T., Tulett, J., & Barnwell, R. (2018). Nodal land seismic acquisition: The next generation. *First Break*, *36*(1), 47–52. <https://doi.org/10.3997/1365-2397.n0061>
- de Groot-Hedlin, C., & Hedlin, M. (2019). Detection of Infrasound Signals and Sources Using a Dense Seismic Network. In A. Le Pichon, E. Blanc, & A. Hauchecorne (Eds.), *Infrasound monitoring for atmospheric studies* (pp. 669–700). Cham: Springer International Publishing. https://doi.org/10.1007/978-3-319-75140-5_21
- Drob, D. P., Meier, R. R., Picone, J. M., & Garcés, M. M. (2010). Inversion of Infrasound Signals for Passive Atmospheric Remote Sensing. In A. Le Pichon, E. Blanc, & A. Hauchecorne (Eds.), *Infrasound monitoring for atmospheric studies* (pp. 701–731). Dordrecht: Springer Netherlands. https://doi.org/10.1007/978-1-4020-9508-5_24
- Fee, D., Haney, M., Matoza, R., Szuberla, C., Lyons, J., & Waythomas, C. (2016). Seismic Envelope-Based Detection and Location of Ground-Coupled Airwaves from Volcanoes in Alaska. *Bulletin of the Seismological Society of America*, *106*(3), 1024–1035. <https://doi.org/10.1785/0120150244>
- Fee, D., Macpherson, K., & Gabrielson, T. (2023). Characterizing Infrasound Station Frequency Response Using Large Earthquakes and Colocated Seismometers. *Bulletin of the Seismological Society of America*, 1–15. <https://doi.org/10.1785/0120220226>
- Fee, D., & Matoza, R. S. (2013). An overview of volcano infrasound: From hawaiian to plinian, local to global. *Journal of Volcanology and Geothermal Research*, *249*(3), 123–139. <https://doi.org/10.1016/j.jvolgeores.2012.09.002>
- Fee, D., Toney, L., Kim, K., Sanderson, R. W., Iezzi, A. M., Matoza, R. S., De Angelis, S., Jolly, A. D., Lyons, J. J., & Haney, M. M. (2021). Local Explosion Detection and Infrasound Localization by Reverse Time Migration Using 3-D Finite-Difference Wave Propagation. *Frontiers in Earth Science*, *9*, Article 620813. <https://doi.org/10.3389/feart.2021.620813>
- Ford, S. R., Rodgers, A. J., Xu, H., Templeton, D. C., Harben, P., Foxall, W., & Reinke, R. E. (2014). Partitioning of Seismoacoustic Energy and Estimation of Yield and Height-of-Burst/Depth-of-Burial for Near-Surface Explosions. *Bulletin of the Seismological Society of America*, *104*(2), 608–623. <https://doi.org/10.1785/0120130130>

- Gowan, T. M., Steenburgh, W. J., & Schwartz, C. S. (2018). Validation of Mountain Precipitation Forecasts from the Convection-Permitting NCAR Ensemble and Operational Forecast Systems over the Western United States. *Weather and Forecasting*, *33*(3), 739–765. <https://doi.org/10.1175/WAF-D-17-0144.1>
- Haney, M. M. (2009). Infrasonic ambient noise interferometry from correlations of microbaroms. *Geophysical Research Letters*, *36*(19), L19808. <https://doi.org/10.1029/2009GL040179>
- Hansen, S. M., & Schmandt, B. (2015). Automated detection and location of microseismicity at Mount St. Helens with a large-N geophone array. *Geophysical Research Letters*, *42*(18), 7390–7397. <https://doi.org/10.1002/2015GL064848>
- Hedlin, M. A. H., Drob, D., Walker, K., & de Groot-Hedlin, C. (2010). A study of acoustic propagation from a large bolide in the atmosphere with a dense seismic network. *Journal of Geophysical Research*, *115*(B11), B11312. <https://doi.org/10.1029/2010JB007669>
- Hedlin, M. A. H., Garces, M., Bass, H., Hayward, C., Herrin, G., Olson, J., & Wilson, C. (2002). Listening to the secret sounds of Earth’s atmosphere. *Eos, Transactions American Geophysical Union*, *83*(48), 557. <https://doi.org/10.1029/2002EO000383>
- Hunter, J. D. (2007). Matplotlib: A 2D graphics environment. *Computing in Science & Engineering*, *9*(3), 90–95. <https://doi.org/10.1109/MCSE.2007.55>
- Hupe, P., Ceranna, L., Pilger, C., De Carlo, M., Le Pichon, A., Kaifler, B., & Rapp, M. (2019). Assessing middle atmosphere weather models using infrasound detections from microbaroms. *Geophysical Journal International*, *216*(3), 1761–1767. <https://doi.org/10.1093/gji/ggy520>
- Iezzi, A. M., Schwaiger, H. F., Fee, D., & Haney, M. M. (2019). Application of an updated atmospheric model to explore volcano infrasound propagation and detection in Alaska. *Journal of Volcanology and Geothermal Research*, *371*, 192–205. <https://doi.org/10.1016/j.jvolgeores.2018.03.009>
- IRIS Transportable Array. (2003). *USArray Transportable Array*. International Federation of Digital Seismograph Networks. <https://doi.org/10.7914/SN/TA>
- Ishii, K., Yokoo, A., Iguchi, M., & Fujita, E. (2020). Utilizing the solution of sound diffraction by a thin screen to evaluate infrasound waves attenuated around volcano topography. *Journal of Volcanology and Geothermal Research*, *402*, 106983. <https://doi.org/10.1016/j.jvolgeores.2020.106983>

- Johnson, C. W., Meng, H., Vernon, F., & Ben-Zion, Y. (2019). Characteristics of Ground Motion Generated by Wind Interaction With Trees, Structures, and Other Surface Obstacles. *Journal of Geophysical Research: Solid Earth*, *124*(8), 8519–8539. <https://doi.org/10.1029/2018JB017151>
- Johnson, J., Mikesell, T. D., Anderson, J. F., & Liberty, L. M. (2020). Mapping the sources of proximal earthquake infrasound. *Geophysical Research Letters*, 0–3. <https://doi.org/10.1029/2020GL091421>
- Johnson, J. B., & Ripepe, M. (2011). Volcano infrasound: A review. *Journal of Volcanology and Geothermal Research*, *206*(3-4), 61–69. <https://doi.org/10.1016/j.jvolgeores.2011.06.006>
- Karplus, M., & Schmandt, B. (2018). Preface to the Focus Section on Geophone Array Seismology. *Seismological Research Letters*, *89*(5), 1597–1600. <https://doi.org/10.1785/0220180212>
- Keith Wilson, D., Noble, J. M., & Coleman, M. A. (2003). Sound Propagation in the Nocturnal Boundary Layer. *Journal of the Atmospheric Sciences*, *60*(20), 2473–2486. [https://doi.org/10.1175/1520-0469\(2003\)060;2473:SPITNB;2.0.CO;2](https://doi.org/10.1175/1520-0469(2003)060;2473:SPITNB;2.0.CO;2)
- Keith Wilson, D., & Thomson, D. W. (1994). Acoustic Tomographic Monitoring of the Atmospheric Surface Layer. *Journal of Atmospheric and Oceanic Technology*, *11*(3), 751–769. [https://doi.org/10.1175/1520-0426\(1994\)011;0751:ATMOTA;2.0.CO;2](https://doi.org/10.1175/1520-0426(1994)011;0751:ATMOTA;2.0.CO;2)
- Kim, K., & Lees, J. M. (2011). Finite-difference time-domain modeling of transient infrasonic wavefields excited by volcanic explosions. *Geophysical Research Letters*, *38*(6), n/a-n/a. <https://doi.org/10.1029/2010GL046615>
- Kim, K., & Pasyanos, M. E. (2022). Yield Estimation of the August 2020 Beirut Explosion by Using Physics-Based Propagation Simulations of Regional Infrasound. *Geophysical Research Letters*, *49*(23), 1–9. <https://doi.org/10.1029/2022GL101118>
- Kim, K., & Rodgers, A. (2017). Influence of low-altitude meteorological conditions on local infrasound propagation investigated by 3-D full-waveform modeling. *Geophysical Journal International*, *210*(2), 1252–1263. <https://doi.org/10.1093/gji/ggx218>
- Kim, T. S. (2004). Local infrasound signals from the Tokachi-Oki earthquake. *Geophysical Research Letters*, *31*(20), L20605. <https://doi.org/10.1029/2004GL021178>
- Kiser, E., Levander, A., Zelt, C., Schmandt, B., & Hansen, S. (2019). Upper Crustal Structure and Magmatism in Southwest Washington: V_p , V_s , and V_p/V_s Results From the iMUSH Active-Source Seismic Experiment. *Journal of Geophysical Research: Solid Earth*, *124*(7), 7067–7080. <https://doi.org/10.1029/2018JB016203>

- Kogelnig, A., Hübl, J., Suriñach, E., Vilajosana, I., & McArdell, B. W. (2014). Infrasound produced by debris flow: Propagation and frequency content evolution. *Natural Hazards*, *70*(3), 1713–1733. <https://doi.org/10.1007/s11069-011-9741-8>
- Lacanna, G., Ichihara, M., Iwakuni, M., Takeo, M., Iguchi, M., & Ripepe, M. (2014). Influence of atmospheric structure and topography on infrasonic wave propagation. *Journal of Geophysical Research: Solid Earth*, *119*(4), 2988–3005. <https://doi.org/10.1002/2013JB010827>
- Lacanna, G., & Ripepe, M. (2013). Influence of near-source volcano topography on the acoustic wavefield and implication for source modeling. *Journal of Volcanology and Geothermal Research*, *250*, 9–18. <https://doi.org/10.1016/j.jvolgeores.2012.10.005>
- Lacanna, G., & Ripepe, M. (2020). Modeling the Acoustic Flux Inside the Magmatic Conduit by 3D-FDTD Simulation. *Journal of Geophysical Research: Solid Earth*, *125*(6), 1–18. <https://doi.org/10.1029/2019JB018849>
- Langston, C. A. (2004). Seismic ground motions from a bolide shock wave. *Journal of Geophysical Research*, *109*(B12), B12309. <https://doi.org/10.1029/2004JB003167>
- Lott, F. F., Ritter, J. R. R., Al-Qaryouti, M., & Corsmeier, U. (2017). On the Analysis of Wind-Induced Noise in Seismological Recordings. *Pure and Applied Geophysics*, *174*(3), 1453–1470. <https://doi.org/10.1007/s00024-017-1477-2>
- Macpherson, K. A., Fee, D., Coffey, J. R., & Witsil, A. J. (2023). Using Local Infrasound to Estimate Seismic Velocity and Earthquake Magnitudes. *Bulletin of the Seismological Society of America*, 1–23. <https://doi.org/10.1785/0120220237>
- Maekawa, Z. (1968). Noise reduction by screens. *Applied Acoustics*, *1*(3), 157–173. [https://doi.org/10.1016/0003-682X\(68\)90020-0](https://doi.org/10.1016/0003-682X(68)90020-0)
- Maher, S., Matoza, R., de Groot-Hedlin, C., Kim, K., & Gee, K. (2021). Evaluating the applicability of a screen diffraction approximation to local volcano infrasound. *Volcanica*, 67–85. <https://doi.org/10.30909/vol.04.01.6785>
- Marchetti, E., Walter, F., & Meier, L. (2021). Broadband Infrasound Signal of a Collapsing Hanging Glacier. *Geophysical Research Letters*, *48*(16), 1–10. <https://doi.org/10.1029/2021GL093579>
- Marcillo, O., Arrowsmith, S., Whitaker, R., Morton, E., & Scott Phillips, W. (2014). Extracting changes in air temperature using acoustic coda phase delays. *The Journal of the Acoustical Society of America*, *136*(4), EL309–EL314. <https://doi.org/10.1121/1.4896404>

- Matoza, R. S., & Fee, D. (2014). Infrasonic component of volcano-seismic eruption tremor. *Geophysical Research Letters*, *41*(6), 1964–1970. <https://doi.org/10.1002/2014GL059301>
- Matoza, R. S., Garcés, M. A., Chouet, B. A., D’Auria, L., Hedlin, M. A. H., De Groot-Hedlin, C., & Waite, G. P. (2009). The source of infrasound associated with long-period events at Mount St. Helens. *Journal of Geophysical Research*, *114*(B4), B04305. <https://doi.org/10.1029/2008JB006128>
- Meng, H., & Ben-Zion, Y. (2018). Characteristics of Airplanes and Helicopters Recorded by a Dense Seismic Array Near Anza California. *Journal of Geophysical Research: Solid Earth*, *123*(6), 4783–4797. <https://doi.org/10.1029/2017JB015240>
- Mutschlecner, J. P. (2005). Infrasound from earthquakes. *Journal of Geophysical Research*, *110*(D1), D01108. <https://doi.org/10.1029/2004JD005067>
- Novoselov, A., Fuchs, F., & Bokelmann, G. (2020). Acoustic-to-seismic ground coupling: coupling efficiency and inferring near-surface properties. *Geophysical Journal International*, *223*(1), 144–160. <https://doi.org/10.1093/gji/ggaa304>
- Ortiz, H. D., Matoza, R. S., Johnson, J. B., Hernandez, S., Anzieta, J. C., & Ruiz, M. C. (2021). Autocorrelation Infrasound Interferometry. *Journal of Geophysical Research: Solid Earth*, *126*(4), 1–14. <https://doi.org/10.1029/2020JB020513>
- Perttu, A., Taisne, B., De Angelis, S., Assink, J. D., Tailpied, D., & Williams, R. A. (2020). Estimates of plume height from infrasound for regional volcano monitoring. *Journal of Volcanology and Geothermal Research*, *402*, 106997. <https://doi.org/10.1016/j.jvolgeores.2020.106997>
- Pierce, A. D. (2019). *Acoustics*. Cham: Springer International Publishing. <https://doi.org/10.1007/978-3-030-11214-1>
- Poppeliers, C., Anderson Aur, K., & Preston, L. (2019). The Relative Importance of Assumed Infrasound Source Terms and Effects of Atmospheric Models on the Linear Inversion of Infrasound Time Series at the Source Physics Experiment. *Bulletin of the Seismological Society of America*, *109*(1), 463–475. <https://doi.org/10.1785/0120180249>
- Prieto, G. A. (2022). The Multitaper Spectrum Analysis Package in Python. *Seismological Research Letters*, *93*(3), 1922–1929. <https://doi.org/10.1785/0220210332>
- Schmandt, B. (2014). *MSH Node Array*. International Federation of Digital Seismograph Networks. <https://doi.org/10.7914/SN/1D'2014>

- Smets, P. S. M., Evers, L. G., Näsholm, S. P., & Gibbons, S. J. (2015). Probabilistic infrasound propagation using realistic atmospheric perturbations. *Geophysical Research Letters*, *42*(15), 6510–6517. <https://doi.org/10.1002/2015GL064992>
- Sweet, J. R., Anderson, K. R., Bilek, S., Brudzinski, M., Chen, X., DeShon, H., Hayward, C., Karplus, M., Keranen, K., Langston, C., Lin, F., Beatrice Magnani, M., & Woodward, R. L. (2018). A Community Experiment to Record the Full Seismic Wavefield in Oklahoma. *Seismological Research Letters*, *89*(5), 1923–1930. <https://doi.org/10.1785/0220180079>
- Toney, L. (2022). *infresnel*. Zenodo. <https://doi.org/10.5281/zenodo.7388646>
- Uieda, L., Tian, D., Leong, W. J., Jones, M., Schlitzer, W., Grund, M., Toney, L., Yao, J., Magen, Y., Materna, K., Frölich, Y., Belem, A., Newton, T., Anant, A., Ziebarth, M., Quinn, J., & Wessel, P. (2022). *PyGMT: A Python interface for the Generic Mapping Tools*. Zenodo. <https://doi.org/10.5281/zenodo.6702566>
- Ulberg, C. W., Creager, K. C., Moran, S. C., Abers, G. A., Thelen, W. A., Levander, A., Kiser, E., Schmandt, B., Hansen, S. M., & Crosson, R. S. (2020). Local Source Vp and Vs Tomography in the Mount St. Helens Region With the iMUSH Broadband Array. *Geochemistry, Geophysics, Geosystems*, *21*(3), 1–19. <https://doi.org/10.1029/2019GC008888>
- Walker, K. T., Hedlin, M. A. H., de Groot-Hedlin, C., Vergoz, J., Le Pichon, A., & Drob, D. P. (2010). Source location of the 19 February 2008 Oregon bolide using seismic networks and infrasound arrays. *Journal of Geophysical Research*, *115*(B12), B12329. <https://doi.org/10.1029/2010JB007863>
- Wang, R., Schmandt, B., & Kiser, E. (2020). Seismic Discrimination of Controlled Explosions and Earthquakes Near Mount St. Helens Using P / S Ratios. *Journal of Geophysical Research: Solid Earth*, *125*(10), 1–15. <https://doi.org/10.1029/2020JB020338>
- Wang, S. (1996). Finite-difference time-domain approach to underwater acoustic scattering problems. *The Journal of the Acoustical Society of America*, *99*(4), 1924–1931. <https://doi.org/10.1121/1.415375>
- Watson, L. M., Iezzi, A. M., Toney, L., Maher, S. P., Fee, D., McKee, K., Ortiz, H. D., Matoza, R. S., Gestrich, J. E., Bishop, J. W., Witsil, A. J. C., Anderson, J. F., & Johnson, J. B. (2022). Volcano infrasound: progress and future directions. *Bulletin of Volcanology*, *84*, Article 44. <https://doi.org/10.1007/s00445-022-01544-w>
- Wessel, P., Luis, J. F., Uieda, L., Scharroo, R., Wobbe, F., Smith, W. H. F., & Tian, D. (2019). The Generic Mapping Tools Version 6. *Geochemistry, Geophysics, Geosystems*, *20*(11), 5556–5564. <https://doi.org/10.1029/2019GC008515>

- Wills, G., Nippress, A., Green, D. N., & Spence, P. J. (2022). Site-specific variations in air-to-ground coupled seismic arrivals from the 2012 October 16 explosion at Camp Minden, Louisiana, United States. *Geophysical Journal International*, *231*(1), 243–255. <https://doi.org/10.1093/gji/ggac184>
- Witsil, A., Fee, D., Dickey, J., Pena, R., Waxler, R., & Blom, P. (2022). Detecting Large Explosions with Machine Learning Models Trained on Synthetic Infrasound Data. *Geophysical Research Letters*, 1–15. <https://doi.org/10.1029/2022GL097785>

4.10 Supplemental Material

This supplemental material contains a plot of regional infrasound recordings of iMUSH explosions (Figure 4.10) and plots of the atmospheric profiles used as inputs for our numerical infrasound propagation modeling (Figure 4.11).

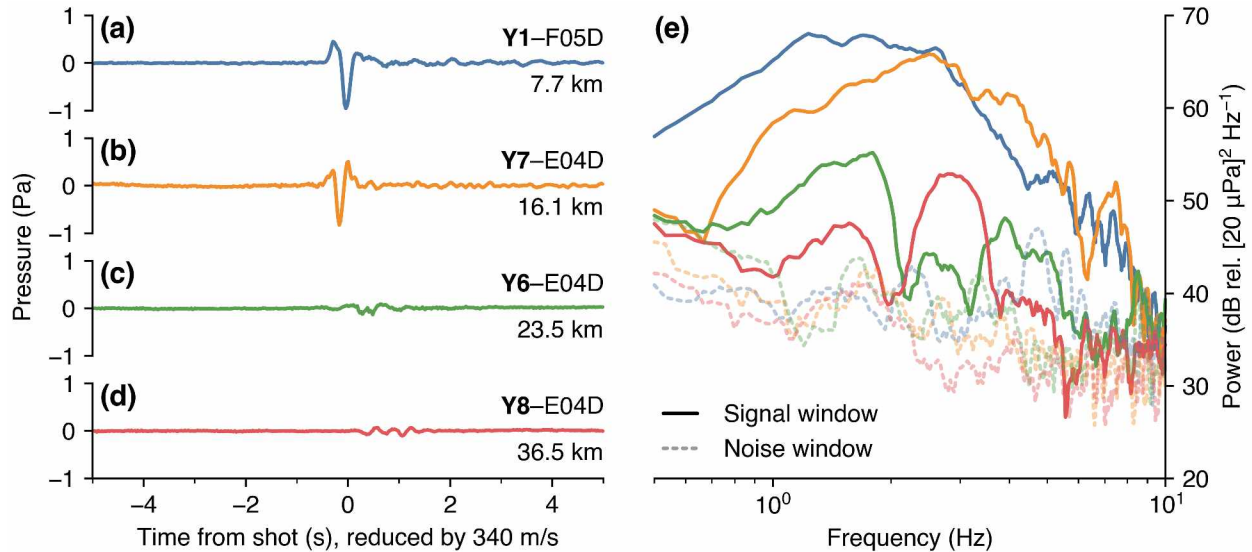


Figure 4.10 EarthScope Transportable Array (TA) infrasound station recordings of iMUSH shots. Panels (a)–(d) show pressure waveforms from various shots recorded on two TA stations, F05D and E04D (station locations are shown in Figure 4.1a inset). The shot name is in boldface, and the recording station is noted. Shot–station distances appear under each waveform. Waveforms are not filtered. Note that the x -axis is reduced time. Panel (e) shows signal and noise spectra for the shot–station pairs in panels (a)–(d). Signal spectra come from a 30 s window centered on the arrival onset assuming a celerity of 340 m/s; noise spectra are taken from a 30 s window immediately preceding the signal window.

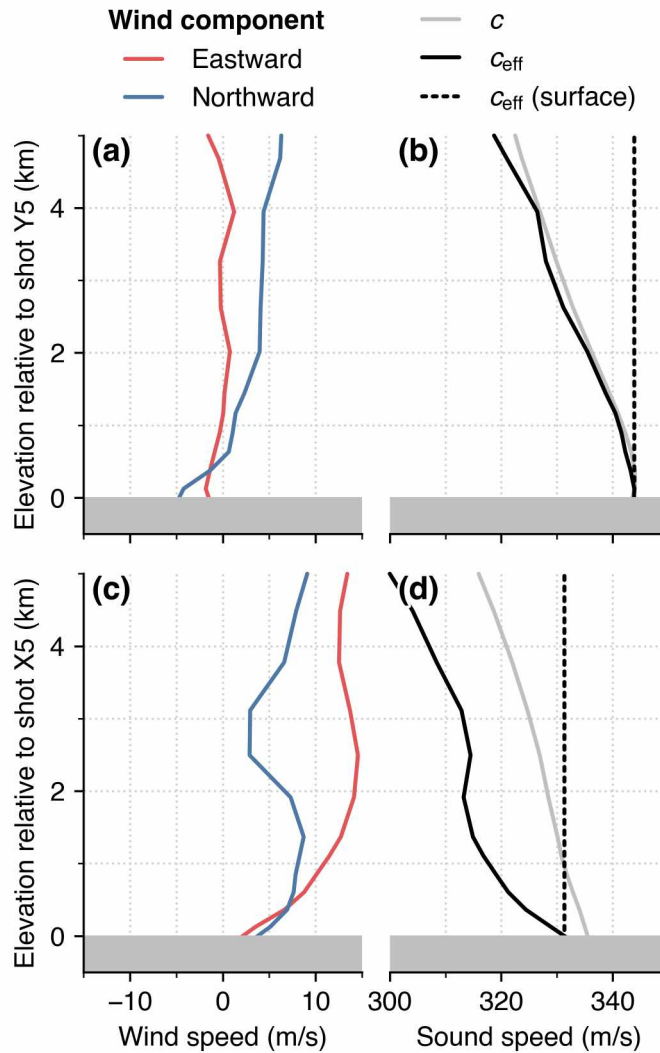


Figure 4.11 ERA5 atmospheric profiles used in our numerical modeling. Panel (a) shows the horizontal wind components from the profile used for the shot Y5 transect and panel (b) shows the static sound speed, c , calculated from the profile temperature using Equation 4.3, as a gray line. The effective sound speed in the direction of propagation, $c_{\text{eff}} = c + w_p$ (see Equation 4.2), is plotted as a black line. Refraction occurs where c_{eff} exceeds its surface value (plotted as a vertical dashed line). Panels (c) and (d) are identical to panels (a) and (b), but for the shot X5 transect. Note that the y -axis limits are identical to those in Figures 4.7a and 4.8a to facilitate comparison.

Chapter 5: General Conclusions

The title of this dissertation — “Characterization of geohazards via seismic and acoustic waves” — is broad. However, it is necessarily so: the methods applied in this dissertation span seismic source modeling, geophysical inversion, acoustic propagation modeling, machine learning, and signal processing. The processes studied include surficial mass movements, volcanic explosions, and buried chemical explosions. We apply these methods on volcanoes in Alaska and Washington state in the U.S., and in Vanuatu in the South Pacific Ocean. Here, I draw connections between the three chapters forming the body of this dissertation, and discuss avenues for further investigation.

In Chapter 2, we take advantage of an extraordinary repeating seismoacoustic source in the form of two massive avalanches at Iliamna Volcano (Alaska). Unraveling the dynamics of these energetic events is challenging, since the source area is distributed and in motion. The infrasound produced by these avalanches is recorded at distances where neither topographic nor atmospheric effects can be ignored — as demonstrated in Chapter 4. However, the similarity of the two avalanches enables us to compare observations between the two events, allowing us to separate source from propagation effects. Since this work was conducted, the Alaska Volcano Observatory has installed an additional infrasound array (**AV.KENI**) on the Kenai Peninsula. Infrasound from future avalanches at Iliamna will therefore be better captured. Additional geophysical station coverage around Iliamna is beneficial not just for studies of avalanche activity on the volcano, but also for machine learning techniques which rely on labeled data examples. Unlike in Chapter 3, where we use an automated approach to label explosions, machine learning for mass movement characterization will likely rely on waveforms extracted for specific, documented events. Iliamna has been, and will continue to be, an excellent “natural laboratory” for measuring and interpreting seismoacoustic signals from large mass movements.

Chapter 3 is a proof-of-concept for local volcano infrasound machine learning classification, using the highly-active Yasur Volcano (Vanuatu) as a test case. We find that the effects of propagation over topography leave a very clear fingerprint on the recorded infrasound waveforms; this fingerprint is used by the classifier to make decisions about the subcrater of origin. This is evidenced by the much higher single-station classification performance ($\sim 95\%$) versus network-generalized performance ($\sim 75\%$). A key outcome of this study is the creation of a large, labeled catalog of infrasound waveforms. As discussed in §1.3, such catalogs have largely been limited to seismic sources and waveforms (e.g., Mousavi et al., 2019). Our labeled infrasound waveform catalog can be used by community members as a benchmark dataset (see, e.g., Woollam et al., 2022) to evaluate different ML algorithms. For example, deep learning techniques could be applied to the dataset. Presumably, these methods would yield even better classification performance.

In Chapter 4, we demonstrate the utility of a large-N nodal seismic array for recording infrasound, using an active-source experiment at Mount Saint Helens (Washington state) as a testbed. The prospect of leveraging acoustic–seismic coupling on seismometers is very appealing, since there are many more seismometers than infrasound sensors currently deployed worldwide (Wills et al., 2022). However, a major challenge exists in accounting for the highly spatially variable acoustic–seismic transfer function. Our observations indicate that this transfer function can vary significantly at hundred-meter scales, presumably due to large heterogeneities in near-surface geologic materials and structure. In spite of this challenge, our results show that high spatial density recordings of the infrasound wavefield can reveal fine-scale propagation effects not captured with the sparse spacing of typical infrasound networks. As instrumentation technologies continue to evolve, large-N infrasound deployments may soon be realized. The methods and modeling we apply in this chapter can be transported to such deployments. Our work also highlights the utility of high-resolution (mesoscale) weather models. These data are not generally used by the infrasound community beyond incorporation into the lower atmosphere elevations of 1D atmospheric profiles

(Schwaiger et al., 2019). Furthermore, they are not archived or documented in a systematic manner. Future work should evaluate these higher-resolution weather models against other, coarser reanalysis products and explore ways to integrate these models into propagation modeling codes. It is possible that cases where propagation modeling does not capture observed infrasound arrivals, such as the modeling we perform in Chapter 2, may be “solved” through the use of higher-resolution weather models.

5.1 Additional Work

The completion of this dissertation does not conclude all of the work performed during my time at UAF. Some ongoing and future work, beyond what is addressed in the body of this dissertation, is mentioned here. This work fits in to the general theme of this dissertation, as it involves seismoacoustics for hazard characterization.

5.1.1 *Summer 2023 return to Yasur Volcano*

In July and August of 2023, I will travel to Yasur Volcano, Vanuatu to take part in a multi-institutional and multi-disciplinary study of the volcano. This work follows up on the 2016 deployment which provided the data for Chapter 3 of this dissertation. Planned equipment for deployment includes three-component broadband seismometers, infrasound sensors, volcanic gas instruments, UAS (drones) with various payloads, and a cable and interrogator for distributed acoustic sensing.

Objectives of the work include obtaining better imagery and video to compare with multi-parametric time series of explosive activity, more complete recordings of Yasur’s very-long-period seismicity (Matoza, Chouet, et al., 2022), and better capture of explosion source directionality with additional aerial (UAS-hosted) infrasound sensors (Iezzi et al., 2019).

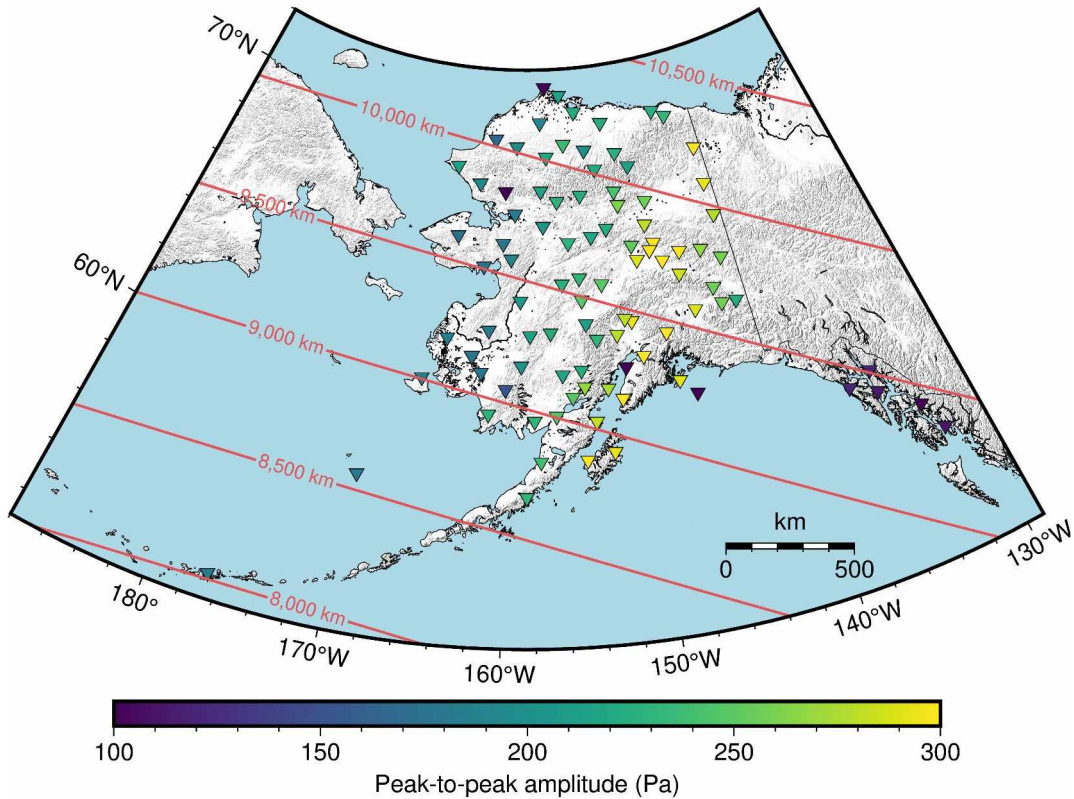


Figure 5.1 Peak-to-peak amplitude measurements of the Lamb wave from the Hunga volcano eruption for stations located in Alaska. Warmer colors indicate larger amplitudes. Red lines delineate distances from the volcano. Based on Figure S12 in Matoza, Fee, et al. (2022).

5.1.2 Atmospheric acoustic waves in Alaska from the Hunga volcano eruption

The 15 January 2022 eruption of Hunga volcano (Tonga) produced a truly unprecedented set of global atmospheric acoustic observations (Matoza, Fee, et al., 2022). The most prominent global arrival is an acoustic-gravity wave called a Lamb wave, which circled the Earth multiple times (Matoza, Fee, et al., 2022). This wave is well-recorded by Alaska’s dense regional network of microbarometers (sensitive air pressure sensors). Figure 5.1 shows peak-to-peak amplitude measurements of the first pass of the Lamb wave through Alaska. There are amplitude variations of up to ~ 200 Pa across the network. A notable east–west spatial trend exists in the amplitudes. These observations can be probed further, and causes for this observed pattern can be considered.

5.2 References

- Iezzi, A. M., Fee, D., Kim, K., Jolly, A. D., & Matoza, R. S. (2019). Three-dimensional acoustic multipole waveform inversion at Yasur Volcano, Vanuatu. *Journal of Geophysical Research: Solid Earth*, *124*(8), 8679–8703. <https://doi.org/10.1029/2018JB017073>
- Matoza, R. S., Chouet, B. A., Jolly, A. D., Dawson, P. B., Fitzgerald, R. H., Kennedy, B. M., Fee, D., Iezzi, A. M., Kilgour, G. N., Garaebiti, E., & Cevuard, S. (2022). High-rate very-long-period seismicity at Yasur volcano, Vanuatu: Source mechanism and decoupling from surficial explosions and infrasound. *Geophysical Journal International*, *187*(4)(June), 717–725. <https://doi.org/10.1093/gji/ggab533>
- Matoza, R. S., Fee, D., Assink, J. D., Iezzi, A. M., Green, D. N., Kim, K., Toney, L., Lecocq, T., Krishnamoorthy, S., Lalande, J.-m., Nishida, K., Gee, K. L., Haney, M. M., Ortiz, H. D., Brissaud, Q., Martire, L., Rolland, L., Vergados, P., Nippres, A., ... Wilson, D. C. (2022). Atmospheric waves and global seismoacoustic observations of the January 2022 Hunga eruption, Tonga. *Science*, *377*(6601), 95–100. <https://doi.org/10.1126/science.abo7063>
- Mousavi, S. M., Sheng, Y., Zhu, W., & Beroza, G. C. (2019). STanford EArthquake Dataset (STEAD): A Global Data Set of Seismic Signals for AI. *IEEE Access*, *7*, 179464–179476. <https://doi.org/10.1109/ACCESS.2019.2947848>
- Schwaiger, H. F., Iezzi, A. M., & Fee, D. (2019). AVO-G2S: A modified, open-source Ground-to-Space atmospheric specification for infrasound modeling. *Computers & Geosciences*, *125*(February 2018), 90–97. <https://doi.org/10.1016/j.cageo.2018.12.013>
- Wills, G., Nippres, A., Green, D. N., & Spence, P. J. (2022). Site-specific variations in air-to-ground coupled seismic arrivals from the 2012 October 16 explosion at Camp Minden, Louisiana, United States. *Geophysical Journal International*, *231*(1), 243–255. <https://doi.org/10.1093/gji/ggac184>
- Woollam, J., Münchmeyer, J., Tilmann, F., Rietbrock, A., Lange, D., Bornstein, T., Diehl, T., Giunchi, C., Haslinger, F., Jozinović, D., Michelini, A., Saul, J., & Soto, H. (2022). SeisBench—A Toolbox for Machine Learning in Seismology. *Seismological Research Letters*, *93*(3), 1695–1709. <https://doi.org/10.1785/0220210324>